FORSCHUNGSZENTRUM JÜLICH GmbH

Institut für Grenzflächenforschung und Vakuumphysik

Surface Morphology of Clean and Adsorbate Covered Au(111) Investigated by Scanning Tunneling Microscopy under Ambient Conditions

Lin Huang

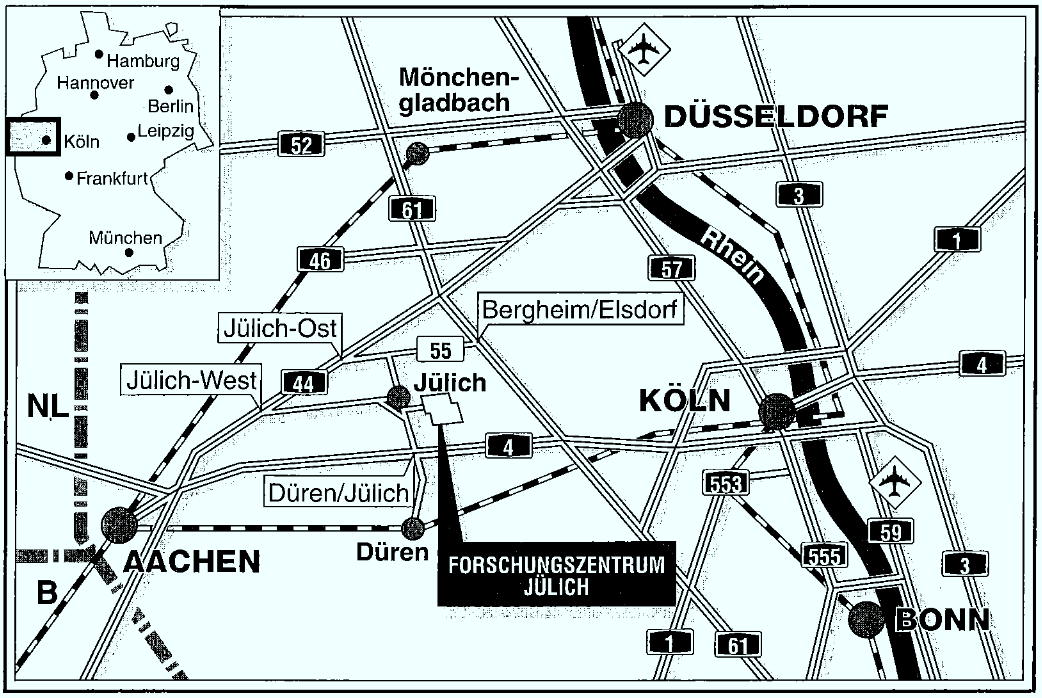

Berichte des Forschungszentrums Jülich ; 3251
ISSN 0944-2952
Institut für Grenzflächenforschung und Vakuumphysik Jül-3251
D 5 (Diss. Universität Bonn)

Zu beziehen durch: Forschungszentrum Jülich GmbH · Zentralbibliothek
D-52425 Jülich · Bundesrepublik Deutschland
Telefon: 02461/61-6102 · Telefax: 02461/61-6103 · Telex: 833556-70 kfa d

Surface Morphology of Clean and Adsorbate Covered Au(111) Investigated by Scanning Tunneling Microscopy under Ambient Conditions

Lin Huang

Abstract

The surface morphology of clean and adsorbate covered Au(111) has been systematically studied using scanning tunneling microscopy (STM) under ambient conditions. The results demonstrate that using STM and X-ray diffraction (XRD) some particular surface science topics can be investigated also in the ambient environment. The investigations of surface properties under ambient conditions will advance our understanding of many important processes involved in the manufacturing environment.

Firstly, the clean Au(111) surface has been studied. Because of its inertness, the Au(111) surface is a well suited substrate for adsorption studies in ambient environment. Furthermore, the clean Au(111) surface undergoes a $(22 \times \sqrt{3})$ reconstruction which can be used as an ideal model system to evaluate the performance of our STM operated in air. In most cases, the appearance on both large and atomic scales and behavior of the reconstruction of Au(111) in air show similarities with those in ultra-high vacuum (UHV). Due to the presence of adsorbates, mobility of the reconstruction patterns in air is higher, particularly at structural imperfections. In rare cases, the decay of the reconstruction and a phase transition between the $(22 \times \sqrt{3})$ and (1×1) structure are also observed on the freshly prepared samples.

Secondly, iodine adlayer structures on Au(111) have been studied. Since the adlayer forms different phases as a function of coverage, I/Au(111) serves as a model system to study two dimensional (2D) phenomena such as commensurate-incommensurate (C-I) phase transitions of the surface structures. Three distinct adlayer structures have been obtained using ex-situ coverage control: (i) at low iodine coverage, a commensurate $(\sqrt{3} \times \sqrt{3})$R30° structure is formed. (ii) in the coverage range from 0.33 to 0.4, a uniaxially compressed $(p \times \sqrt{3})$ structure is observed. (iii) at the iodine monolayer saturation coverage, a hexagonally compressed moiré-type incommensurate structure is found. From the observation of parallel domain walls it follows that the phase transition from (i) to (ii) is of *second* order. The coexistence of phases (ii) and (iii) on the same surface area indicates that the corresponding phase transition in this case is of *first* order. By changing the tunneling parameters either iodine adlayer or the gold substrate can be "selectively" imaged. In this way the properties of the adlayer structures could be determined with high precision. This unique feature of STM may find wider applications in the study of other adsorption systems.

Thirdly, the surface morphology of Au(111) after annealing in high pressure oxygen at high temperatures have been investigated. Two types of oxygen-induced structures on the Au(111) surface have been observed: (i) a hexagonal long-range reconstruction with a periodicity of 60-80 Å and a corrugation of ~ 0.5 Å. At the atomic scale this surface exhibits a $(\sqrt{3} \times \sqrt{3})$R30° structure, which we attribute to atomic oxygen strongly chemisorbed at the Au(111) surface. The superstructure can be satisfactorily described as the result of a moiré pattern induced by an in plane lattice mismatch and a slight rotation between the topmost gold layer and its underlying substrate due to the presence of the adsorbate. (ii) a "modified" herringbone structure related to the original herringbone reconstruction of the clean Au(111) surface, but with additional

depressions in some of the fcc-regions between the reconstruction double-lines. At the atomic scale the surface exhibits a characteristic 'row structure' with $\sqrt{3}$ periodicity. The observation of localized areas of the $(\sqrt{3} \times \sqrt{3})$R30° phase with the characteristic long-range hexagonal superstructure indicates that the formation of this reconstruction upon exposure to oxygen proceeds via nucleation and growth. Therefore, surface defects or impurities should play a crucial role in the nucleation process. Preliminary studies on the chemical composition of the surface using X-ray photoelectron spectroscopy (XPS) and Auger electron spectroscopy (AES) reveal the presence of oxygen on the surface, and that the concentration of the most common impurities such as Ca and Si is below the detection limit of XPS and AES. This indicates that the observed structures are intrinsically induced by the chemisorption of oxygen on Au(111). The oxygen-induced hexagonal reconstruction is found to be very stable in air and has been studied using synchrotron X-ray diffraction. In a first XRD experiment all the diffraction peaks expected for the $(\sqrt{3} \times \sqrt{3})$R30° structure and the long-range hexagonal superstructure were observed in reciprocal space. The position of superstructure peaks together with the shift of the $\sqrt{3}$ peak from the expected normal position indicates an expansion of the topmost gold layer while oxygen atoms are most likely commensurate with this layer.

Finally, the influence of an externally applied strain on the $(22 \times \sqrt{3})$ reconstruction of Au(111) has been investigated. An experimental set-up has been developed which allows STM investigations on surface structures of a bent Au(111) single crystal (0.3 mm thick). Using STM, it has been verified that the bending experiments are within the elastic regime. The observations show that the external strain can produce a change of the reconstruction patterns as well as a structure transformation from the $(22 \times \sqrt{3})$ reconstructed phase to the (1×1) surface. The details of the deconstruction depend not only on the amplitude of the applied strain, but also on the orientation between the strain vector and the local reconstruction domains. The results can be qualitatively understood from simple theoretical models.

Contents

List of Figures

Chapter 1

Introduction

The last thirty years have witnessed the development of surface science at the speed of an explosion. Since the progress of ultrahigh vacuum (UHV) techniques provides a well-controlled, *scientific environment* , various kinds of surface analytical methods have been developed and applied to study the phenomena occurring at the gas-solid interface. The complete understanding of these phenomena is of great importance for both science and technology. The use of UHV techniques and single crystal samples have allowed experimentalists to obtain clean and well-characterized surfaces and to avoid the problems faced in more realistic environment. This procedure also reduces the complexity of the theories invoked to explain the experimental observations. Hence, the majority of the surface science experiments are performed under UHV conditions.

In some cases, however, particularly when dealing with industrial problems, the results obtained from experiments performed under UHV conditions do not necessarily provide the correct descriptions of the real processes due to the "pressure gap" [1]. Indeed, 'real' surfaces involved in the industrial processes are mostly subjected to a very different environment, namely, the *manufacturing environment* . There are two possibilities to overcome this difficulty: (i) to simulate the industrial environment in a UHV apparatus by introducing various kinds of gases or to extrapolate the results obtained in UHV across a large pressure range [2]; (ii) to study the surface properties directly in the manufacturing environment, that is, to perform experiments under ambient conditions. Although the second approach has been recognized and pursued for a long time, the lack of suitable analytical tools has prevented its realization until recently. Most of the surface science techniques have been developed for the use in UHV, which usually involve the interactions of particles with surface. Since this interaction will be modified in an environment other than vacuum, in most cases these methods cannot be used to study the surface properties under ambient conditions. With the invention of the scanning tunneling microscopy (STM) [3] and a series of related scanning probe microscopies (SPM), however, versatile and affordable tools have emerged that could give the structure information of the gas-solid or liquid-solid interfaces under ambient conditions down to the atomic scale. STM experiments in air are particularly useful for technological applications such as: (i) the study of surface diffusion which is important to many surface processes, such as surface reactions, adsorption and thin film growth; (ii) the determination of surface roughness on a nanometer scale; (iii) the measurement of microscopic surface mechanical properties like friction constants or hardness; (iv) the modification of surface structures at the nanometer scale in ambient environment. Finally, the possibility of performing STM experiments in liquids has opened the door for *in-situ* electrochemical studies and the numerous applications of STM/AFM in biological investigations.

In the past 15 years since its invention, STM applications in surface science has made great progress in the UHV environment. Recently, the achievements in electrochemistry and biology are also remarkable. At the same time, many investigations have been performed in air [4, 5, 6, 7]. For instance, the first atomic resolution images on a densely parked metal surface were obtained on a Au(111) by STM in air [6]. While the STM has become a standard and versatile analytical tool in UHV surface science studies, many difficulties for STM operated in air still remain unresolved, such as: (i) building a reliable air-STM system that routinely provides high quality and reproducible results [7, 8, 9]; (ii) calibrating an STM in air using model systems which have been well characterized by other methods in well-controlled environments; (iii) systematically studying surface science issues in realistic environments; (iv) developing suitable models to give a correct interpretation of the data. The overcomimg of these difficulties is critical for the STM in order to become a standard and mature technique for the study of surface processes occurring in the ambient environment.

The aim of this thesis is to use STM to study properties of well-defined surfaces under ambient conditions. The following tasks have been the main concerns in this work:
(i) design and construction of a reliably working microscope;
(ii) developing suitable methods to prepare tunneling tips and samples;
(iii) finding model system for the STM calibration;
(iv) taking advantages of the air STM to study the surface science issues which are not suitable or maybe difficult to be investigated in UHV.
In the present work, we have studied iodine adlayer structures on Au(111); oxygen interactions with Au(111) under high temperature and pressure conditions; reconstruction of Au(111) under external strain.

This thesis is organized as follows: the STM instrumentation and preparation of tip and sample are described in detail in chapter 2. In chapter 3 the results on the reconstruction of Au(111) imaged under ambient conditions are presented. Iodine adlayer structures on Au(111) are described in chapter 4. The oxygen induced restructuring of the Au(111) surface is described in chapter 5. In chapter 6 we present results on the influence of an externally applied strain on the Au(111) reconstruction. The main results presented in this thesis are summarized in chapter 7.

Chapter 2

Experimental

2.1 Scanning tunneling microscopy

If a sharp metal tip is brought near to a planar sample surface, so close that the wave function of the tip and the sample can overlap, then the electrons will be able to tunnel through the barrier separating tip and sample when a small bias is applied between them. The resulting current is a function of the bias voltage, tip-sample separation, and the barrier height between them. According to the first-order perturbation theory, at low temperatures the tunneling current can be written as [10]:

$$I = \frac{2\pi e}{\hbar} \sum_{\mu\nu} f(E_\mu)[1 - f(E_\nu) + eV)] \, |M_{\mu\nu}|^2 \, \delta(E_\mu - E_\nu), \tag{2.1}$$

where $M_{\mu\nu}$ is the tunneling matrix element, *f(E)* is the Fermi function, V is the bias voltage between sample and tip, and E_μ is the energy of the state μ, where μ and ν run over all the states of tip and sample, respectively. In case the tip structure is modeled as a spherical potential well of radius R at a position denoted by $\vec{r}_t$, the tunneling current in the limit of small voltage is

$$I \propto V e^{2\kappa R} \rho(\vec{r}_t, E_f), \tag{2.2}$$

where $\kappa = \sqrt{2m\Phi}/\hbar$, Φ is the barrier height and $\rho(\vec{r}_t, E)$ is the surface local density of states (LDOS) at point $\vec{r}_t$ and energy E. With d as the distance between tip and sample, and

$$\rho(\vec{r}_t, E) = \sum_{\nu} |\Psi_\nu(\vec{r}_t)|^2 \, \delta(E_\nu - E), \tag{2.3}$$

$$|\Psi_\nu(\vec{r}_t)|^2 \propto \exp(-2\kappa(R + d)), \tag{2.4}$$

we obtain the result that

$$I \propto e^{(-2\kappa d)}. \tag{2.5}$$

The most important feature of this tunneling process is that the current is exponentially dependent on the tip-sample separation. Since $\kappa = 0.51\sqrt{\Phi(eV)}$ Å^{-1}, with a typical value of work function for a metal $\Phi \approx 4$ eV, a 1 Å decrease in the tip-sample separation will increase the current by almost one order of magnitude. This high sensitivity can be used to measure the change in tip-sample separation with very high vertical resolution. Usually, STM is operated in the so called constant current mode, in which a feedback mechanism is used to maintain a constant current as the tip is scanned over the sample. If the bias applied is kept constant, maintaining a constant current requires the vertical position of tip to be altered such as to follow the contour of constant Fermi-level LDOS of the surface. In most cases, the images bear a strong similarity to the constant charge density contour of the surface.

A unique advantage of STM is that it can be operated under ambient conditions, since the tunneling process itself will usually not be disturbed in the presence of the atmospheric gas. The reason is that the volume involved in the tunneling process is extremely small ($\leq 10^3$ Å^3). In such a small working volume of the STM, the effective number of molecules is only 10^{-2} even at atmospheric pressure. If the sample is inert enough, it is possible that the 'clean' surface properties can be investigated by STM in air.

2.2 Instrumentation

The STM measurements presented in this work were performed using a home-made modified "beetle" type instrument [11]. The advantages of this type of STM are: (i) it is a fast and easy to operate system. (ii) the rigid and compact design provides high stability against vibration. (iii) the microscope is constructed of identical piezoelectric elements, therefore, the STM itself is completely temperature compensated. The thermal drift is one of the most critical factors for successful tunneling microscopy, particularly when the microscope is operated in air. By using this kind of design the influence of thermal drift can be reduced efficiently.

The microscope was operated at room temperature either in rough-vacuum ($p \sim 1 \cdot 10^{-2}$ mbar) or in a neutral gas atmosphere. The construction details are illustrated in Fig. 2.1. A glass bell-jar (Leybold), which serves as the vacuum chamber for the STM, is placed on the open flange of a metal pot. There are several openings with flanges distributed around the side wall of the pot. Through these flanges the vacuum system and electronic signals are connected to the chamber and the microscope, respectively. The microscope is mounted on a lever-micrometer, by which the STM head can be positioned on top of or removed from the sample. The sample is fixed on the sample holder by a special "walk-ring" which is constructed as a triple helix with a slope of 0.3 mm used for the tip-sample coarse approach. This approach is made by the rotation of the STM scan head around the center of the "walk-ring", which causes the tip to move closer or farther from the sample surface. The sample holder is composed of one stainless steel part and two thick copper disks separated by viton rings. Another special kind of sample holder used to study the influence of an external strain on the surface structures will be described in detail in chapter 6. The whole system is placed on an anti-vibration air damped table. Since the operating principle of this type of STM has been described in detail elsewhere [11, 12], it will not be explained here.

Usually, the chamber is first evacuated and then either filled with neutral gas (Ar, N_2) or kept under vacuum. With this design the influence of temperature drift and acoustic vibration can be effectively reduced. Furthermore, the sample surface can be

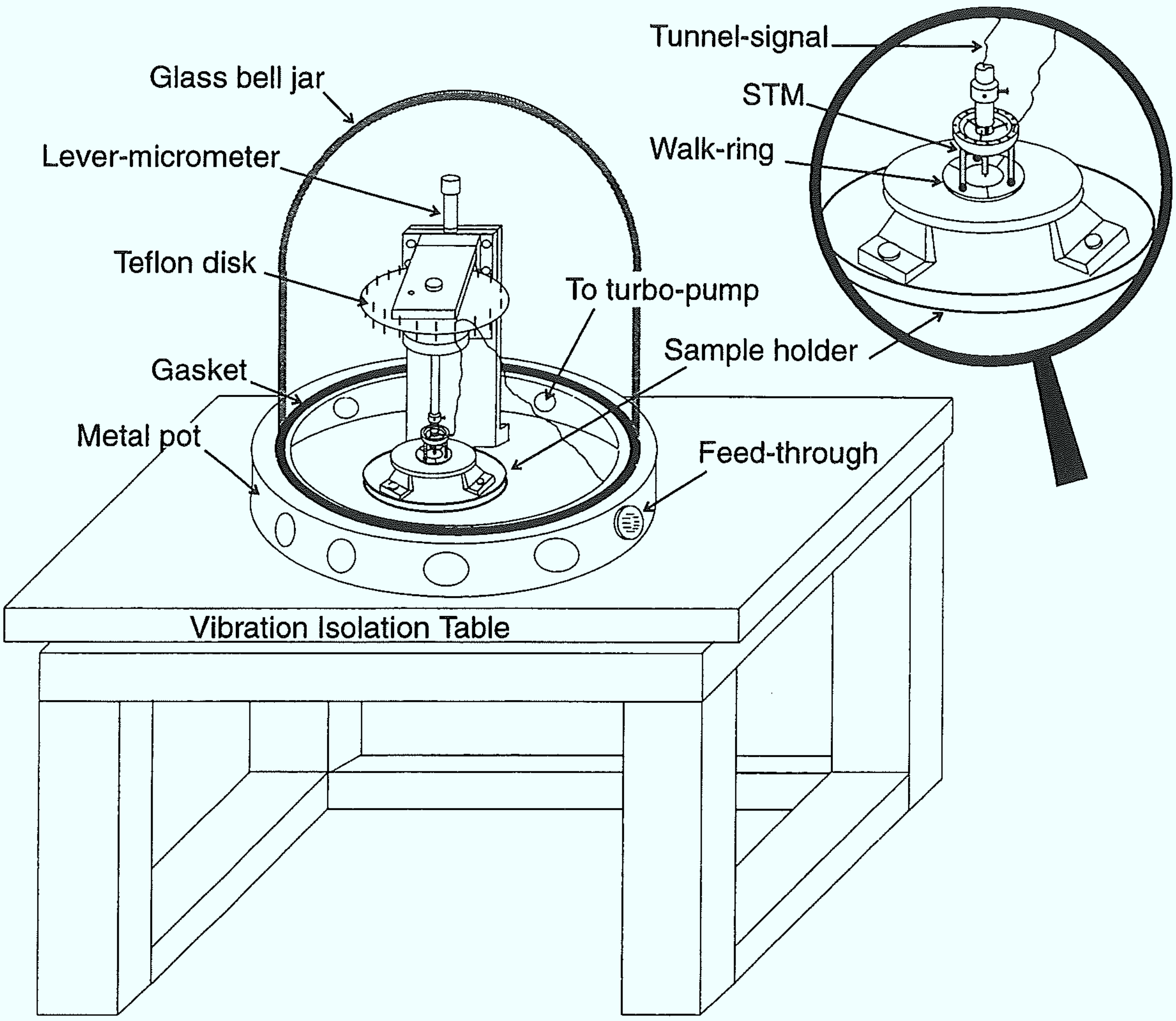

Figure 2.1: Schmatic illustration of the STM apparatus

kept free from water or other contamination in air for a longer period of time. On the other hand, it is still very convenient to change tip and sample. The pumping system is usually disconnected from the chamber during image acquisition in order to avoid vibration. Note, however, that during the sample preparation and transfer to the STM as well as changing of the tip, it is impossible to avoid the exposure of the sample surface to the air in the laboratory.

All STM images were obtained using constant current mode. The electronics used is an STM-Control 03, which has been developed in this institute by M. Teske. The details of the electronics have been described elsewhere [13]. One important feature of this electronics is the use of an adjustable electronic high-pass filter for recording the images. This acquisition mode allows to suppress the average inclination of the sample and, thus, to take advantage of the full gray scale to display the surface morphology. Another effect caused by this high-pass filter is the impression that the surface is illuminated from the left. However, the *quantitative* information on the tip height (e.g. to determine the surface corrugation) has been extracted from images recorded without the high-pass filter. The software used for image acquisition and processing was developed in this institute by W. Hürttlen. In some particular cases, the contrast of the images were artificially enhanced after data acquisition. Unless indicated, other 'filters' were not used in the image processing.

One of the major problems in STM is the role played by the unknown structure of the tunneling tip during the measurements. There are several ways to prepare tunneling tips [14], the most popular methods are mechanical forming or electrochemical etching. Electrochemical etching has become the standard technique to prepare W tips for UHV-STM. Since the W tips are very easily oxidized in air, they cannot provide stable and high quality images when used with STM in air. In this work mechanically polished 0.25 mm diameter iridium tips were used. Since iridium is very hard, the mechanical grinding method can be easily adopted. Also, iridium is rather stable against oxidation. The very high cohesive energy of 6.93 eV makes the breaking of bonds at the Ir surface quite difficult and, thus, prevents the formation of compounds.

The electronic properties of tip materials were investigated theoretically in Ref. [15]. The results are listed in Table 2.1. It can be seen that W, Pt, Ir are all good candidates for use as tunneling tips mainly because the simple s and d states are the dominant electronic states at the Fermi level. The influence of the tip electronic states on the STM imaging has been the subject of many studies. According to the reciprocity principle [16], the presence of a d-type state on the tip may explain the origin of an enhanced atomic resolution on metal surfaces. Experimentally, the high quality atomic-resolution images obtained in this work demonstrate that Ir is indeed a good choice for use as tunneling tip in air, and that the preparation method used here is successful.

Material	W	Pt	Ir
s state	3.1%	0.77%	0.94%
d state	85%	98%	96%

Table 2.1: Electronic density of states at the Fermi level for common tip materials.

2.3 Samples and preparation

Two types of Au(111) samples were used in this work, the preparation prcedure is described in detail in the following.

2.3.1 Au(111) single crystals

The Au(111) single crystals are 2 mm thick disks, with a diameter of 8 mm. They were mechanically polished and aligned to have a (111) surface orientation. The bulk mosaicity of the sample is less than 0.2°. Usually, further preparation is necessary after polishing to improve the sample properties. In a recent review article, two possible procedures to prepare Au single crystals used as electrodes in an electrolyte cell are suggested: sputtering and annealing in UHV or flame annealing [17]. While the flame

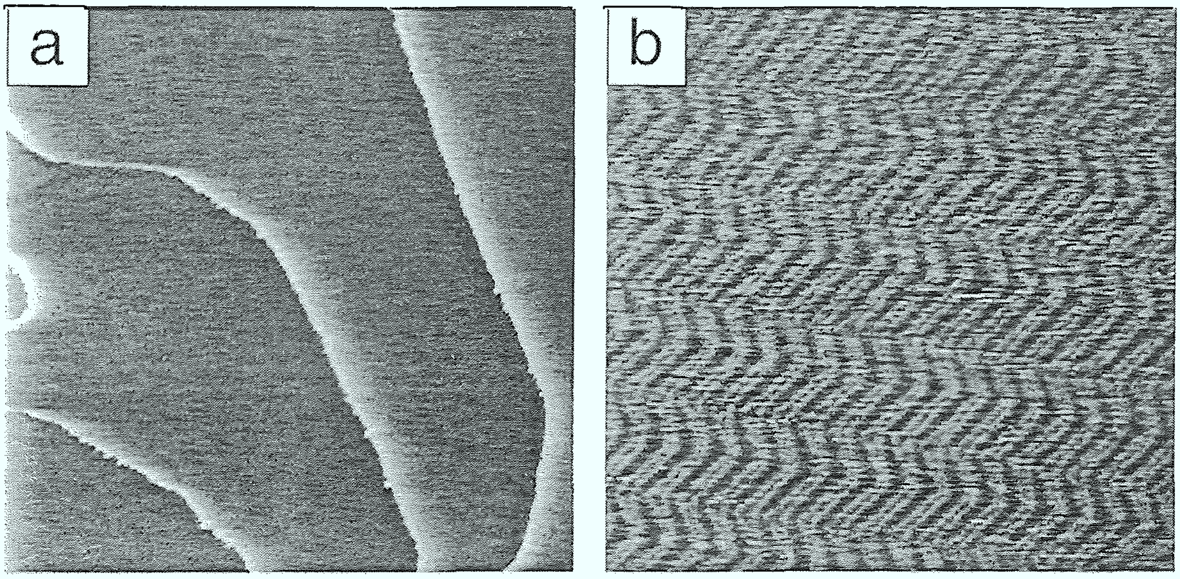

Figure 2.2: (a) STM topograph of the Au(111) single crystal surface after annealing in argon at 800°C for 1 h (6000 × 6000 Å). Tunneling parameters: V_t=170 mV, I_t=2 nA. (b) Higher magnification image revealing the "herringbone" reconstruction (1450×1450 Å). Tunneling parameters: V_t=40 mV, I_t=10 nA.

annealing method was often used to prepare the gold thin film samples in this work, another more gentle way to prepare the gold single crystals was developed. We have annealed the crystals in a furnace with well-controlled temperature and gas-atmosphere. The advantages of this method are obvious: it does not need UHV facilities and there is no risk to damage the crystals as with flame annealing. The recipe of the preparation consists of alternatingly annealing the samples under oxygen and argon atmosphere in a temperature range of 700 – 1000°C for a time interval between 10 minutes to 24 hours depending on the sample history. On the so prepared sample surface, large terraces exhibiting the $(22 \times \sqrt{3})$ herringbone reconstruction (see chapter 3) were observed by STM. The STM images shown in Fig. 2.2 reveal the typical morphology of the Au(111) single crystal surface after annealing in the furnace. As seen in Fig. 2.2a, large terraces separated by monatomic steps have an average width of a few hundred nanometers. The herringbone reconstruction on these large terraces revealed by the image in Fig. 2.2b clearly resembles the morphology of the clean Au(111) surface observed in UHV after standard preparation. This sample has already been subjected to several cycles of annealing in oxygen and argon. The STM characterization of the annealed crystals proves that the preparation method used is successful.

2.3.2 Au(111) thin films on quartz

Although the gold *single crystals* are the 'better' substrates for STM studies, the high cost is the main problem that prevents them being widely used. The search for lower-cost, easy to handle substitutes has been the subject of many investigations. The interest has mainly focused on gold thin films deposited on various kinds of substrates, such as mica [18, 19, 20], quartz glass [21], and silicon surfaces [22]. The properties of

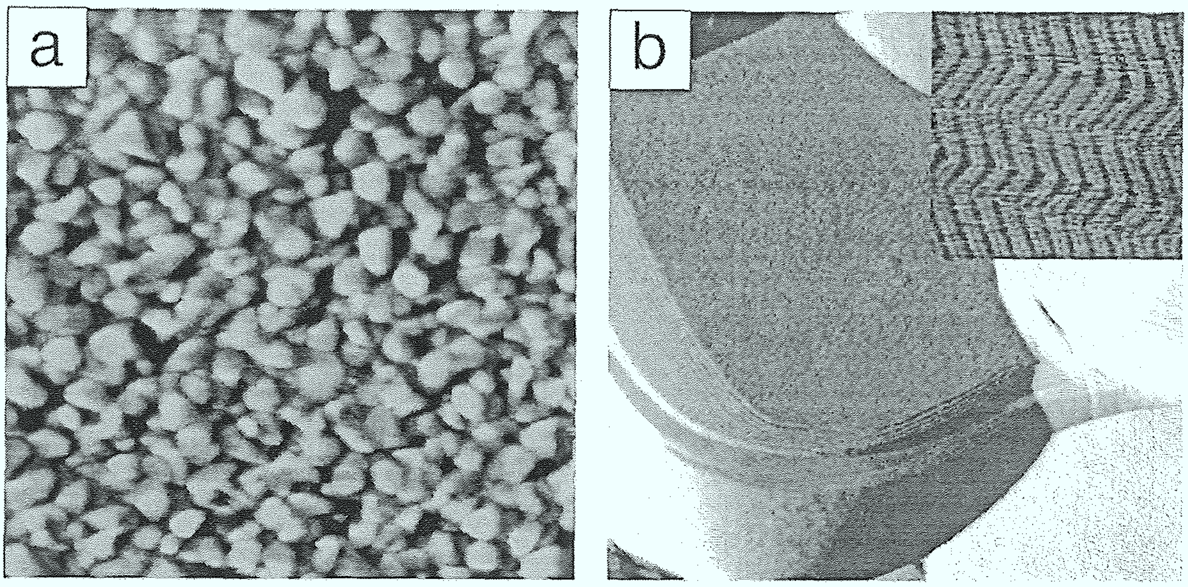

Figure 2.3: (a) The gold thin film sample without further preparation after deposition (6000 × 6000 Å). Tunneling parameters: V_t=400 mV, I_t=1.0 nA. (b) The gold thin film sample after flame annealing (6000 × 6000 Å, V_t=400 mV, I_t=1.5 nA). The inset reveals the reconstruction patterns on the large terraces (800 × 800 Å, V_t=20 mV, I_t=20 nA).

these samples were tested and reviewed in a recent work [23]. It was concluded that the epitaxial growth of gold films on mica were one of the best choices for use as substrates in UHV-STM studies. The samples can be either stored in a contamination-free environment or cleaned by *in-situ* sputtering and annealing. To overcome the difficulty of storing this kind of samples in air, Hegner et al. [24] have developed a stripping method which can produce very large atomically flat surfaces. The preparation and characterization of thin gold films deposited on quartz was investigated in this thesis. The results showed that this kind of sample can also serve as an excellent substrate particularly for STM studies in air.

The deposition of gold films was carried out at the Insititut für Schicht und Ionentechnik (ISI) at Forschungszentrum Jülich. Deposition pressures were $5 \cdot 10^{-5}$ mbar. Gold was evaporated at a rate of about 10 Å/s, and during evaporation the substrate was held at room temperature. The film thickness (about 2000 Å) was monitored by a quartz crystal thickness controller. In order to improve the adhesion of gold films to the quartz substrate, 20 Å of chromium have been deposited on the clean quartz prior to the evaporation of gold.

After deposition without annealing, the STM analysis showed that these films consist of small grains with a typical diameter of about 100-500 Å, as in Fig. 2.3a. After short annealing in a butane flame (30-40 seconds at$\sim$ 1000K) and then cooling down in air, the average grain size is significantly increased and large facets with (111) orientation are formed. Fig. 2.3b shows the representative surface morphology of such an annealed gold thin film sample. The large atomically flat terrace in the center of the image extends over $\sim$ 4000 Å. On these large terraces the characteristic $(22 \times \sqrt{3})$ gold surface reconstruction was routinely observed. The inset in the top right corner of Fig. 2.3b reveals the detail of this reconstruction pattern, which is similar to the image shown in Fig. 2.2b obtained from the gold single crystal surface. The STM characterization on the annealed samples based on a large number of experiments clearly shows that the surface morphology of this kind of samples is very similar to the surface of Au(111) single crystals. Most importantly, the presence of the surface reconstruction on the facets indicates the cleanness of the sample surface. Therefore, these low-cost, easily prepared samples can be used as ideal substitutes for gold single crystals in the STM studies.

Chapter 3

Surface morphology of Au(111) imaged under ambient conditions

3.1 Introduction

Clean surfaces of crystals are usually found to have a different structure from the one of simply truncated bulk crystal. Due to the lack of neighbor atoms, surface atoms are exposed to the influence of forces different from those in the bulk. This leads in most cases to a relaxation or reconstruction in the surface region. In the bulk noble metals there exist two types of forces: one is a pairwise repulsion between the atoms due to the full d shells, the other is a multi-atom electron gas attraction due to the sp electrons and the sp-d hybridization. At the surface the local electron density is reduced which leads to a redistribution of the sp electrons [25]. This redistribution favors a reduction of the interatomic distances of the surface atoms. The atoms in the interior of the solid have a tendency to keep the top layer in registry. Therefore, the surface is under a considerable amount of tensile stress. This surface stress is often thought to be a driving force of the surface reconstruction.

Gold surfaces have a unique position among the studies of surface reconstructions from both theoretical and experimental point of views:
(i) All three low-index gold surfaces reconstruct. Au(111) is the only surface among the (111) surfaces of the fcc metals which is known to be naturally reconstructed at room temperature [26, 27].
(ii) The $(22 \times \sqrt{3})$ reconstruction of Au(111) is thought to be able to relief the surface stress induced by the substrate upon the formation of a free surface [28].
(iii) There is, in addition, a "herringbone" long-range superstructure associated with this reconstruction, which is attributed to "stress domains" and may constitute the first direct observation of stress domains in any physical system [29].
(iv) The "elbows" of the herringbone reconstruction have been found to act as nucleation sites for the growth of metal films on this surface [30, 31, 32].
(v) This reconstruction has been observed not only under ultrahigh vacuum (UHV) conditions [33, 34, 35, 36], but also in air, liquid [21] and electrolyte [37]. Therefore, it can be used as a model system for an STM study under ambient conditions, since the results can be directly compared with those obtained in UHV.

Numerous experimental studies using various kinds of surface science techniques have dealt with the Au(111) surface, as well as a lot of theoretical work. The results can be summarized as follows: There are two kinds of local potential minima for gold atoms at the Au(111) surface, the one is located at the fcc sites (ABC stacking), the other at hcp sites (ABA stacking). Although the two sites are not energetically degenerate, the first-principles calculations showed that the binding energy on the hcp sites is only slightly higher than on fcc sites [38]. By occupation of the two sites in alternating domains, the average interlayer atomic distance can be reduced. The $(22 \times \sqrt{3})$ reconstruction involves the occupation of both sites and the formation of soliton-like walls in the transition regions. The atoms in the transition regions occupy sites other than fcc and hcp, and appear as ridges with a height of about 0.2 Å in the STM image. The widths of the regions with hcp and fcc stacking are not equal due to the energy difference between the fcc and hcp sites. The uniaxial contraction can not relief the surface stress in all directions. This, however, may be accomplished by the long-range superstructure which results from a zigzag periodic bending of the pairwise reconstruction lines by 120° every $\sim$ 300 Å to form the so called *herringbone* or *chevron* pattern. Theoretical studies suggest that the formation of this superstructure may be the results of the competition between two effects: (i) the bending of the reconstruction lines (i.e. the formation of regular domain walls) will cost extra energy; but (ii) the strain relaxation via substrate-mediated long-range elastic interactions will reduce the overall elastic energy [29]. Since the reduction of surface stress is thought to be the main driving force for this reconstruction, the reconstruction structure is found very sensitive to the local changing of the stress distribution (e.g. near structural imperfections) at the surface.

3.2 The $(22 \times \sqrt{3})$ reconstruction of Au(111) imaged in air

The Au(111) surface is a well-suited substrate for adsorption studies, for this reason it has been the subject of many investigations using STM in air, only some of them are listed here [20, 21, 24, 39, 40, 41, 42, 43, 44]. To our knowledge, only few of these studies have mentioned the reconstruction. The following reasons may be responsible for this: (i) since the corrugation of the reconstruction lines seen by STM is rather small (0.15-0.2 Å), it can be easily buried in the large noise usually encountered with STM operated in air; (ii) only the *clean* surface undergoes this reconstruction; if the sample is not properly prepared or contaminated under ambient conditions, the reconstruction does not develop.

In this chapter, the structure and stability of the reconstruction of Au(111) in air has been studied systematically and the results are compared with those obtained in UHV [34, 35]. Fig. 3.1a shows the typical structure of the large terraces of Au(111) samples. Parallel double-lines are seen to run along the $[11\bar{2}]$ direction with a distance between neighboring double-lines of about 65 Å; the distance between the two lines forming the double-line is about 22 Å. The central area marked by the white square was scanned at higher magnification (in the following text, this kind of image will be simply called zoom-in image without additional explanation) and is shown in Fig. 3.1b. It can be seen

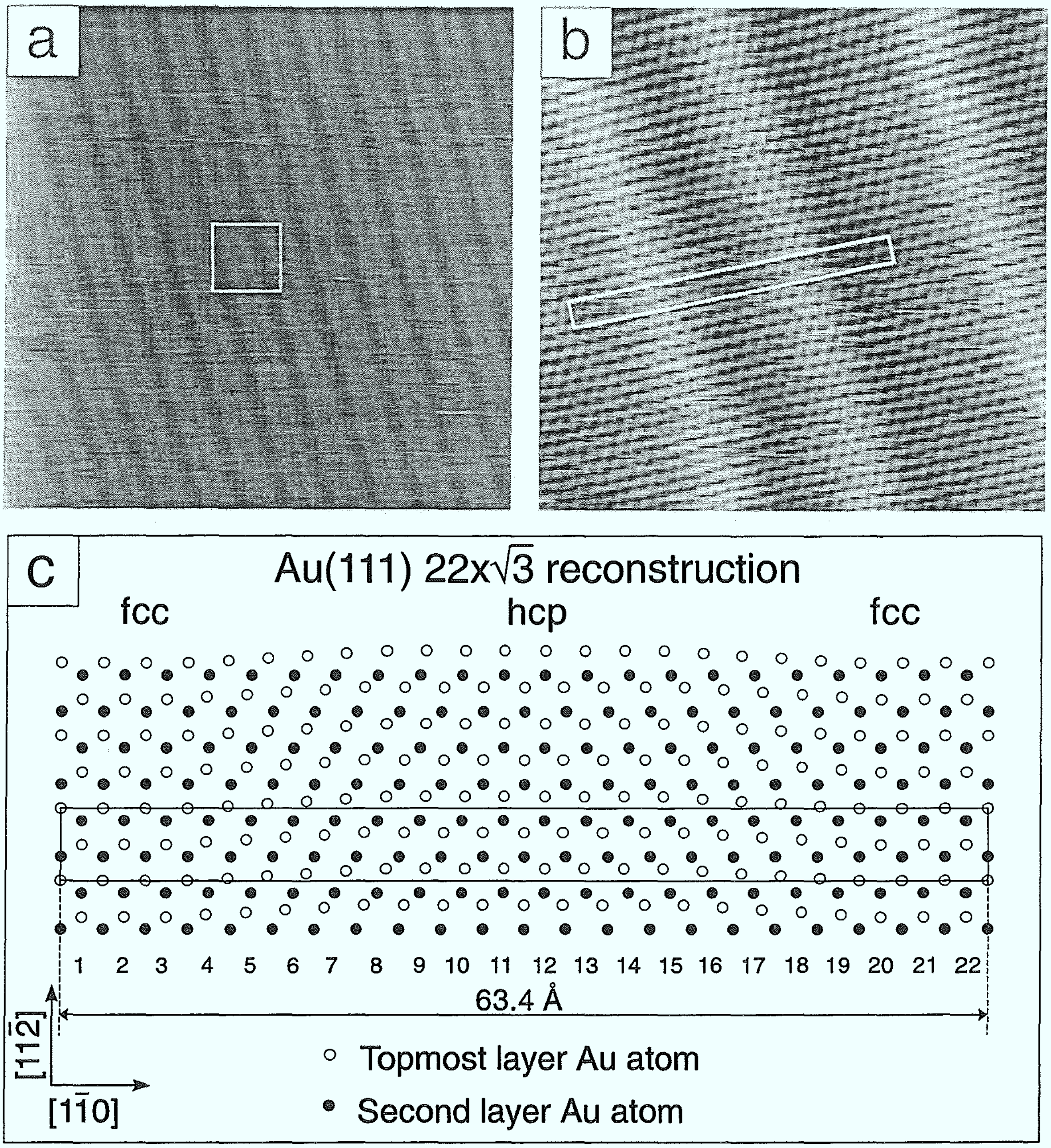

Figure 3.1: (a) STM topograph of the $(22 \times \sqrt{3})$ reconstruction obtained from the gold thin film sample after flame annealing (750 × 750 Å). Tunneling parameters: V_t=10 mV, I_t=15 nA. (b) Zoom-in of the center of the image in (a), revealing the atomic structures of this surface reconstruction (100 × 100 Å). Tunneling parameters: V_t=10 mV, I_t=15 nA. (c) Hard sphere model of the $(22 \times \sqrt{3})$ reconstruction.

that apart from the corrugation lines, a regular hexagonal corrugation characteristic for the closed packed fcc (111) atomic structure can be discerned. Compared with the results in UHV, this can be ascribed to the atomic structure of the reconstruction pattern. The unit cell of the reconstruction has been determined and marked by a white rectangle in the image. Fig. 3.1c shows the hard sphere model of this reconstruction. The length of the unit cell along the $[1\bar{1}0]$ direction measured from STM image is ~ 65 Å, while along the $[11\bar{2}]$ direction it is ~ 5 Å. Also, the lateral displacement of the surface atoms along $[11\bar{2}]$ is clearly evident and is measured to 0.9 Å. Again, the results are in perfect agreement with the results in UHV [35].

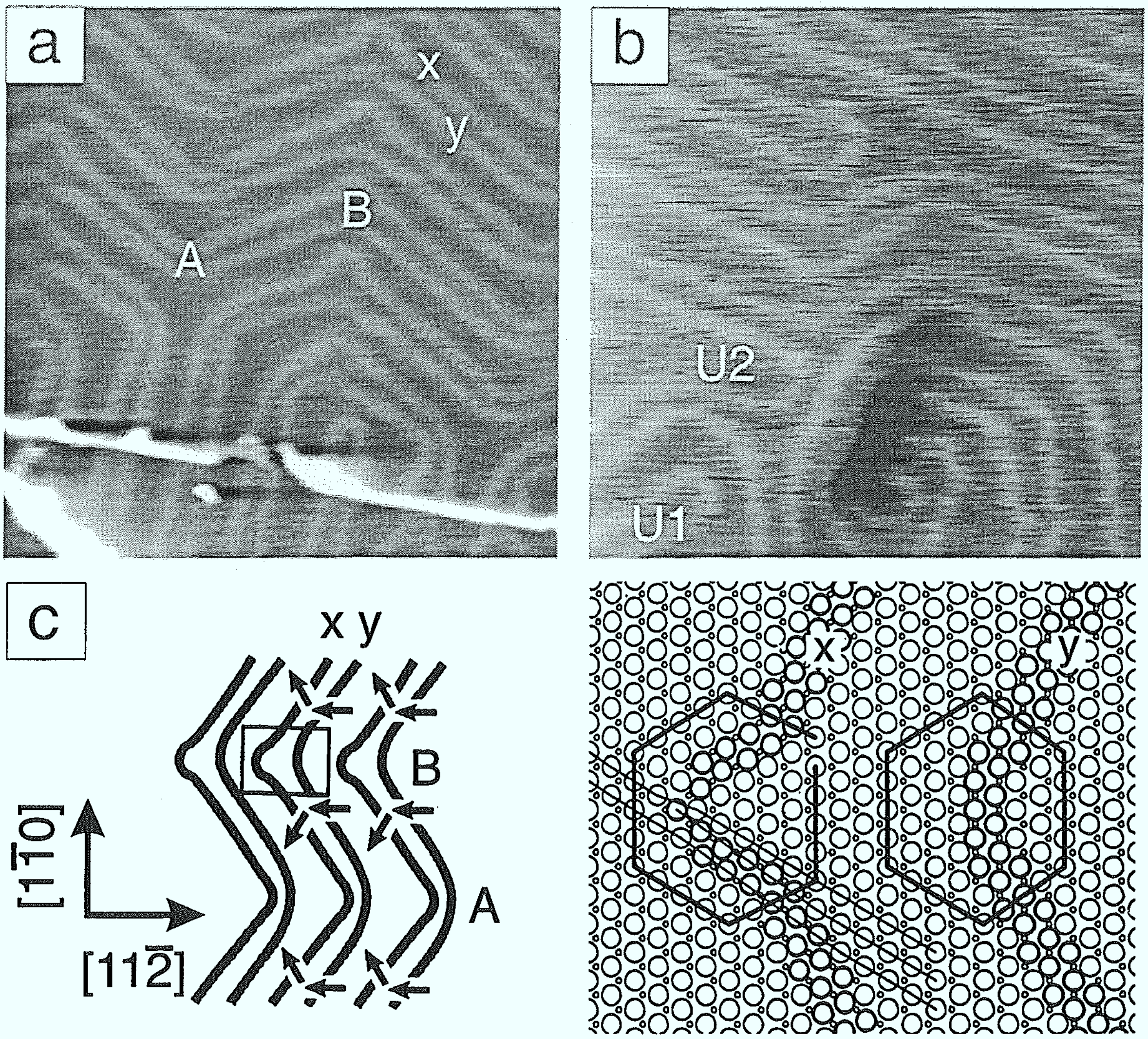

Figure 3.2: (a) The formation of U-turns of herringbone pattern at steps, obtained from Au(111) single crystal surface after annealing in argon at 800°C for 3 h (540 × 540 Å). Tunneling parameters: V_t=60 mV, I_t=10 nA. (b) The influence of screw dislocations on the reconstruction pattern, obtained from the gold thin film sample after flame annealing (420 × 420 Å). Tunneling parameters: V_t=10 mV, I_t=18 nA. (c) Hard sphere model proposed by Chambliss et al. [45].

There are some speculations to explain the atomic resolution obtained at ambient pressure. Since the impinging rate of particles in the gas pressure is so large in this environment ($\sim 10^{23}$ molecules/cm^{2}s), even the most inert surface should be permanently covered by at least one monolayer of adsorbates (e.g. water). In the tunneling process, however, and provided that the tip height is small enough, the STM tip may temporarily push the adsorbates away locally allowing to image the clean surface beneath the adsorbed layer. This explanation is supported by the present experiments and by the results shown in chapter 4.

On the large Au(111) terraces, especially on the well-annealed single crystal surface, a long-range superstructure can often be found. The STM image shown in Fig. 2.2b is an overview of this structure, the image in Fig. 3.2a at higher magnification reveals some additional details. As in Fig. 2.2b, a regular bending of 120° of the $(22 \times \sqrt{3})$ reconstruction domains appears with a domain width of about 150 Å. Within each domain, the registry of surface atoms along the $[1\bar{1}0]$ direction varies between fcc and hcp stacking, the fcc-hcp transitions appear as ridges in the STM images. There are two inequivalent dislocation lines (ridges), labeled x, and y in Fig. 3.2a [45], within the elbows which connect rotationally equivalent domains. Whereas each x-type ridge contains a point dislocation near the elbow, the type y does not. The inequivalence of the two types of ridges also explains the different appearance of domain boundaries, labeled A and B in Fig. 3.2a. On boundary A, the hcp regions are very narrow in contrast to the nearly equal hcp and fcc regions on boundary B. To illustrate this structure more clearly, we attach the hard sphere model proposed by Chambliss et al. in Fig. 3.2c [45]. As mentioned above, the point-dislocations in the elbows have been found to serve as nucleation centers in the growth of metal overlayers (Fe, Co) on the reconstructed surface.

3.3 Interactions of the reconstruction with surface imperfections

Similar to the situation in UHV, another type of domain boundaries, namely, 'U-turns', can be observed, in particular near the structural imperfections such as steps or screw-dislocations (Fig. 3.2). There are two types of U-turns, which are labeled U1 and U2 in Fig. 3.2b. The U1-turns connect the two lines in a dislocation pair (double-lines); the U2-turns connect the lines from adjacent pairs of double-lines. Because the areas surrounding the two types of U-turns correspond to different stacking regions, either fcc or hcp, the two types of U connections can not coexist in the direct neighborhood. As indicated already in Ref. [35], adjacent U-turns of different type must be separated by a single corrugation line in between. This situation is also observed here. Furthermore, the modification of the reconstruction in the vicinity of a screw dislocation is clearly illustrated in this image. The appearance of this twofold screw dislocation changes the strain field locally, the corrugation lines have to bend around the dislocation center to relief the local stress more uniformly.

In most cases, the reconstruction lines try to keep a perfect phase correlation when crossing surface steps. This trend is clearly evidenced in Fig. 3.3. Two monatomic

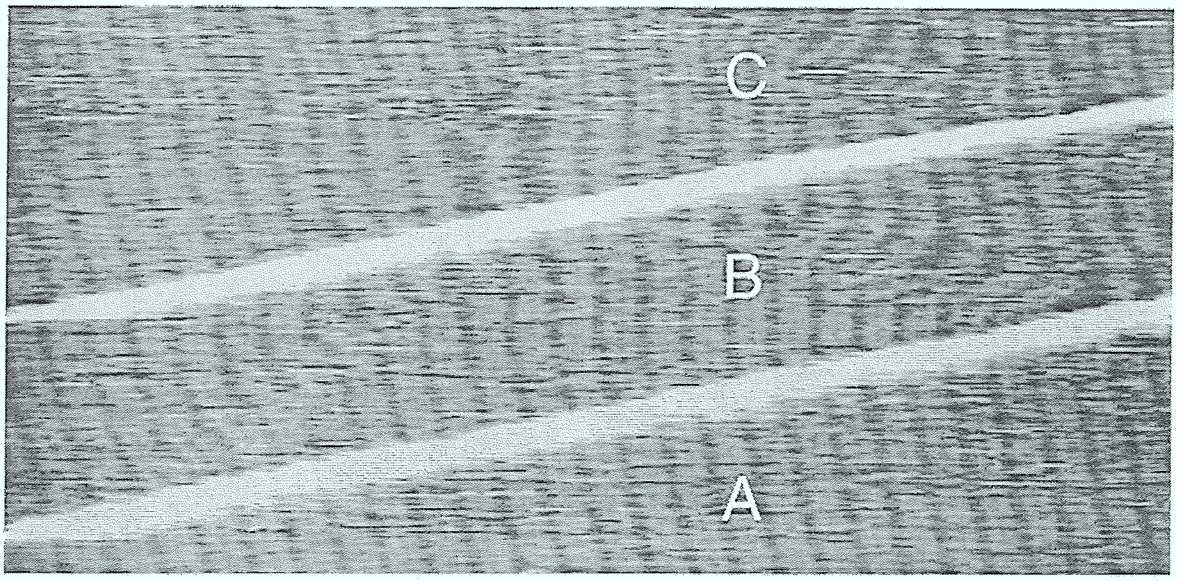

Figure 3.3: Interactions between reconstruction lines and steps, obtained from the gold thin film sample after flame annealing (1850 × 900 Å). Tunneling parameters: V_t=20 mV, I_t=20 nA.

steps separate the terraces A, B and C that are all reconstructed. Most of the double-lines on terrace A are "in-phase" with those on terrace B, except the two pairs at the right side of the image, which form most likely U-turns due to the dislocation in the reconstruction pattern on the B terrace. Because of an additional distortion of the reconstruction pattern located near the step in the center part of the terrace C, the reconstruction double-lines in the middle terrace B can not run straightly and simultaneous keep in phase with both the lines on terraces C and A as they would usually do. Instead, they bend around locally, trying to keep the registry at the steps with the reconstruction lines on the upper and lower terrace. The observation here indicates that the energy cost associated with bending of the reconstruction lines is lower than the loss of registry at the steps.

3.4 Mobility and decay of the reconstruction and monolayer islands in air

The experimental results obtained in UHV showed that the $(22 \times \sqrt{3})$ reconstruction is very stable and usually no change of the pattern caused by the scanning tip was observed. Only after an intentional perturbation by means of the STM tip, the pattern would rearrange itself during the relaxation process [46]. Although in most cases, even in air, the reconstruction is also found to be stable against the perturbation induced by the scanning tip, the observations presented below demonstrate that the reconstruction patterns in air have much higher mobility than in UHV, particularly at structural imperfections.

In the central area of Fig. 3.4a, there are three U-turns (U1-type), which are marked by white arrows. Two of them forms a closed loop structure. This kind of structure is

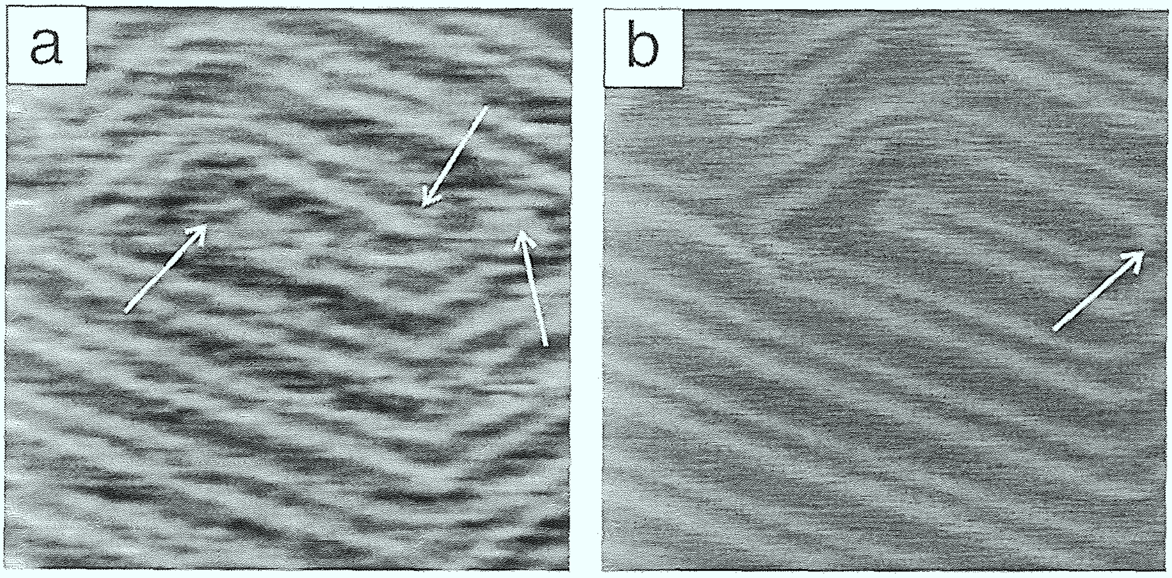

Figure 3.4: Time-lapse STM images revealing the mobility of the reconstruction under ambient conditions, obtained from the gold thin film sample after flame annealing (both images: 410 × 410 Å, V_t=10 mV, I_t=15 nA).

most likely energetically unfavorable. After a short period of time (two scans), one end of the loop connects to the other U-turn close to it. In this way a U-turn of double-lines (marked by the arrow) is left behind in the image shown in Fig. 3.4b. No significant change of the reconstruction pattern in Fig. 3.4b was observed even after many scans. In other cases, the rearrangement of reconstruction patterns over much larger scales was also found.

Usually, no significant deterioration of the reconstruction is observed even several hours after preparation. In some rare cases, e.g. if the humidity is very high, a phase transition of the reconstructed $(22 \times \sqrt{3})$ to the unreconstructed (1×1) surface can be observed on the freshly prepared gold film samples. This "deconstruction" process is illustrated by the sequence of images presented in Fig. 3.5. The high stability of our instrument (drift < 10 Å/min) allows to perform time-lapse STM investigations on the decay of the reconstruction pattern over an extended period of time. The six images presented in Fig. 3.5 are chosen from such a time-lapse series. The time interval between Fig. 3.5a and 3.5f was 60 minutes and the number of scans recorded between them was 18. The decay process of the reconstruction is clearly observed.

From a number of such studies several features of the deconstruction phase transition process in air have been inferred. We find that the transformation usually starts at the imperfectly reconstructed regions. In the lower right part of the image in Fig. 3.5a, there is a narrow (1×1) region surrounded by the reconstructed area, the decay of the pattern was found to proceed from this region. In other cases, the deconstruction process is found to start from step edges. The scanning tip also plays an important role in the transition process: even though the presence of the scanning tip cannot be alone responsible for the deconstruction process, it can at least accelerate it. This has been verified by observations in which the reconstruction lines were still visible in the

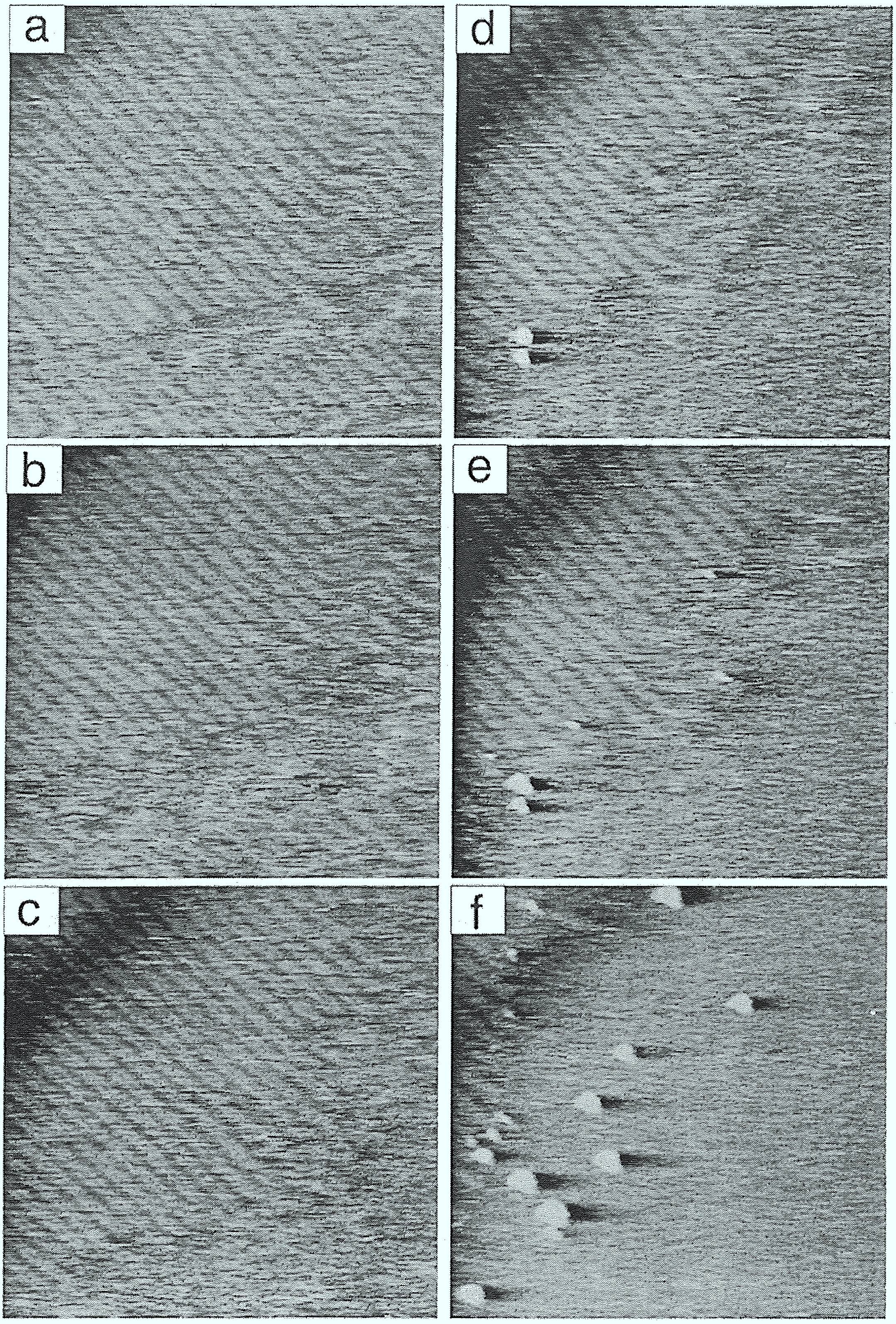

Figure 3.5: Time-lapse STM images show the "deconstruction" process, obtained from the gold thin film sample after flame annealing (1400 × 1400 Å). Tunneling parameters: V_t=85 mV, I_t=12 nA.

area which was not scanned before, while in the scanned area the reconstruction had already been lifted. The coexistence of the $(22 \times \sqrt{3})$ and (1×1) phases indicates that the deconstruction is a first order phase transition. During the transition, extra atoms in the higher density reconstructed phase will be squeezed out and can nucleate into monolayer high gold islands on the surface as seen in Figs. 3.5d-f. These islands at room temperature are usually metastable; they can easily diffuse to the steps and be trapped there.

There is strong evidence that the presence of adsorbates can lift the reconstruction. However, from our experiments it was not possible to determine which adsorbates may be responsible for the lifting. There are some clues that water molecules are involved: Early studies showed that the adsorption of wet air on gold surfaces induces a change of the work function [47]. In our experiments the lifting of the reconstruction appeared always to be associated with a high air humidity. Finally, studies of the same reconstruction in electrolyte found a similar phase transition when the surface potential was raised [48]. It has been speculated that in the presence of a water film on the sample surface, the biased tip may be compared with the electrode in the electrolyte cell. This may partially explain the fact that the presence of the scanning tip will accelerate the $(22 \times \sqrt{3})$ to (1×1) deconstruction of the Au(111) in air.

The monolayer islands on the Au(111) surface under ambient conditions were found to decay in a different way as in UHV. As reported in previous studies [49, 50], the area of monolayer islands decays linearly with time at room temperature in air. We observed similar results on our Au(111) samples. Figure 3.6 shows time-lapse sequence of images obtained from the gold thin film sample after flame annealing, revealing the decay of a monolayer island and the change of surface morphology. Michely et al. reported that: When gold surfaces are imaged in air, a significant diffusion of steps is observed which may be stimulated by the STM tip in the presence of adsorbates. In contrast, small structures on Au(111) under UHV conditions were found only slightly changed after tenth of scans [51]. The observations from STM images in Fig. 3.6a-f are in consistent with these previous results. In fact, the absence of the $(22 \times \sqrt{3})$ reconstruction on the terraces indicates that this surface is no longer the *clean* Au(111) surface. Apart from the decay of the island, the step movements are clearly visible from this series. Fig. 3.6g shows a plot of the area of the monolayer island (arrow) shown in the images as a function of time. It can be seen that the data is well fitted with a linear function, with a decay rate of -5.5 ± 0.3 atoms/s.

The mechanism of linear decay of clusters was discussed in Refs. [49, 50]. The concentration of adatoms in the vicinity of the island is higher than that in the vicinity of a straight step edge. The decay of the clusters is a balance between the detachment rate of the atoms from the cluster edge and the surface diffusion rate. The radius of the cluster r can be expressed as a function of time t through the scaling law [49]:

$$r \propto (t_0 - t)^n, \tag{3.1}$$

for $t < t_0$, where t_0 is the time at which the cluster disappears. There are two cases with different exponents: (i) the *diffusion-limited* case, in which the detachment rate of adatoms from the cluster edge is rapid than the rate of diffusion, and the exponent

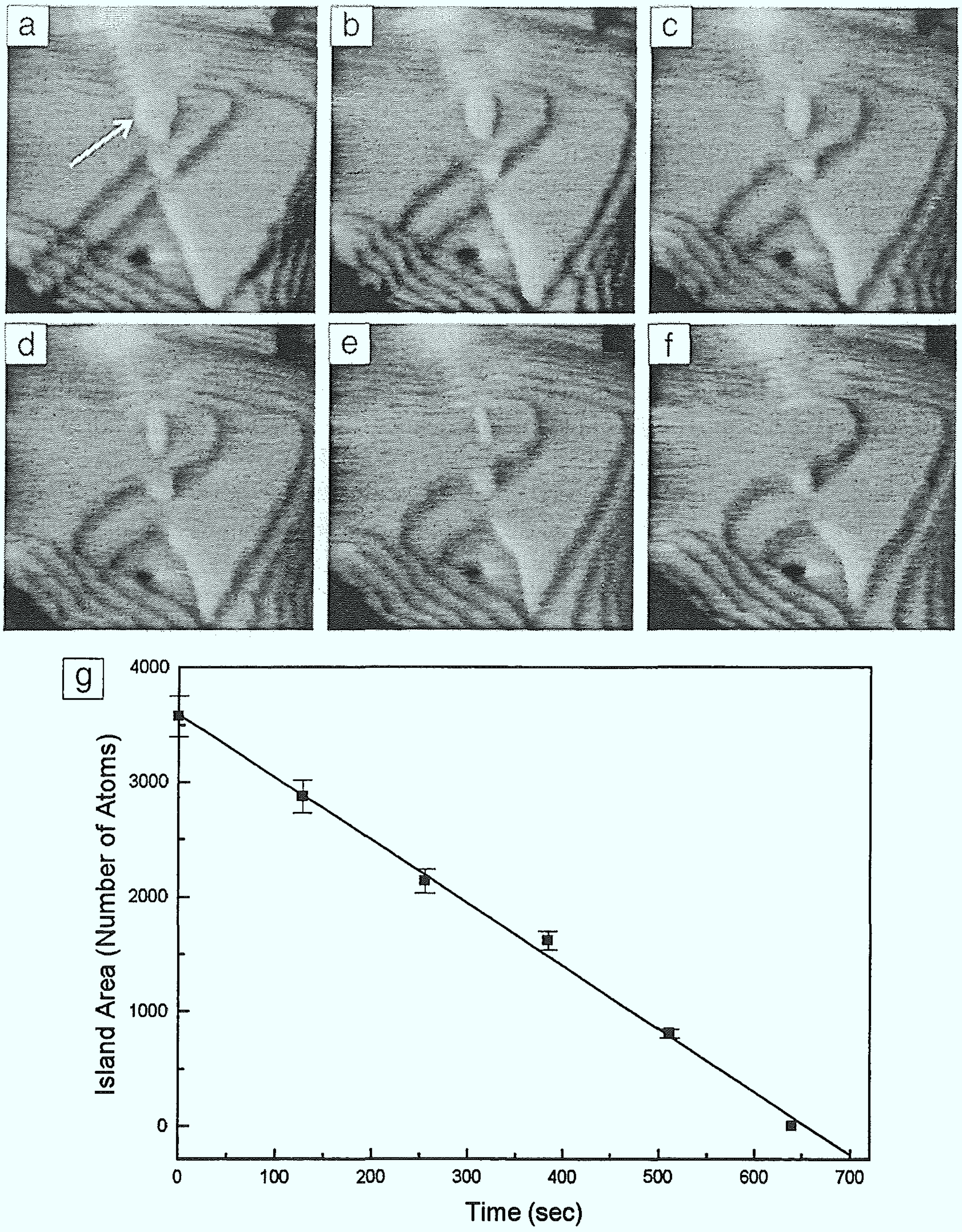

Figure 3.6: (a)-(f) Decay of a monolayer island observed by time-lapse STM images, obtained from the gold thin film sample after flame annealing (1200 × 1200 Å). Tunneling parameters: V_t=200 mV, I_t=5.3 nA. (g) Plot of the island area shown in (a)-(f) as a funtion of time.

$n = 1/3$. This case is indeed observed recently on the Ag/Ag(111) system [52]. (ii) the *interface-transfer-limited* case, in which the detachment rate of adatoms from the cluster edge is slow compared to the rate of diffusion, and the exponent $n = 1/2$. The observation of a linear decay of the island areas clearly demonstrate that this is an interface-transfer-limited case. However, as discussed by Morgenstern et al. , the decay of islands on *clean* metal surfaces is usually assumed to be not in the interface-transfer-limited case, since there is no additional barrier for the attachment of adatoms to an *ascending* step, and the decay of islands should be diffusion limited. Due to the existence of a step edge barrier, the downward diffusion of adatoms across steps were not observed in the Ag(111) case. This may imply that the adatoms most likely diffuse to the ascending steps and the decay of islands is found indeed to be diffusion limited, $n = 1/3$.

The linear decay behavior on Au(111) observed in this case is actually not in contradiction to the results on the Ag(111) surface. Since the presence of the adsorbates on the surface may lower the step barrier, as reported in the case of oxygen adsorbed on Pt(111) [53], the adatoms in our case could possibly diffuse across *descending* steps. The observed change of the shape of the terrace directly under the monolayer island provides evidence for the occurring of such a process. The possibility that adatoms can diffuse across descending steps will lead to a increase of diffusion rate, particularly in this case, where the island is almost surrounded by the descending steps. On the other hand, due to the presence of an additional barrier for the attachment of adatoms to descending steps, the decay of islands may become interface-transfer-limited. Actually, in a Monte Carlo simulation study, Dubson et al. show that the linear decay of monolayer islands may arise from a competition of the following factors [50]: (i) the detachment of adatoms from kink sites; (ii) the rate of absorption of adatoms by a outer ledge (descending steps) and (iii) the rate of the reattachment to the island. It can be seen that, the presence of adsorbates on the surface will strongly affect all the three factors and therefore, the observation of the linear decay of islands on *adsobate covered* surfaces can be understood. Furthermore, the decay rate of -5.5 ± 0.3 atoms/s observed here is much larger than the rate of -0.106±0.016 reported by Peale et al. [49]. Apart from the different geometry and maybe different adsorbates involved in the two cases, we could not exclude that the influence of the STM tip may be responsibile for the large decay rate observed in our case.

In a recent study, Fournel et al. report the observation of large morphological changes of Au(111) surfaces, and they suggest that these changes are due to the gold atoms transferred from steps on the surface to the STM tip [54]. From our experimental observations, such a process appears to be unreasonable at least in the case discussed above.

3.5 Conclusions

The work presented in this chapter demonstrates that the combination of reliable tip, well-controlled preparation of sample and excellent instrumental stability allows our "ambient" STM to routinely provide high quality and reliable results. The observations of reconstruction patterns at both large and atomic scales by STM in air can be directly compared with those obtained in UHV. Due to its unique reconstruction, Au(111) serves as an ideal model system for evaluating the performance of STM operated in ambient environments. Moreover, the presence of the reconstruction is a sensitive measure of the cleanliness and structural perfection of the sample surface. In most cases, the morphologies and stability of the reconstruction of Au(111) in air show strong similarities with those in UHV. Due to the presence of adsorbates, the mobility of the reconstruction patterns is rather high, particularly at structural imperfections. In rare cases, the decay of the reconstruction and a phase transition from the $(22 \times \sqrt{3})$ into a (1×1) phase were also observed on the freshly prepared samples. Because of the presence of adsorbates, the decay of monolayer islands are found to have a linear behavior, which indicates that the decay process is interface-transfer-limited.

Chapter 4

Iodine adlayer structures on Au(111)

4.1 Introduction

Iodine adsorption on the Au(111) surface has been studied intensively since the early 1980s. The investigations were performed under various conditions and using different experimental methods. The iodine structures were studied by low energy electron diffraction (LEED) in UHV [55], and ex-situ following emersion from iodide solutions under potential control [56]. Recently, scanning tunneling microscopy was employed to study this system in aqueous solutions under electrode potential control [57, 58] as well as in organic polar solvents and in air [59, 60]. The results obtained from LEED and surface X-ray diffraction (XRD) [61, 62] in reciprocal space combined with those in real space using STM should, in principle, enable the exact determination of the iodine adlayer structures. However, due to the complexity of this system, there are still some uncertainties in the published results. In the low coverage range, the $(\sqrt{3} \times \sqrt{3})\mathrm{R}30^\circ$ structure reported by LEED and STM was not observed in the XRD measurements. At higher coverage, a $(5 \times \sqrt{3})$ structure was found by LEED and STM [56, 57, 59], while a (3×3) structure was also reported [58]. In the corresponding coverage range, the XRD results suggested a $(p \times \sqrt{3})$ phase which compresses continuously with increasing potential in the electrolyte cell. Furthermore, near iodine monolayer saturation coverage, XRD experiments found a rotated-hexagonal incommensurate phase, whereas a high-order commensurate $(7 \times 7)\mathrm{R}21.8^\circ$ structure was also suggested as a possible model to describe the moiré-like pattern observed by STM [57, 59].

The structure and phase diagram of iodine adsorbed on Au(111) is to some extent comparable to that of physisorbed rare gas adlayers on graphite and single-crystal metal surfaces [64, 65]. Therefore, I/Au(111) can be used as a model system to study 2D phenomena such as commensurate-incommensurate (C-I) phase transitions of the surface structures. The study of iodine adsorption also finds practical applications, for example, as protective coating of platinum single crystal surfaces [66]. One important advantage of this system is its stability: It can be investigated in UHV, as well as in electrolytic solutions and under ambient conditions. Comparing the phase diagram of I/Au(111) as a function of coverage and temperature obtained under different experimental conditions will further advance the understanding of 2D systems in general.

From the results of a combined LEED and Auger study [55], it is known that the desorption of iodine atoms in the monolayer coverage range from the Au(111) surface only starts at about 200°C. Obviously, adsorption at room temperature is essentially irreversible, and the desired coverage can be reached by adding successive iodine doses onto the gold substrate. The iodine adlayer was formed by putting droplets of an iodine solution in methanol on the freshly annealed gold thin film sample. The concentration of the solution was in the range of 0.01-1mM. The iodine surface coverage was controlled by either consecutive deposition on the same sample between the STM measurements, or by putting more or fewer droplets on different samples. Using this procedure various iodine adlayer structures corresponding to different monolayer coverages can be obtained. The results reveal that with increasing coverage the commensurate iodine $(\sqrt{3} \times \sqrt{3})$R30° structure first transforms into a continuously compressed (striped) incommensurate phase $(p \times \sqrt{3})$. Near monolayer saturation coverage the iodine atoms are forced to adsorb on other type of sites and the adlayer forms a hexagonal moiré-like pattern with a long-range height modulation. In the intermediate coverage range, the iodine adlayers were found to be not well-ordered. The coexistence of the striped $(p \times \sqrt{3})$ structure and the hexagonally compressed modulated structure in different regions on the same surface may indicate that the corresponding phase transition is of first order. The present study complements the previous investigations of this system in air. Also, some of the STM-results are found to be in accord with the recent XRD measurements on this system in electrolyte under potential control [62].

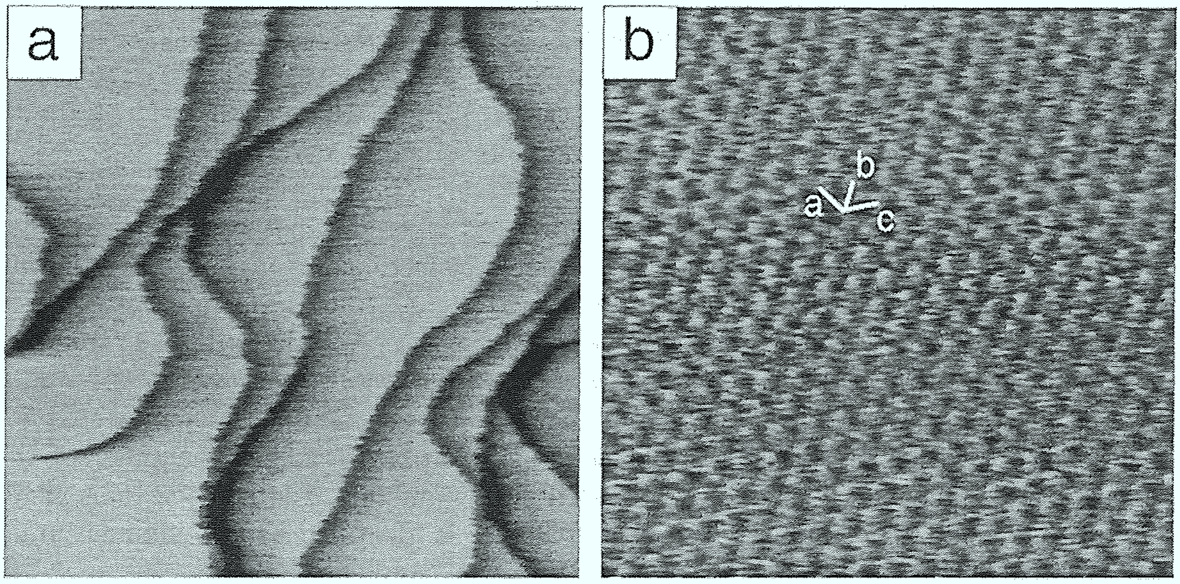

Figure 4.1: (a) "Frizzy" monatomic steps meander on the surface after iodine adsorption (1600×1600 Å). Tunneling parameters: V_t=200 mV, I_t=5.4 nA. (b) Atomic resolution image of the (1×1) Au(111) surface (52 × 52 Å). Tunneling parameters: V_t=10 mV, I_t=10 nA.

4.2 $(p \times \sqrt{3})$ structure

After iodine adsorption the Au(111) surface was found to be transformed into the 'deconstructed' (1×1) phase. At small iodine coverage ($\theta < 0.33$), iodine atoms are distributed randomly on the surface and could not be directly imaged with STM due to their high mobility at room temperature. Apparently, iodine adsorption increases the mobility of the atoms at the steps on the Au(111) substrate, similar to the case of Na adsorption on Au(111) [63], since the surface steps are no longer straight and parallel to the Au(111) high symmetry $[1\bar{1}0]$ directions. Instead, they meander on the surface and become "frizzy". This situation is illustrated in Fig. 4.1a. At the atomic scale (Fig. 4.1b), a well-ordered hexagonal lattice with nearest-neighbor spacing (NNS) of $a = b$=2.9 Å and c=2.7 Å is observed, which is ascribed as the atomic structure of the unreconstructed Au(111) surface. Due to the mechanical asymmetry of the STM-scanning head, there is a slight distortion in the observed hexagonal structure which, in principle, could be corrected using the known lattice parameters of the Au(111) surface (a_{Au}=2.884 Å). We have measured the average NNSs and used these values to calculate the area of a unit cell and, hence the number of Au surface atoms in each image. The number of atoms in images of the same scan size as in Fig. 4.1b is calculated to 400±10, which will be used as the reference to determine local iodine coverage.

The first stable iodine adlayer structure is observed when the iodine coverage reaches $\theta \simeq 0.33$. At this coverage the iodine adatoms are forced into registry (most likely into three-fold sites) on the Au(111) to form a $(\sqrt{3} \times \sqrt{3})$R30° surface structure. The image shown in Fig. 4.2a depicts an approximate hexagonal lattice with the measured NNS along the three high symmetry directions being a=5.1 Å, b=4.8 Å and c=5.0 Å, respectively. These NNSs are close to the value of $\sqrt{3}a_{\mathrm{Au}}$=5.0 Å expected for the $(\sqrt{3} \times \sqrt{3})$R30° structure. To determine the local coverage, the number of the atoms in this image is calculated and divided by the number of substrate atoms yielding $\theta = 0.32 \pm 0.01$. Thus, the observed structure is identified as the commensurate $(\sqrt{3} \times \sqrt{3})$R30° structure.

If the iodine coverage is only slightly increased above θ=0.33, the adlayer structures will also change correspondingly. The $(5 \times \sqrt{3})$ structure reported in the previous LEED and STM study [56, 57], and the $(p \times \sqrt{3})$ found in XRD measurements [62] both suggest a uniaxial compression of the $(\sqrt{3} \times \sqrt{3})$R30° structure to form a striped phase. This situation is similar to the behavior of the Xe/Pt(111) system, for which the symmetry breaking commensurate-incommensurate (C-I) transition from a commensurate $(\sqrt{3} \times \sqrt{3})$R30° structure into a striped domain wall phase has been observed [65]. Theoretical studies predict this transition to be of second order, if the compression is indeed uniaxial, i.e. if the domain walls are parallel to one another [67].

At first glance, the STM image in Fig. 4.2b is similar to its counterpart in Fig. 4.2a. Further analysis, however, reveals that the hexagonal lattice is slightly distorted. To determine this kind of structure more accurately, the "selective imaging" method was used [59, 68]. By simply changing the tunneling parameters, either the iodine adlayer or the substrate lattice can be imaged at the same place. In this way, the adlattice properties such as periodicity, orientation and local coverage can be determined with

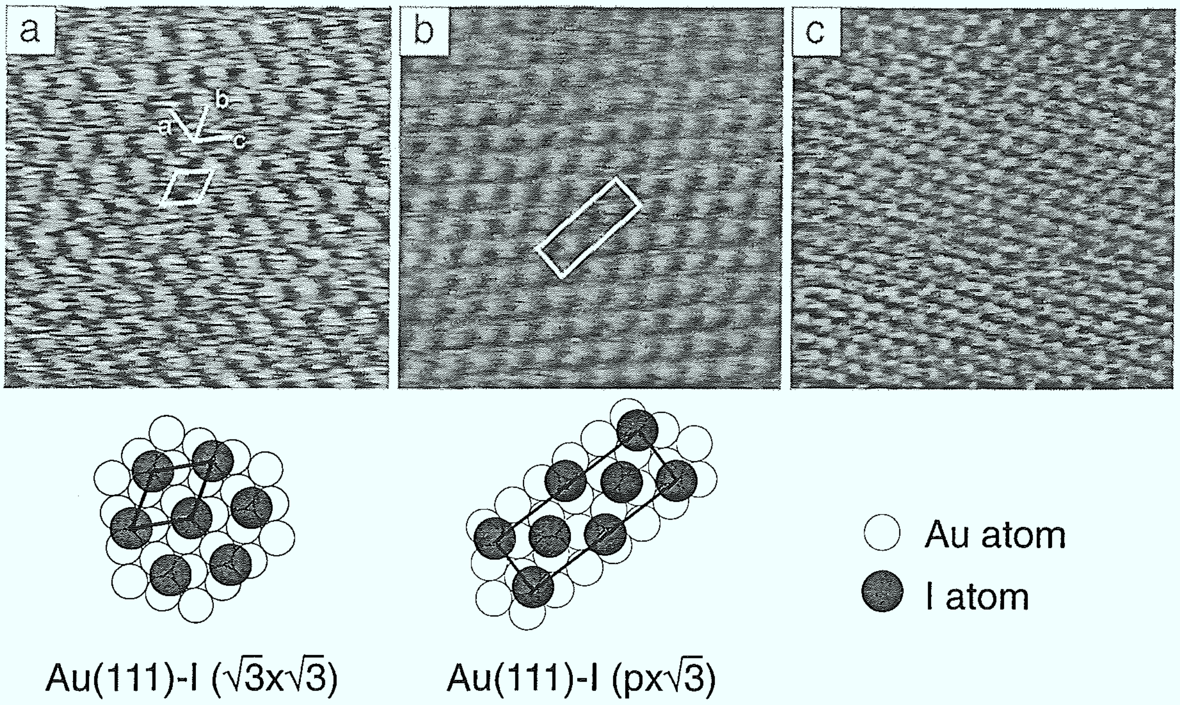

Figure 4.2: (a) The approximate $(\sqrt{3}\times\sqrt{3})$R30° structure (52×52 Å). Tunneling parameters: V_t=10 mV, I_t=3.8 nA. (b) $(p\times\sqrt{3})$ (p=5) structure (52 × 52 Å). Tunneling parameters: V_t=10 mV, I_t=7 nA. (c) "Selective imaging" of the Au(111) substrate at the same place as (b) (52×52 Å). Tunneling parameters: V_t=10 mV, I_t=29 nA.

high precision. Directly after the acquisition of Fig. 4.2b, the tunneling current was increased from 7 nA to 29 nA at constant voltage, corresponding to a decrease of the tunneling gap impedance from 1.4 MΩ to 0.34 MΩ. The image then obtained is shown in Fig. 4.2c. It is obvious that this image with the average NNS of 2.8±0.1 Å is very similar to the one presented in Fig. 4.1b: it represents the unreconstructed Au(111) lattice. With the reference of the gold lattice, the iodine structure in Fig. 4.2b can be easily determined. It is found that the distance between the atoms along the rows running from the upper left towards the lower right corner maintain the commensurate NNS (5.0 Å), while the atomic spacing in the other two rows are reduced to a value of 4.4 Å. This value is close to the value of 4.39 Å expected for the $(5\times\sqrt{3})$ structure reported in the previous STM studies [57, 59]. The unit cell is drawn in Fig. 4.2b as a white rectangle. The examination of the images yields a local iodine coverage of $(\theta = 0.40 \pm 0.01)$. The angle between the two compressed iodine rows and the nearest gold close packed direction is measured to 26°, deviating by about 4° from the value characteristic of the $(\sqrt{3}\times\sqrt{3})$R30° structure. The selective imaging process was found to be reproducible with different samples and tips. We could also image the Au substrate by either lowering the bias voltage at constant current or increasing the tunneling current at constant voltage, i.e. it is the decrease of the gap impedance which is responsible for this interesting phenomenon.

A large number of experiments were performed in the coverage range between 0.33

and 0.4. The results show that the adlayer structure is more complex than the simple $(5 \times \sqrt{3})$ structure. While one of the NNS of the iodine lattice seems to always keep the commensurate value of 5.0 Å, the other two can take various values associated with the continuous change of the local coverage. We found that in the coverage range between 0.37 and 0.4, the compression increases with increasing coverage, corresponding to a change of the compressed NNS, which in average varies from 4.6 to 4.4 Å. The values are close to those expected for the $(p \times \sqrt{3})$ structures (with 4 atoms per unit cell) when p=5 (4.39 Å) and p=8 (4.59 Å), respectively. The XRD measurements on I/Au(111) in electrolyte under potential control yielded very similar results. For the $(p \times \sqrt{3})$ phase, XRD found coverages varying from 0.365 to 0.409 with corresponding compressed NNS between 4.62 to 4.32 Å, respectively. It is somewhat surprising to see that similar results are obtained under such different experimental conditions. It can thus be concluded that for the anionic iodine adsorbate, the adlattice structures on low-index single-crystal surfaces are determined by coverage and temperature rather than the particular environment. Although the preparation method prevents us from varying the coverage continuously, the data based on the large number of discrete measurements can to some extent simulate this continuous change of coverage.

The formation of domain walls during the C-I phase transition has been predicted by theoretical studies [69], and observed experimentally for various systems [65, 70]. The LEED study on I/Au(111) reported the observation of the splitting of the original $\sqrt{3}$ beams into triplets at iodine coverage above 0.33, which may be caused by the formation of domain walls [71]. Although the uniaxially compressed structure was seen in STM studies, such domain walls were not observed so far. The STM image shown in Fig. 4.3a together with its Fourier transform and a proposed hard sphere model provides evidence of the existence of such domain walls in this system. As seen in Fig. 4.3a, the NNS along the rows running from upper left to bottom right varies periodically, forming striped arrays running from the lower left towards the top right corner of the image. In the Fourier transform (Fig. 4.3c) of this image, extra spots marked by white circles are clearly observed near the commensurate positions (marked by white rectangles). Further analysis shows that this pattern corresponds to the diffraction pattern expected for a striped phase with superheavy domain walls [71]. Note, that only one out of three equivalent domains is present in the STM image. Therefore, it is reasonable to assume that this is, indeed, a uniaxial compressed domain wall phase.

To determine the structure more accurately, a (1×1) grid is superimposed on this image in such a way, that the iodine atoms in the supposedly $(\sqrt{3} \times \sqrt{3})R30^\circ$ commensurate regions fall right into the three-fold sites of the Au(111) substrate. The position of the atoms within the domain walls can then be determined. A possible hard sphere model for this structure is proposed. Note, that the superstructure unit cell is a $(5 \times \sqrt{3})$ structure. It can be seen that due to the stress induced by the presence of the wall, the atoms within the walls relax by shifting away from it (probably towards the nearest bridge site). This situation is indicated by the small arrows drawn in the ball model. By the atomic relaxation within the domain walls the atoms take positions which close to that of a uniform compression: Comparing the $(5 \times \sqrt{3})$ model presented in Fig. 4.2 with the ball model discussed above, it is clear that the first one is derived from the second one after full relaxation of the domain walls. The strong relaxation may

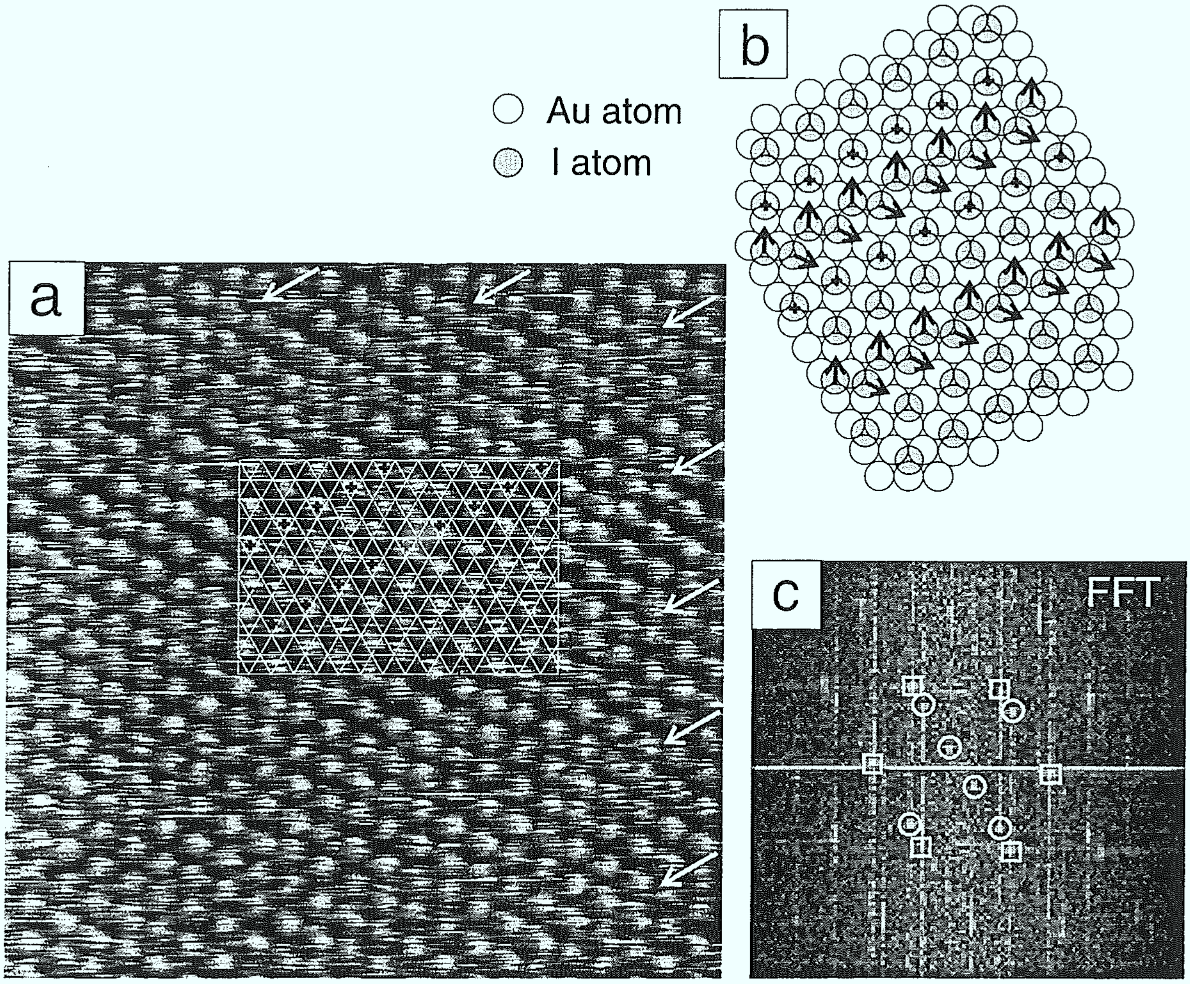

Figure 4.3: (a) STM topograph showing $(\sqrt{3} \times \sqrt{3})$ structure with domain walls (92 × 92 Å). Tunneling parameters: V_t=10 mV, I_t=3.8 nA. (b) Proposed hard sphere model. (c) Fourier transform of image (a).

explain the fact why such domain walls were not observed in the previous STM studies on I/Au(111).

4.3 Moiré-type structures at higher iodine coverage

Haiss et al. [59] found a structure with long-range modulation at iodine saturation coverage $\theta = 0.44$ and suggested a (7×7)R21.8° structure to be a possible model. Also, intermediate structures consisting of patches of local $(5 \times \sqrt{3})$ and moiré-like patterns at coverages around $\theta = 0.42$ are reported. In the same coverage range, XRD measurements found that the adlayer undergoes a first-order transition from the $(p \times \sqrt{3})$ to a hexagonal incommensurate rotated structure at a critical coverage of 0.409. The NNS in this hexagonally compressed phase first increases to 4.43 Å then decreases to 4.3 Å at a coverage of 0.445.

Fig. 4.4a shows an image of a well-ordered iodine lattice at monolayer saturation coverage with clear long-range superperiodicity. The zoom-in image in Fig. 4.4b reveals

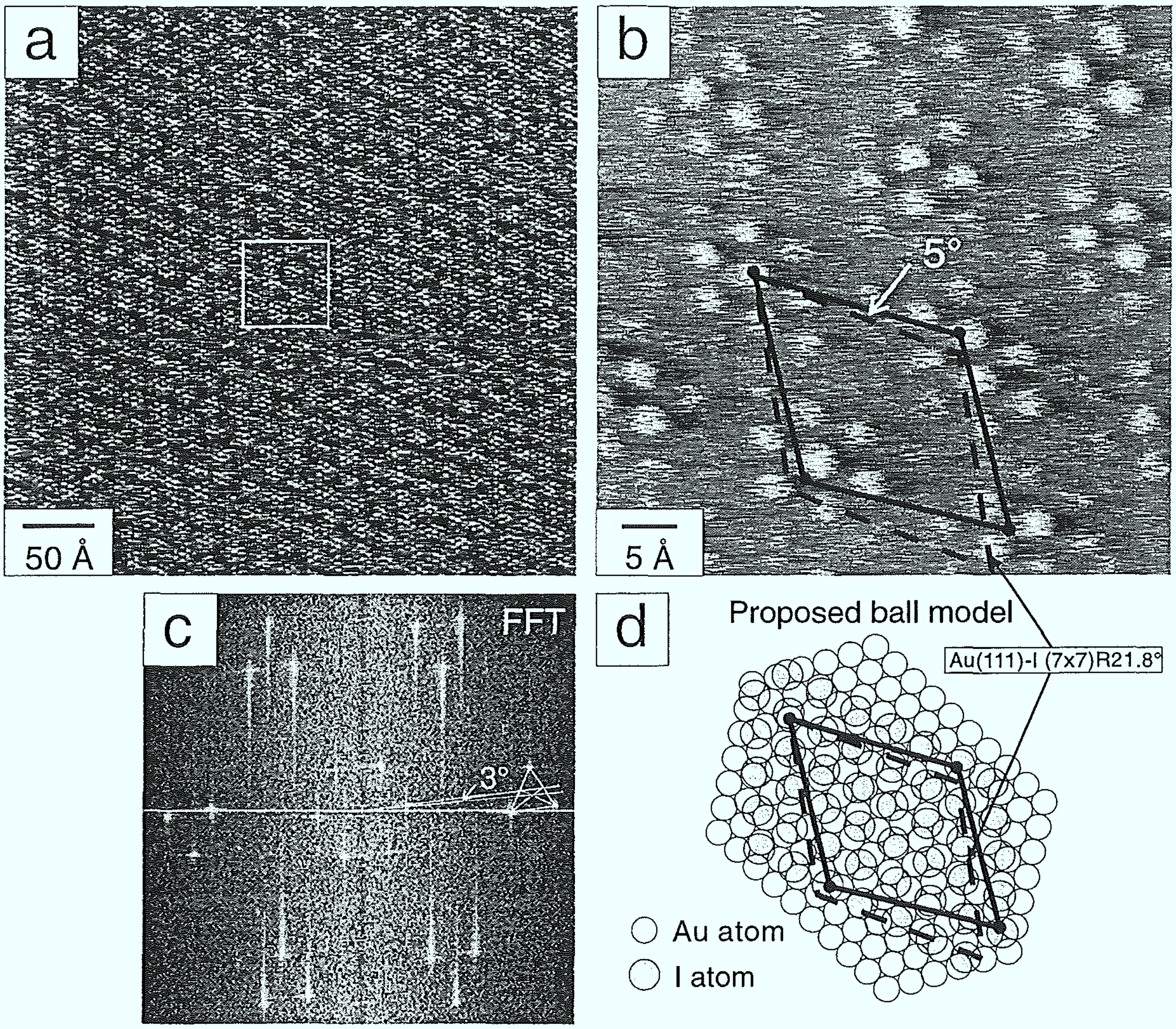

Figure 4.4: STM images of well-ordered Moiré structures at saturation iodine coverage (a) Large-scale overview of this structure (400 × 400 Å). Tunneling parameters: V_t=20 mV, I_t=15 nA. (b) Zoom-in image revealing the atomic structure (52 × 52 Å). Tunneling parameters: V_t=20 mV, I_t=15 nA. (c) Fourier transform image of (a). (d) Proposed hard sphere model for this structure.

the adlayer structure at the atomic scale. The analysis of the Fourier transform (FFT) of Fig. 4.4a (shown in Fig. 4.4c) provides additional information about both the superlattice and the atomic structure. Two sets of spots can be distinguished in the FFT image: the hexagonal set in the center corresponds to the superstructure; the outer spots which are split into triplets reflect the atomic structure. Although these triplets resemble the LEED patterns obtained in UHV from this system [55] and from Kr/graphite [64], we find that this pattern slightly differs from those LEED patterns. In the LEED patterns, one of the spots in the triplets is displaced radially outward along the $\sqrt{3}$ direction in reciprocal space. Also, the off-axis splitting of the other two spots is highly symmetric with respect to this direction, indicating a compression of the adlayer along the $\sqrt{3}$ direction in real space. In the FFT image shown in Fig. 4.4c, it is obvious that if we assume that one of the spots is displaced along the $\sqrt{3}$ direction, the triangle would not be symmetric along this direction. This implies that either the compression is not along the $\sqrt{3}$ direction or that the adlayer is rotated from the exact $\sqrt{3}$ orientation in real space. Such a 'rotational epitaxy' of the adlayer above a critical misfit is in fact predicted by theory [72], and has been observed in many experimental investigations of physisorbed adlayers [65]. If we assume a uniform compression of a rotated lattice, this would imply that the first-order diffraction spots were splitted from the commensurate $\sqrt{3}$ position in such a way that the center of the triplets should remain at the $\sqrt{3}$ position in reciprocal space. This is, indeed, verified by the results presented below. Similarly, the splitting of the $\sqrt{3}$ spot into triplets while keeping the position of the original $\sqrt{3}$ spot at the center of the triangle was observed in a LEED study of S/Ru(0001) system [70]. Then, the orientation and periodicity of the superlattice is easily determined (see Fig. 4.4c). As a result, the superlattice is found to be rotated by about 3° from the R30° direction and has a periodicity of $\sim$ 19 Å. The NNS calculated from the triplet splitting is 4.4±0.1 Å, in excellent agreement with the values obtained in real space from STM topograph in Fig. 4.4b. The coverage is calculated to $\theta \simeq 0.45$, which is believed to be the saturation coverage of iodine on Au(111) [62].

The observed structure is very similar to the high-order commensurate (7×7)R21.8° phase suggested in the previous studies performed in air and electrolyte [57, 59]. It is pointed out that these authors also realized the incommensurate nature of this structure and have observed different periodicities and rotation angles of this hexagonal pattern. Based on the FFT results and the STM images obtained in real space, we propose a hard sphere model presented in Fig. 4.4d for the structure observed here. The unit cell of the (7×7)R21.8° is also indicated (dashed lines). It can be seen that the proposed model slightly deviates from the (7×7)R21.8° by a rotation of 5° and the length of unit cell is reduced from 20.2 Å to $\sim$ 19.5 Å.

Besides the homogeneously compressed phase, other structures which are not well-ordered, were often observed in the range just below the saturation coverage. Fig. 4.5 shows two examples of this kind of structures. As seen in Fig. 4.5a, the adlattice structure differs from the $(p \times \sqrt{3})$ structure due to its local height modulation. On the other hand, this modulation is not very regular as in the case shown in Fig. 4.4. The Fourier transform of this image reveals three sets of spots corresponding to (i) the gold substrate lattice, (ii) the iodine adlattice and (iii) the iodine superlattice. Although the gold substrate is not discernible in the image presented here, it can be observed in the high magnification zoom-in image. With the reference of the gold lattice, the average iodine NNS is determined to be 4.4±0.1 Å. The coverage is $\theta \simeq 0.43$. The adlattice makes an angle of about 26° to the gold substrate. Using this FFT image, we were able to test the assumption made earlier that the center of the triangle should be the $\sqrt{3}$ position. It is found that the angle between connections from (0, 0) in the reciprocal space to one center of these triangles and to the corresponding spot of gold lattice is 30°, and the length ratio between them is 1.8, both close to the value being expected for the $\sqrt{3}$ position. As mentioned above, this implies that the compression of the adlayer is hexagonally isotropic, whereas the orientation of the adlayer is rotated by a few degrees from the commensurate R30° direction. Furthermore, this kind of hexagonally rotated structure was found to coexist with the $(p \times \sqrt{3})$ structure on the same sample. This coexistence is suggestive of a first-order transition from the striped

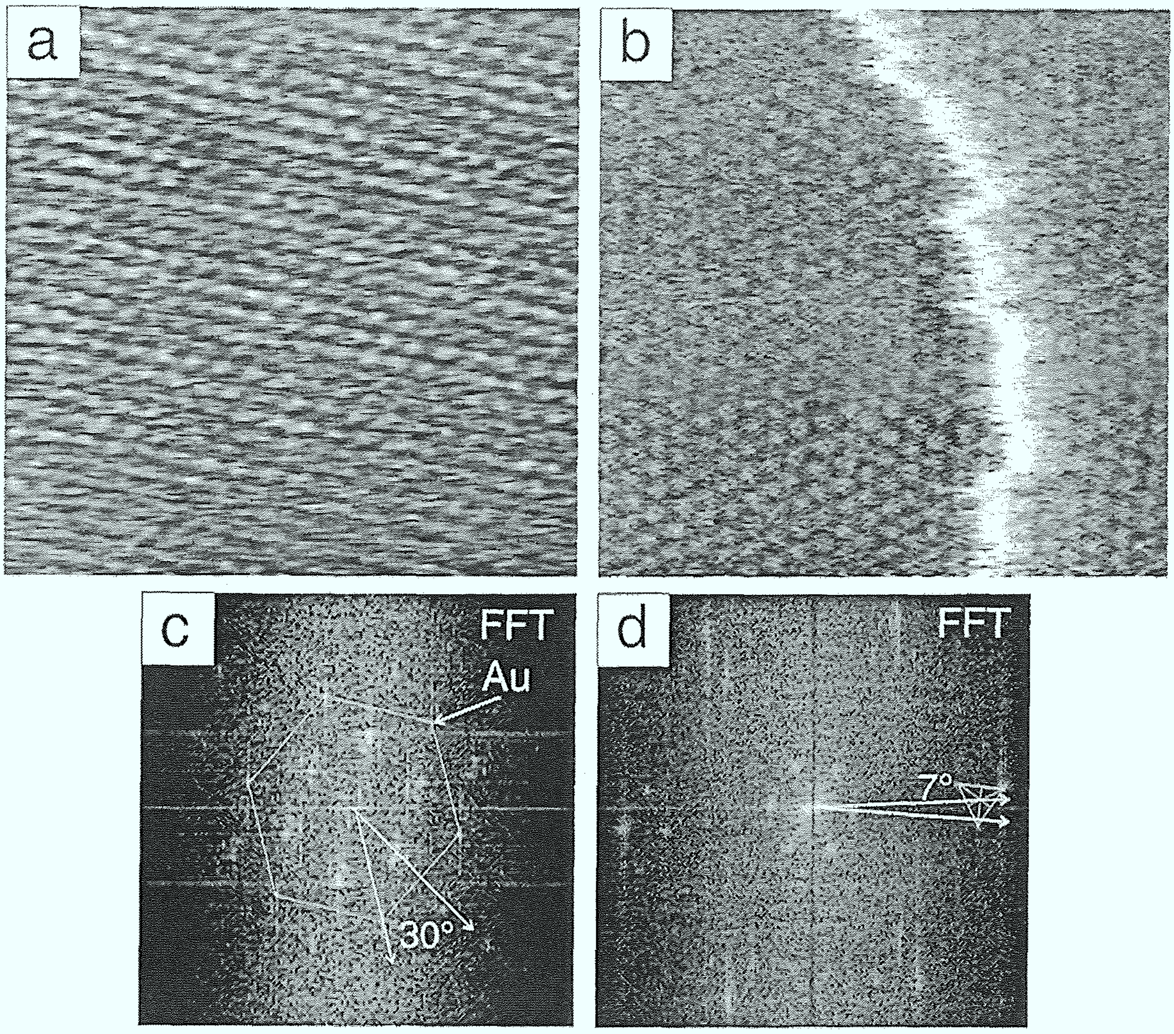

Figure 4.5: (a) Intermediate structure composed of moiré-type and $(p \times \sqrt{3})$ patches (100 × 100 Å). Tunneling parameters: V_t=260 mV, I_t=10 nA. (b) Moiré-type structure across a 'frizzy step' (52 × 52 Å). Tunneling parameters: V_t=10 mV, I_t=8.3 nA. (c) Fourier transform image of (a). (d) Fourier transform image of (b).

$(p \times \sqrt{3})$ to this rotated hexagonal incommensurate phase.

Fig. 4.5b depicts the moiré pattern near saturation coverage on two adjacent terraces separated by a "frizzy" monatomic step. The local distortions in this image clearly evidence the incommensurate nature of the adlayer structure. A quantitative analysis reveals that the superlattice has a periodicity of ~ 21 Å and is rotated about 7° from the R30° direction. It is well known that the periodicity and orientation of moiré patterns are extremely sensitive to the local misfit, and the relative orientation of the adlayer and substrate lattices [73]. Therefore, small distortions and local heterogeneities will result in a significant change of the local orientation of the pattern.

To determine the registry of the iodine lattice with the substrate more accurately, Gao and Weaver used the method of changing potential in the midway of the scan in

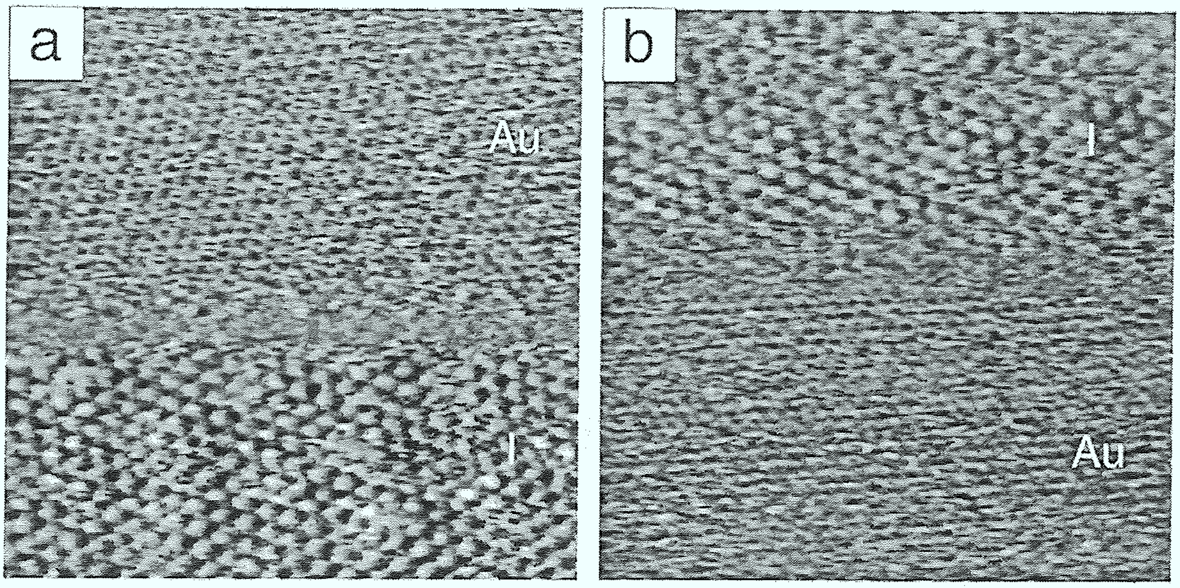

Figure 4.6: "Composite images" revealing the registry between the iodine adlayer and gold substrate (100×100 Å). (a) Tunneling parameters: V_t=10 mV, I_t=25 to 2.1 nA (R_t=0.4 to 4.8 MΩ). (b) Tunneling parameters: V_t=10 mV, I_t=2.1 to 27.3 nA (R_t=4.8 to 0.37 MΩ).

the electrolyte to obtain "composite" images [57], which show the iodine adlayer and Au(111) substrate in the same image. We have adopted this idea in our experiment. Instead of changing the potential, the tunneling impedance R_t was changed roughly midway during the STM scan, which enabled us to obtain similar "composite" images through the selective imaging effect. The results are presented in Fig. 4.6. The image shown in Fig. 4.6a was recorded with a tunneling voltage of 10 mV, the current used for the top half and bottom half is 25 nA (R_t=0.4 MΩ) and 2.1 nA (R_t=4.8 MΩ), respectively. In this way, the registry between the iodine adlayer and substrate can be accurately determined. The angle between the adlattice and gold substrate is 24°, the NNS of the adlayer structure is 4.3±0.1 Å. Immediately after the acquisition of Fig. 4.6a, the image in Fig. 4.6b was recorded using the same switching of the gap impedance but in the reverse direction, i.e. from 4.8 MΩ back to 0.37 MΩ. The iodine structure in the top half image is identical to the one observed in Fig. 4.6a. This observation demonstrates that the process is reversible, i.e. the iodine adlayer seems to be not permanently affected by the stronger interactions between tip and sample at the low gap impedance.

The complete understanding of the selective imaging requires a calculation of the tip-sample interactions and the bonding strength between I–I and I–Au atoms, as well as further experiments. At present, we can only speculate about the possible mechanisms: (i) An electronic state effect can be excluded because the phenomenon is observed by either changing the bias voltage or the tunneling current, i.e. simply determined by the reduction of the distance (impedance) between tip and surface. (ii) From a theoretical study on the energy dissipation in STM [74], it was inferred that the tunneling processes may induce a rise in surface temperature by as much as 30 K at R_t=10^5 Ω and V_t=1 V on metal surfaces. In our case, the tunneling impedance is of the order of 10^5 Ω, but the voltage used is much smaller than 1 V. The investigation of thermal annealing of the iodine monolayer [55] indicates that the desorption of the iodine from Au(111) starts at about 480 K. Therefore, it is unlikely that the heat transfer associated with the tunneling process could account for the observed phenomenon. (iii) The reduction of the tip-sample distance leads to an increase of the tip-sample interaction, which in some cases will modify the sample surface [75]. In fact, the 'critical' gap impedance needed for selective imaging which is of the order of 0.5 MΩ is similar to the threshold impedance required to slide individual atoms on metal surfaces by means of the STM tip [76]. It is therefore conceivable that by strong enough interactions between the tip and the iodine atoms, the latter will be forced to temporarily leave the adsorption sites underneath the scanning tip. Due to the high mobility of the iodine atoms, the adlayer may re-order itself quickly and look as if it was unperturbed once the tip has moved away.

4.4 Conclusions

Iodine adlayer structures on Au(111) have been studied by STM under ambient conditions. Three distinct adlayer structures have been obtained using ex-situ coverage control: (i) At low iodine coverage, a commensurate $(\sqrt{3} \times \sqrt{3})$R30° structure is obtained. (ii) In the coverage range between 0.33 and 0.4, uniaxially compressed $(\mathrm{p}\times\sqrt{3})$ structures were observed. The rarely observed domain-wall structure indicates that a rather uniform compression is favored within this phase. The fact that domain walls do not cross each other are consistent with the fact that the phase transition appears to be of second order. (iii) Near iodine monolayer saturation coverage, a hexagonally compressed phase is observed, which is found to be incommensurate with the substrate. The adlayer is more uniformly compressed and slightly rotated with respect to the commensurate phase. The coexistence of the hexagonally compressed phase and $(p \times \sqrt{3})$ structures reveals that the phase transition is of first order. The 'selective imaging' method has been successfully used to determine the adlayer structure parameters. This unique feature of STM may find wide application in the study of other adsorption systems.

Chapter 5

Oxygen induced restructuring of Au(111)

5.1 Introduction

The existence of the $(22 \times \sqrt{3})$ clean surface reconstruction of Au(111) under ambient conditions clearly demonstrates the inertness of gold. In a recent theoretical study, Hammer et al. [77] showed that this inertness is due to a filled antibonding adsorbate-5d state that provides a repulsive interaction between adsorbates and the gold surface, together with a large coupling matrix element, which is related to the degree of orbital overlap with the adsorbate. Due to this inertness, the chemisorption of gases like H_2, O_2 on the gold surface is found to be a highly activated process. This is also verified in experiments. The interaction of gold surfaces with oxygen has been the subject of many investigations since the early stage of surface science. Controversial results were reported by different groups: in some studies the chemisorption of oxygen on gold surfaces has been observed [78, 79, 80, 81], in several other studies the formation of such surface "gold oxides" has been attributed to the presence of contaminants such as calcium [79, 82] or silicon [83, 84] at the surface. However, some conclusions that can be drawn from these studies are: the chemisorption of oxygen from the gas phase on gold surfaces requires elevated temperature (activated process), and high oxygen pressure; the presence of impurities plays an important role and can promote the oxidation process. This result is in accordance with the observations obtained in this work.

The general rate equation for an activated adsorption process can be expressed as follows [85]:

$$R_a = \frac{\sigma p}{\sqrt{2\pi mkT}} f(\theta) \exp\left(\frac{-E_a}{RT}\right) \tag{5.1}$$

The exponential term indicates the fact that to be adsorbed the particle (e.g. oxygen molecule) must overcome an activation barrier E_a. $p/\sqrt{2\pi mkT}$ is the number of collisions for pressure p, and m and k are the mass of the molecule and the Boltzmann constant, respectively. $f(\theta)$ is a factor which takes account of the fraction of surface not covered by the adsorbed species. Finally, σ is a factor ≤ 1 which reflects the fact that the molecule may not be adsorbed on a site, even if this is vacant and if the molecule possesses the required activation energy. The influence of pressure and temperature on the rate of process can be understood from this expression. Note, that increasing of pressure will always accelerate the process. On the other hand, the temperature must be high enough to ensure the process to happen, but a too high temperature might lead to the desorption of the particles from the surface.

Experiments were performed on two different types of gold samples: gold thin films on quartz and Au(111) single crystals. The properties of the samples have been described in chapter 2. To study the interactions with oxygen, samples were annealed in a quartz tube inserted in a furnace in an oxygen atmosphere for an extended period of time (1/2–24 h). The oxygen pressure of 1 bar was provided by flowing oxygen through the quartz tube. The oxygen flow was maintained during the whole processing at high temperature and also during the sample cooling. Many different sample preparations at various temperatures ranging between 500 and 800°C were carried out. Also, the influence of water vapor on the oxygen chemisorption on the Au(111) surface has been investigated. To this end, oxygen was flowed through a water reservoir containing distilled water before entering the furnace. The present study has focused on the following issues: (i) to provide evidence for the chemisorption of oxygen from gas phase on the Au(111) surface; (ii) to characterize the structural changes at the surface induced by the presence of oxygen atoms and (iii) to gain some insight on the kinetics of the oxygen chemisorption and the concomitant restructuring of the Au(111) surface.

5.2 Oxygen induced hexagonal reconstruction

5.2.1 Structure characterization

After keeping the gold thin film samples for half an hour at 800°C in oxygen, the STM analysis always showed a structural change of the surface when comparing to that of the flame annealed surface. Large facets were often observed with sizes comparable to the maximum scan width of 6000 Å. Fig. 5.1 presents the typical surface structure of the annealed samples at two different length scales. The presence of triangular terraces (Fig. 5.1a) on these facets with a characteristic angle of 60° between adjacent steps shows that these gold facets are (111)-oriented. The appearance of large (111) facets after extensive annealing of gold in oxygen is consistent with earlier observations [86]. Surprisingly, instead of the $(22 \times \sqrt{3})$ reconstruction, a *hexagonal* periodic long-range height modulation is observed on the terraces. This superstructure extends over complete facets and can be observed over distances larger than 6000 Å. The measured periodicity of the hexagonal superlattice is $\sim$ 80 Å. The corrugation associated with this superstructure was measured to be about 0.5 Å. This particular surface structure specifically induced by annealing in oxygen strongly resembles the long-range surface structure observed on Ag(111) induced by oxygen chemisorption after a similar surface treatment [87]. In particular, the periodicity and the corrugation amplitudes of the superstructure are comparable: on the Ag(111) surface the corrugation amplitude and the periodicity were found to be about 1 Å and 72 Å, respectively. A long-range structure was also observed by Wilkins et al. on Au(111) surfaces after flame annealing [88]. Although with a similar periodicity as the superstructure found here, the corrugation amplitude was reported to be of the order of 10 Å.

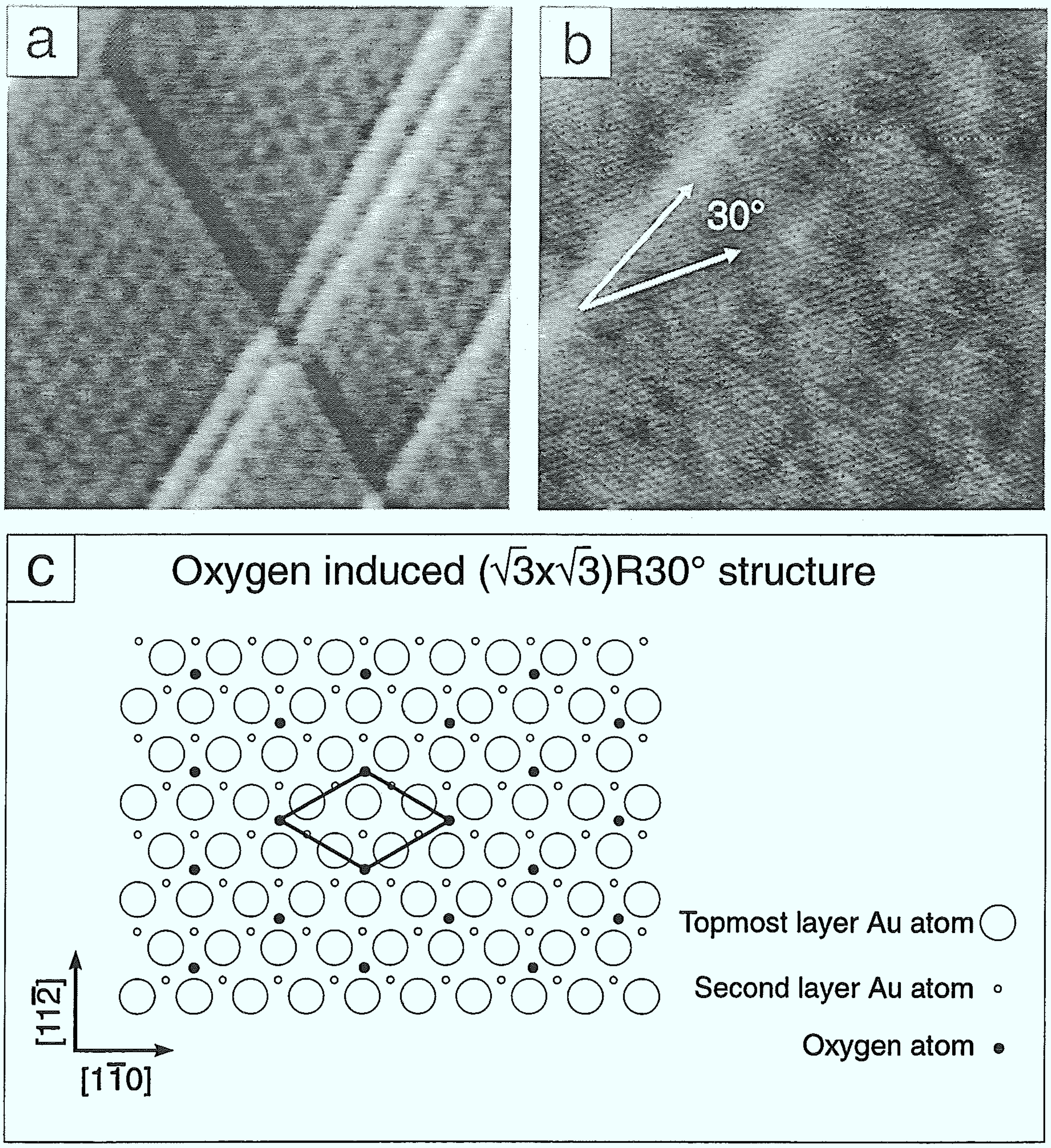

Figure 5.1: STM topographs of the Au(111) surface after annealing of a gold thin film sample in oxygen (1/2 h at 800°C, p_{O_2}=1 bar). (a) Hexagonal superstructure at large scale (1200 × 1200 Å). Tunneling parameters: V_t=400 mV, I_t=5.4 nA. (b) Atomic structures of this surface reconstruction (340 × 340 Å). Tunneling parameters: V_t=400 mV, I_t=2.0 nA. (c) Proposed hard sphere model for the oxygen induced $(\sqrt{3}\times\sqrt{3})$R30° surface structure. It is unclear whether oxygen atoms are adsorbed on fcc or hcp sites.

Fig. 5.1b shows the surface structure at the atomic scale. The hexagonal lattice observed in further zoom-in images has a periodicity of about 5 Å. This value is very close to the $\sqrt{3}a_{\mathrm{Au}}$ where $a_{\mathrm{Au}} = 2.884$ Å is the distance between neighboring atoms on the Au(111) surface. The relative orientation of this structure with the underlying gold lattice can be determined with the reference of the Au surface steps also present in this image. As indicated by the white angle, the atomic structure makes an angle of about 30° with the steps. Since the steps on the Au(111) surface are known to run along the closed packed $[1\bar{1}0]$ directions, the hexagonal surface lattice appears to be rotated by 30° with respect to the gold lattice. Together with the measured surface lattice parameter of 5 Å, this provides strong evidence for the formation of a $(\sqrt{3} \times \sqrt{3})$R30° surface atomic structure upon annealing in oxygen. Fig. 5.1c shows a proposed hard sphere model with oxygen atoms placed in the high symmetry hollow sites. This observation in direct space is quite consistent with the $(\sqrt{3} \times \sqrt{3})$R30° structure observed by reflection high energy electron diffraction (RHEED) on the Ag(111) surface annealed in an oxygen atmosphere [87] and by LEED on a Au(111) single crystal surface after exposure to oxygen at high temperature [80]. In the following, the long-range modulation with periodicities of 60-80 Å will be called superstructure, while the $(\sqrt{3} \times \sqrt{3})$R30° structure will be simply called $\sqrt{3}$ structure.

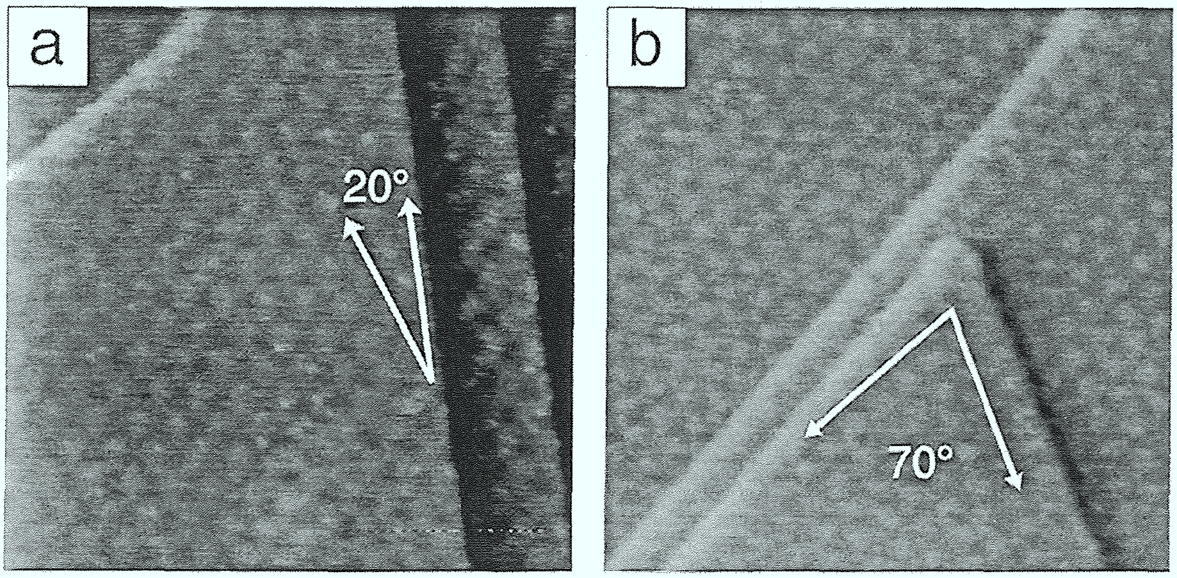

Figure 5.2: STM topographs of the Au(111) surface after annealing of gold thin film samples in oxygen (1/2 h at 800°C, p_{O_2}=1 bar). (a) The hexagonal superstructure with a angle of about 20° to the steps (1200 × 1200 Å, V_t=400 mV, I_t=1.0 nA). (b) The superstructure is distorted from a normal hexagonal lattice (1360 × 1360 Å, V_t=400 mV, I_t=1.1 nA).

There are many examples in surface science that the adsorption of atoms and molecules causes a restructuring of single crystal surfaces, ranging from small atomic relaxation and reconstructions to macroscopic shape modifications. Some possible mechanisms of this adsorbate-induced restructuring were discussed, e.g. , in a review article [89]. Based on the STM measurements, the origin of the long-range hexagonal superstructure on the Au(111) surface has been uncovered. The results presented below reveal that it can be understood in terms of lattice distortions induced by the adsorbate-substrate interactions.

A quantitative examination on the STM images shown in Fig. 5.1a and Figs. 5.2a, b reveal that the superstructure is not a well defined hexagonal lattice with a large but unique unit cells. The straight atomic steps and the well defined 60° angles between them can serve as a reference for evaluating the regularity of the pattern. Comparing Figs. 5.1a and 5.2a, it is obvious that the rows formed by the superstructure (i.e. , the lines connecting neighboring bright or dark spots along the high symmetry directions) do not have a fixed crystallographic orientation. Indeed, in Fig. 5.1a the rows are almost parallel to the surface steps, whereas in Fig. 5.2a an angle of about 20° is measured between these rows and the step edge. Furthermore, the pattern itself can be significantly distorted: (i) the rows of the superstructure are not exactly straight but can meander on length scales much larger than the periodicity. (ii) the overall symmetry is not truly hexagonal. For instance, the left step edge on the terrace in the lower part of Fig. 5.2b makes an angle of about 10° with respect to the rows of the superstructure, whereas the pattern is almost parallel to the right step edge. Hence, the angle between the two corresponding symmetry directions of the superstructure is about 70° (instead of 60° as expected for a perfectly hexagonal pattern). On the other hand, the atomic structure is *undistorted* hexagonal and always measured to make an angle of 30° with respect to the surface steps, independent of the overall shape or orientation of the superstructure (see Fig. 5.1b). (iii) even the periodicity D of the superstructure is found not constant, but can vary between 30 Å and 60 Å. In some rare cases, the coexistence of superstructures with different periodicity could even be observed in the same surface region [73]. This indicates that the superstructure is extremely sensitive to local inhomogeneities on the surface. The above experimental observations are characteristic of the geometrical properties of moiré patterns which have often been invoked to explain the long-range modulations in the surface structures induced by lattice distortions due to the presence of adsorbates [90, 91, 92]. Bao et al. [87] have also used this geometrical analysis to interpret the superstructure observed on the Ag(111) surface after exposure to oxygen.

5.2.2 Moiré pattern analysis

The moiré patterns considered here are modulation patterns resulting from the superposition of two atomic layers with the same symmetry but different lattice parameters a versus $\tilde{a}$ and different orientation. The periodicity D and the rotation angle Φ of the moiré pattern can be expressed as a function of the lattice mismatch $m \equiv (\tilde{a} - a)/a$ and the rotation angle θ between the two lattices in the following way [73]:

$$D = \frac{(1+m)a}{\sqrt{(1+m-\cos\theta)^2 + \sin^2\theta}} \tag{5.2}$$

$$\tan\Phi = \frac{\sin\theta}{1+m-\cos\theta} \tag{5.3}$$

These expressions, which are illustrated in Fig. 5.3, allow a quantitative analysis of the moiré pattern. Since the periodicity D is a monotonically decreasing function of

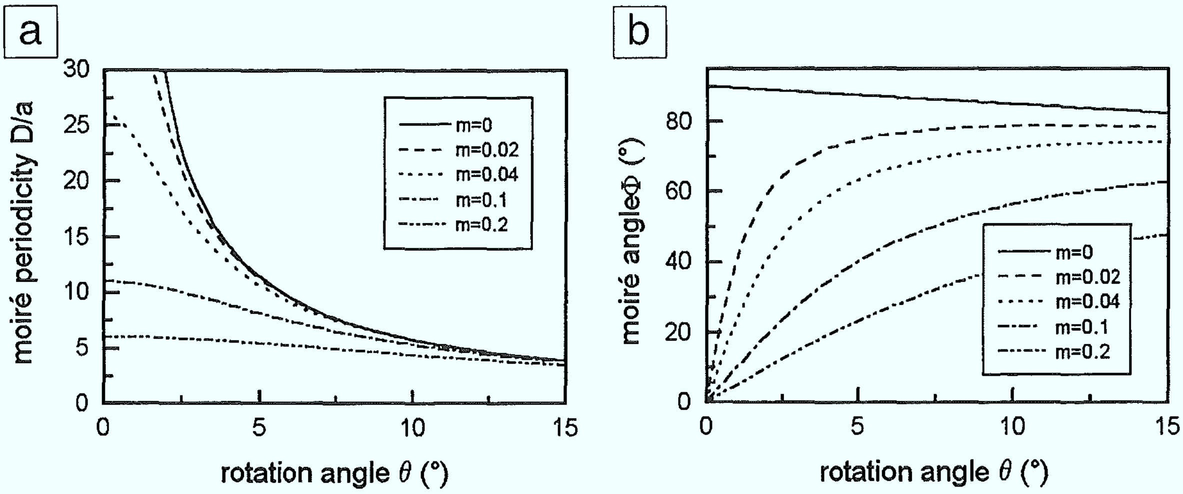

Figure 5.3: Variation of the moiré periodicity D (a) and moiré angle Φ (b) as a function of the rotation angle θ between the two superimposed lattices for various values of the lattice mismatch m.

the rotation angle θ, with its maximum value $(1 + 1/m)a$ for $\theta = 0$, a periodicity of 60 Å or larger can only be achieved if the lattice misfit between the topmost two layers is smaller than 5%. Note, however, that the sign of the misfit (i.e., whether the topmost layer is compressed or expanded) cannot be determined from the size of the moiré periodicity D alone. It can be seen that for a lattice misfit below 5%, a small misorientation θ of the order of 1° results in a rotation of the moiré pattern Φ by more than 20°. More precisely, a misfit m=4% together with a rotation between the two lattices of $\theta = 1°$ results in a (clockwise) rotation $\Phi = 23.5°$ of the moiré pattern (Fig. 5.3b). At the same time, the periodicity D is also slightly changed: the period of the rotated moiré is about 10% smaller than when the two lattices were aligned (Fig. 5.3a). Likewise, a variation of the misfit by about 1% can lead to a change of the moiré angle Φ by more than 10°, if θ is small ($\theta \leq 1°$) but non zero (see Fig. 5.3b). The behavior of the long-range superstructure observed on the Au(111) surface can be understood from the above analysis of the moiré patterns. Also, the extreme sensitivity of the moiré pattern to the local distortions of the surface lattice can be used to probe the local inhomogeneities of this kind of reconstructed surfaces.

From the above results we can derive the following tentative structural model: the oxygen atoms are strongly bound in the near-surface region, most likely to the topmost Au(111) atomic layer. From the R30° orientation, the lattice spacing of about 5 Å, and the absence of any spatial variation of the STM image contrast for this local structure (as it would arise if different adsorption sites were populated), we infer that the oxygen atoms are correlated to the topmost layer by a commensurate $(\sqrt{3}\times\sqrt{3})$R30° structure. On the other hand, a long-range height-modulation is observed which arises from a lattice mismatch and maybe a slight rotation of the topmost Au layer (together with the oxygen layer attached to it) with respect to the second and deeper layers of the bulk Au(111). This gives rise to the moiré-type pattern discussed above. Although the resulting change in the atomic density of the first layer with respect to the second layer cannot be directly deduced from the moiré pattern analysis, the nucleation of the long-range hexagonal reconstruction at steps and the observed 'spill over' of material onto the lower terrace (see Fig. 5.4a below) indicates that the density of the atoms in the topmost layer for the hexagonal reconstruction is *reduced* with respect to the bulk density.

5.2.3 Kinetics of the formation of the oxygen induced surface restructuring

As mentioned above, previous studies showed that impurities could facilitate the reaction of oxygen with the Au(111) surface in a strong way. Also, based on theoretical arguments, Besenbacher and Nørskov [93] have described how impurities on surfaces of transition metals might act as centers for the nucleation of oxide islands and thereby enhance the effective interaction of oxygen with the surface. Different kind of impurities may appear on the surface of our thin gold film samples, namely Cr, Si and Ca, which may diffuse from the Cr coated quartz substrate during annealing in oxygen. In fact, after annealing the gold thin film samples the presence of chromium at the surface was detected by Auger spectroscopy. Therefore, it is reasonable to speculate that these impurities are involved to some extent in the chemisorption process. In order to check this, experiments on Au(111) single crystals of high purity were performed using the same preparation procedure described above. Both the $\sqrt{3}$ structure and the superstructure were observed on the single crystal surfaces, too. Moreover, measurements on the single crystals also provide further evidence that the surface restructuring proceeds via a nucleation and growth mechanisms. The impurities can at least influence the nucleation of the superstructure, but they appear to be not responsible for the formation of the final extended structure.

Fig. 5.4a depicts the characteristic surface morphology of Au(111) obtained after annealing the gold single crystal in oxygen at $T = 800°\text{C}$ for 3 hours. An area of about 700 Å in diameter located on the upper terrace and close to a monatomic step edge exhibits the characteristic long-range superstructure with hexagonal symmetry. The boundaries of the restructured area form straight lines at 120° angles and the step edge protrudes outwards onto the lower terrace (probably as a result of the restructuring). Furthermore, the surface of the region exhibiting the hexagonal superstructure appears to be slightly lowered in the STM image with respect to the surrounding upper terrace. However, a conclusion on the topography cannot be drawn from this result: the observed lowering of the surface height could likely be due to a different electronic structure of the two regions. In fact, under usual tunneling conditions, oxygen atoms chemisorbed on various metal surfaces such Al, Cu, Ni and Pt are imaged as *depressions* rather than *protrusions* [93].

Many experiments using various combinations of annealing temperature and time have been performed on Au(111) single crystals. In case the annealing temperature is low and/or the time is short, only locally restructured areas were observed, which were usually nucleated around structural imperfections like steps or screw dislocations as illustrated in Fig. 5.4a. Only after long-time annealing (over 24 h) at $T = 800°\text{C}$ in an oxygen atmosphere saturated with water (the presence of water is believed to accelerate the chemisorption process [87]), the restructuring of the Au(111) surface can

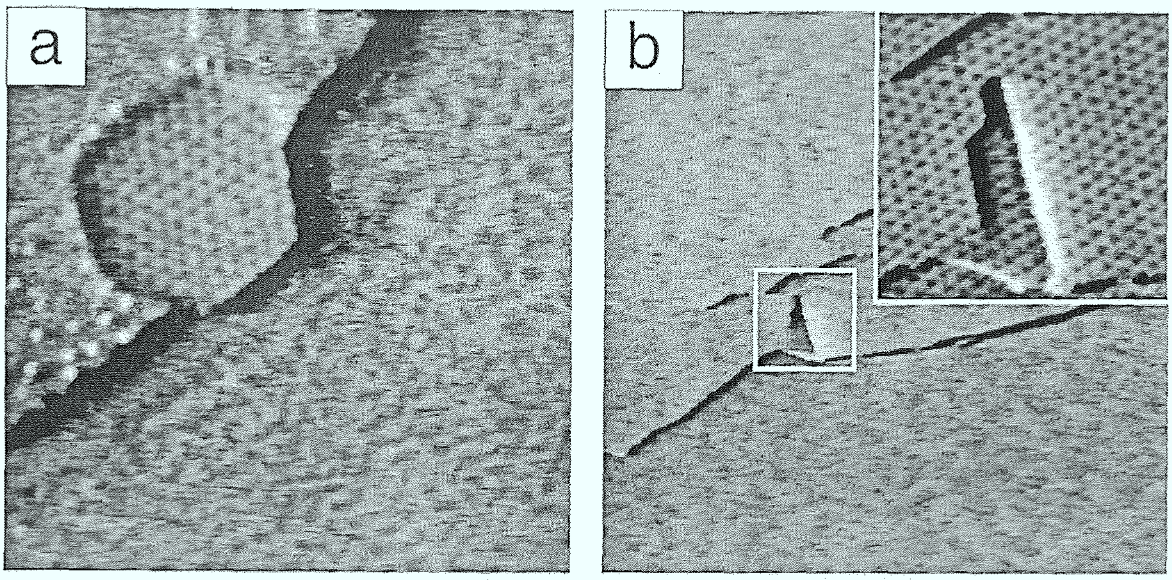

Figure 5.4: (a) STM topograph (1850 × 1850 Å) of the Au(111) single crystal surface after annealing in oxygen at 800°C, p_{O_2}=1 bar, for 3 h. An area exhibiting a long-range superstructure with hexagonal symmetry is located on the upper terrace close to a monatomic step edge (V_t=120 mV, I_t=2.0 nA). (b) STM topographs of the Au(111) single crystal surface after annealing in a water saturated oxygen atmosphere at 800°C, p_{O_2}=1 bar, for 24 h. The main image (6100 × 6100 Å) only shows a small part of a completely reconstructed area which extends over a length of several microns. The central region indicated by the white square was scanned at higher magnification and is shown in the inset in the top right corner. It reveals the details of the hexagonal superstructure with a periodicity of about 65 Å (V_t=200 mV, I_t=5.0 nA).

become almost complete. Fig. 5.4b shows images obtained after such a preparation (T = 800°C for 24 h). The entire region in the large scale image exhibits a very regular hexagonal superstructure with a period of 65 Å, as can be seen from the zoom-in image shown in the inset. In fact, surface regions over length scales of several microns have been found to be completely reconstructed. This situation is again very similar to the O/Ag(111) case, in which the Ag(111) crystals had to be annealed in oxygen for as long as 48 hours for a complete restructuring.

The time scales governing adsorbate induced restructuring process have been discussed by Somorjai and Van Hove [89]. They suggest that these time scales can vary widely, ranging from an atomic vibration period to beyond the human lifetime. There are two main steps in the restructuring process: the first one is the adsorption itself, in the case of an activated process, the time scale is determined by the activation energy; secondly, the restructuring itself takes time, for a complex reconstruction, there may exist an activation barrier for the structural phase transitions. It seems evident that both these steps are involved in the oxygen induced surface restructuring of Au(111) as well as Ag(111). In this context, the long annealing time needed for the complete restructuring is not unreasonable. On the other hand, the observation of the local reconstructed islands, sometimes coexisting with the herringbone reconstruction, suggests that the formation of the long-range hexagonal reconstruction and the necessary atomic rearrangements within the gold surface proceeds via nucleation and subsequent growth of such restructured areas during chemisorption of oxygen at high temperature. In such a *heterogeneous* process, the number of the nucleation centers plays a crucial role.

The difference observed between the behavior of the gold thin films and gold single crystals is particularly noteworthy. In the case of gold thin films deposited on quartz, large (111) facets are obtained after annealing in oxygen for a relatively short period of time, typically 1/2 hour. The facets can grow much larger than 1000 Å and are always completely reconstructed. The lateral extension of the superstructure is only limited by the size of the facet. As mentioned above, the gold films were evaporated on a thin chromium layer deposited on quartz substrates containing silicon and calcium. At least silicon and calcium have been claimed to trigger the chemisorption of oxygen on gold surfaces [82, 83]. A similar observation was reported by Bonzel et al. for the 'oxide formation' on Pt(111) [94]. In this case, the appearance of the 'Pt oxide' was always correlated with the presence of oxide forming impurities (mainly Si) segregating to the surface during oxygen exposures at high temperature. The enhanced concentration of impurities in the gold films could explain why the restructuring is more easily obtained on these samples than on the Au(111) single crystals. However, during annealing of the gold films, grain coarsening, nucleation of facets, and chemisorption of oxygen all take place at the same time. Therefore, the formation of the reconstruction on the gold films might as well be correlated with the appearance of large (111) facets, for instance, due to a more efficient chemisorption of oxygen at the edge of the growing terraces. The complexity of each of the above processes prevents a definite analysis of the formation of the oxygen induced reconstruction in the case of the gold films.

5.3 Modified herringbone reconstruction

The important role of surface defects or impurities on the nucleation of the oxygen induced restructuring is also evident from the experiments on Au(111) single crystals. It has been found that the nucleation of the hexagonal superstructure depends not only on the actual single sample preparation but on the entire sample thermal history. After repeated cycles of annealing in oxygen, the average terrace width of the Au(111) sample became larger and larger: in some cases atomically flat terraces extending over areas larger than 6000 × 6000 Å were observed (see the STM topograph presented in Fig. 5.5a). On these large terraces, the nucleation of the hexagonal superstructure was extremely rare. The characteristic hexagonal pattern was found only at very few places, whereas most terraces exhibited a "modified" herringbone structure shown in Fig. 5.5 and Fig. 5.6.

While the STM images in Fig. 5.5 and Fig. 5.6a depict this structure on a large scale, the zoom-in image in Fig. 5.6b reveals the underlying atomic structure. The overall morphology is clearly derived from the reconstruction pattern observed on the clean Au(111) surface, but exhibits a locally enhanced contrast. Some of the fcc regions between reconstruction double-lines appear darker than others (see, e.g. , the region

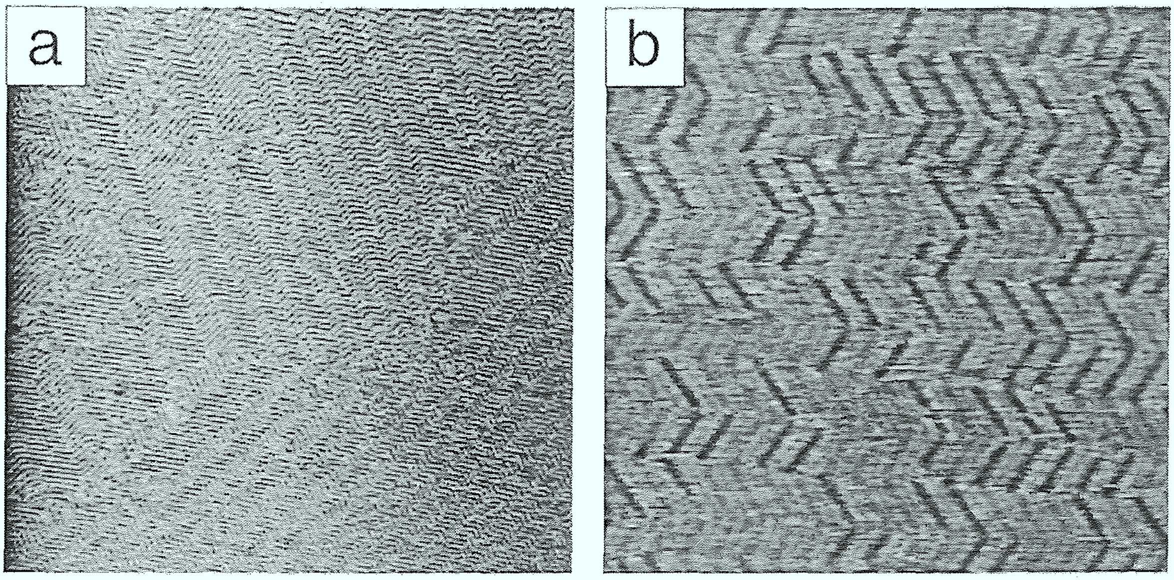

Figure 5.5: STM topographs of the Au(111) single crystal surface after annealing in oxygen at 800°C, p_{O_2}=1 bar, for 5 h. (a) Reconstructed terrace extending over 6000 Å without steps (6000 × 6000 Å, V_t=150 mV, I_t=3.3 nA). (b) Modified herringbone pattern showing local depressions in some fcc regions between the reconstruction double-lines (1520 × 1520 Å, V_t=100 mV, I_t=5.1 nA).

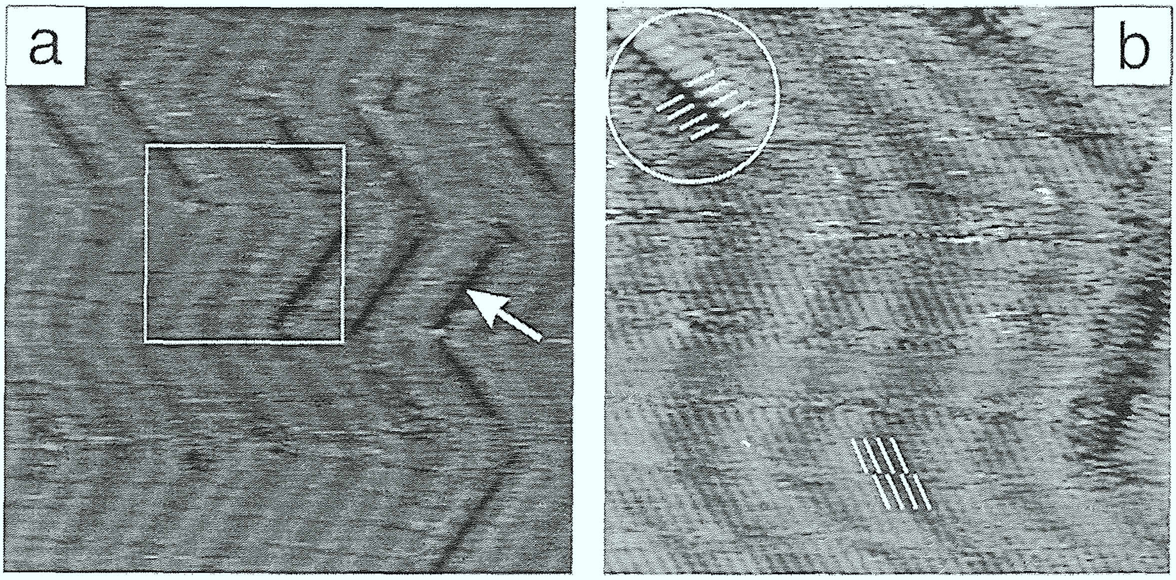

Figure 5.6: (a) STM topograph (630 × 630 Å; V_t=180 mV, I_t=4.0 nA) of the modified herringbone pattern recorded from the Au(111) surface after annealing in a water saturated oxygen atmosphere (700°C, p_{O_2}=1 bar, for 1 h). (b) Zoom-in (220 × 220 Å; V_t=180 mV, I_t=4.0 nA) of the central region indicated by the white square in (a), revealing the details of this structure at the atomic scale.

indicated by the white arrow in Fig. 5.6a). The central area of Fig. 5.6a (marked by the white square) was scanned at higher magnification and is shown in Fig. 5.6b. In this image, a periodic pattern of row-like features can be distinguished. These 'rows' run along the close-packed $[1\bar{1}0]$ directions of the Au(111) surface, forming an angle of about 30° to the zigzag reconstruction lines in the central area of the image and being perpendicular to the reconstruction lines in the upper left and bottom right corners. Examinations of this structure from a number of such images reveals that: (i) the rows are separated by a distance of about 5 Å$= \sqrt{3}a_{Au}$ and (ii) the origin of the enhanced imaging contrast (i.e. the local depressions) may be associated with domains of rows with a different orientation. As illustrated by the white circle in Fig. 5.6b, a comb-like pattern, as a results of an anti-phase boundary, leads to the appearance of a dark central trough in the minority domains. Similar anti-phase boundaries are also observed with the majority domains (white lines in the lower part of Fig. 5.6b). However, compared to those in the minority domains, the effect on the image contrast is much less pronounced and the position of these boundaries can change from one scan to the next. In analogy to the oxygen induced structure discussed above, we may attribute the rows with $\sqrt{3}$ periodicity to atomic oxygen adsorbed at the Au(111) surface. In addition to the row-structure, we find that, on average, the separation between neighboring pairs of reconstruction lines is slightly increased from 65 Å (corresponding to a $(22 \times \sqrt{3})$ structure) on the clean surface to about 75 Å (corresponding to a $(26 \times \sqrt{3})$ structure) in the modified herringbone reconstruction. Previous studies [95, 96] have shown that the Au(111) reconstruction is very sensitive to the presence of adsorbates. Furthermore, the observation of unusual reconstruction patterns in electrolyte was reported [37]. It is reasonable to think that in the present case the modification of the reconstruction is also due to the presence of an adsorbate, namely, atomic oxygen. It was found that the row-structure deteriorates more easily during imaging and is less stable in ambient conditions than the hexagonal structure. This might indicate that the oxygen is more weakly bound to the surface in the modified herringbone structure than in the hexagonal reconstructed phase.

To further discriminate between the two structures, the dependence of the STM image contrast on the tunneling parameters has been investigated, the results are presented in Fig. 5.7. Fig. 5.7a shows an image of the *hexagonal reconstructed* phase, recorded using usual tunneling condition: V_t=160 mV and I_t=2.0 nA, corresponding to a gap impedance R_t=80 MΩ. Then the gap impedance was lowered to R_t=0.83 MΩ and Fig. 5.7b was recorded. It can be seen that the long-range superstructure is almost not discernible. However, after readjusting the tunneling parameters to a higher gap impedance: R_t=117 MΩ, the hexagonal superstructure could be imaged again without any significant deterioration (Fig. 5.7c). The result of this experiment confirms that the oxygen induced hexagonal reconstruction is very stable, and cannot be destroyed even by strong tip-sample interactions. Thus, the oxygen appears to be tightly bound at the Au(111) surface.

The results of a similar experiment performed on the *modified herringbone* structure are presented in Figs. 5.7d-f. The gap impedances used in recording the three images were: R_t=33.4 MΩ, R_t=0.4 MΩ and R_t=22.4 MΩ, respectively. The difference between the two topographs, Fig. 5.7d and 5.7e, is evident: whereas in Fig. 5.7d the additional

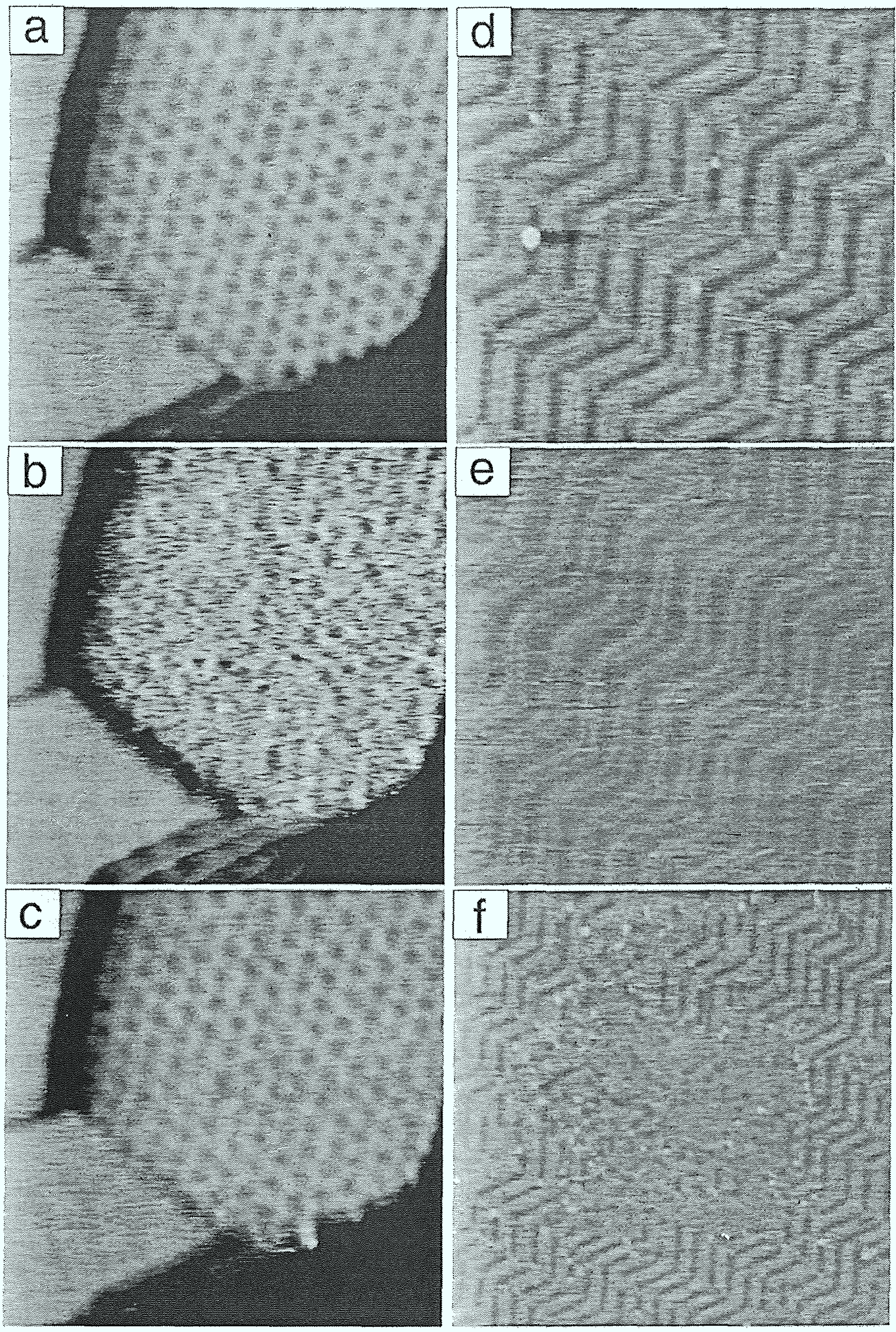

Figure 5.7: (a), (b), (c): STM topographs (900 × 900 Å) of the Au(111) surface after annealing in a water saturated oxygen atmosphere (800°C at p_{O_2}=1 bar for 24 h). The images were recorded using the following tunneling parameters: (a) V_t=160 mV, I_t=2.0 nA; (b) V_t=6.6 mV, I_t=8.0 nA; (c) V_t=164 mV, I_t=2.0 nA. (d), (e), (f): STM topographs of the Au(111) surface after annealing in a water saturated oxygen atmosphere (750°C at p_{O_2}=1 bar for 24 h). The images were recorded using the following tunneling parameters and scan size: (d) V_t=167 mV, I_t=5.0 nA (900 × 900 Å); (e) V_t=2.0 mV, I_t=5.0 nA (900 × 900 Å); (f) V_t=112 mV, I_t=5.0 nA (1800 × 1800 Å).

depressions in most of the fcc-regions between reconstruction lines are clearly resolved, Fig. 5.7e only shows the bare Au(111) herringbone reconstruction pattern. In contrast to the experiment on the hexagonal structure, this process is *irreversible*, i.e. the surface topography is permanently modified by the strong tip-sample interaction at small tunneling gap resistance. This becomes evident in the 'zoom-out' STM image in Fig. 5.7f, recorded immediately after acquisition of Fig. 5.7e. Indeed, a square area is seen in the center of the image, in which the enhanced contrast of the modified herringbone pattern can no longer be observed — in contrast to the surrounding area. However, we have observed a (low-contrast) pattern in the central area similar to the one shown in Fig. 5.7e, when lowering the gap impedance again. A possible explanation for this observation could be that the oxygen is bound rather weakly to the surface in the modified herringbone structure. While the oxygen related row-structure (c.f. Fig. 5.6) is destroyed by the scanning tip, the underlying gold surface is still reconstructed. From a large number of similar experiments we conclude that the modified herringbone pattern can be irreversibly destroyed by the scanning tip, if a tunneling gap impedance below 1 MΩ is used for imaging. In contrast, the oxygen induced hexagonal reconstruction pattern was not found to be modified until a mechanical contact between tip and sample occurs.

The surface modification induced by the lowering of the tunneling impedance during scanning has also been found for I/Au(111) and is discussed in detail in chapter 4. The comparison of the results may give some insight on the bond strength between the adsorbates and the Au(111) substrate. Since the hexagonal reconstruction could not be significantly modified, the bonding must be the strongest. Such a strong bonding can further induce the lifting of original $(22 \times \sqrt{3})$ reconstruction of Au(111) and the formation of a new hexagonal structure on the Au(111) surface. The critical tunneling impedance needed for modification in the I/Au(111) and modified herringbone cases are of the same order of magnitude and are comparable to the threshold impedance required to slide individual atoms on metal surfaces using an STM tip [76]. This may be interpreted in such a way that the bond strength between I and Au is comparable to that between O and Au in the modified herringbone structure. However, the iodine adsorption on Au(111) induces a structure transformation from $(22 \times \sqrt{3})$ to (1×1) structure, while there is no large Au(111) restructuring in the modified herringbone phase. This indicates that the bond strength between O and Au in the modified herringbone structure should be even weaker than that between I and Au.

Finally, the experiments show that the modified herringbone reconstruction usually cannot be observed after being exposed to air for more than 12 hours. In contrast, the hexagonal structure is found to exist without significant deterioration even after several weeks of exposure in air. Due to its enhanced stability, the hexagonal reconstruction allows the further investigation by XPS and AES in UHV and by synchrotron X-ray diffraction in air.

5.4 XPS and XRD results

5.4.1 Characterization of the O/Au(111) surface by XPS and AES

Since the presence of impurities strongly affects the nucleation of the oxygen induced structures on Au(111), XPS and Auger experiments were performed to characterize the surface compositions in order to check whether a large amount of impurities is associated with the reconstructed phases. The preliminary results are described in this section. The Au(111) single crystal was first investigated by STM after annealing in a water saturated oxygen atmosphere at 800°C, p_{O_2}=1 bar, for 24 h. To characterize the overall morphology of the sample surface, large scan-size (3000 × 3000Å) STM images were recorded at different places of the sample. The area of the hexagonally reconstructed regions is measured from each image. From about 30 such images, we find that the total area of the hexagonally reconstructed regions is about 1/3 of the whole surface area. After the STM measurements, the gold crystal was transferred into a UHV chamber for the XPS and AES study.

XPS spectra were recorded in the constant pass energy mode with a Mg $K\alpha$ radiation source operating at 400 W. An analyzer pass energy of 100 eV was used which corresponds to a resolution of 1.3 eV.

Fig. 5.8 shows XPS spectra obtained from the surface of Au(111) single crystal mentioned above. Examination of the spectrum presented in Fig. 5.8a finds that: except for the gold peaks, a peak in the position corresponding to the binding energy of oxygen 1s (530 eV) and a rather small peak at 284 eV, most likely due to carbon contamination are observed. The fact that no additional peaks are observed indicates that the concentration of other impurities on this surface must be very low. The exposure of the sample surface to air may be responsible for the presence of the carbon peak. On the other hand, this spectrum was obtained after the crystal had been stored in UHV for several days. During this period of time, it is possible that some organic molecules in vacuum system can accumulate on the surface which may also responsible for the carbon peak observed.

The O 1s XPS spectrum shown in Fig. 5.8b is somewhat noisy. As can be seen that the original spectrum can be well fitted with two Gaussian peaks centered at 528.7 and 530.3 eV, respectively. The value of O 1s binding energy may provide information related to the oxygen compounds formed at the surface. The XPS studies on the surface oxidation of Ag(111) have shown that there are three O 1s states with binding energies of 530.3, 530.4 and 529.0 eV, respectively [87]. The O 1s state with a binding energy of 529.0 is connected with the $(\sqrt{3}\times\sqrt{3})$R30° phase associated with the long-range reconstruction, while the other two were attributed to silver bulk oxide and another type of surface oxide which is not stable above 600 K. The O 1s binding energy of 529 eV is also typical for atomic oxygen forming a close shell O^{2-} ion on the metal surfaces [83]. Previous studies on the surface oxidation of a Au(100) crystal in electrolyte showed that the O 1s binding energy was shifted from 532.4 to 530.8 eV when the potential was increased from 0.8 to 4.0 V [97]. The same authors also reported a O 1s binding

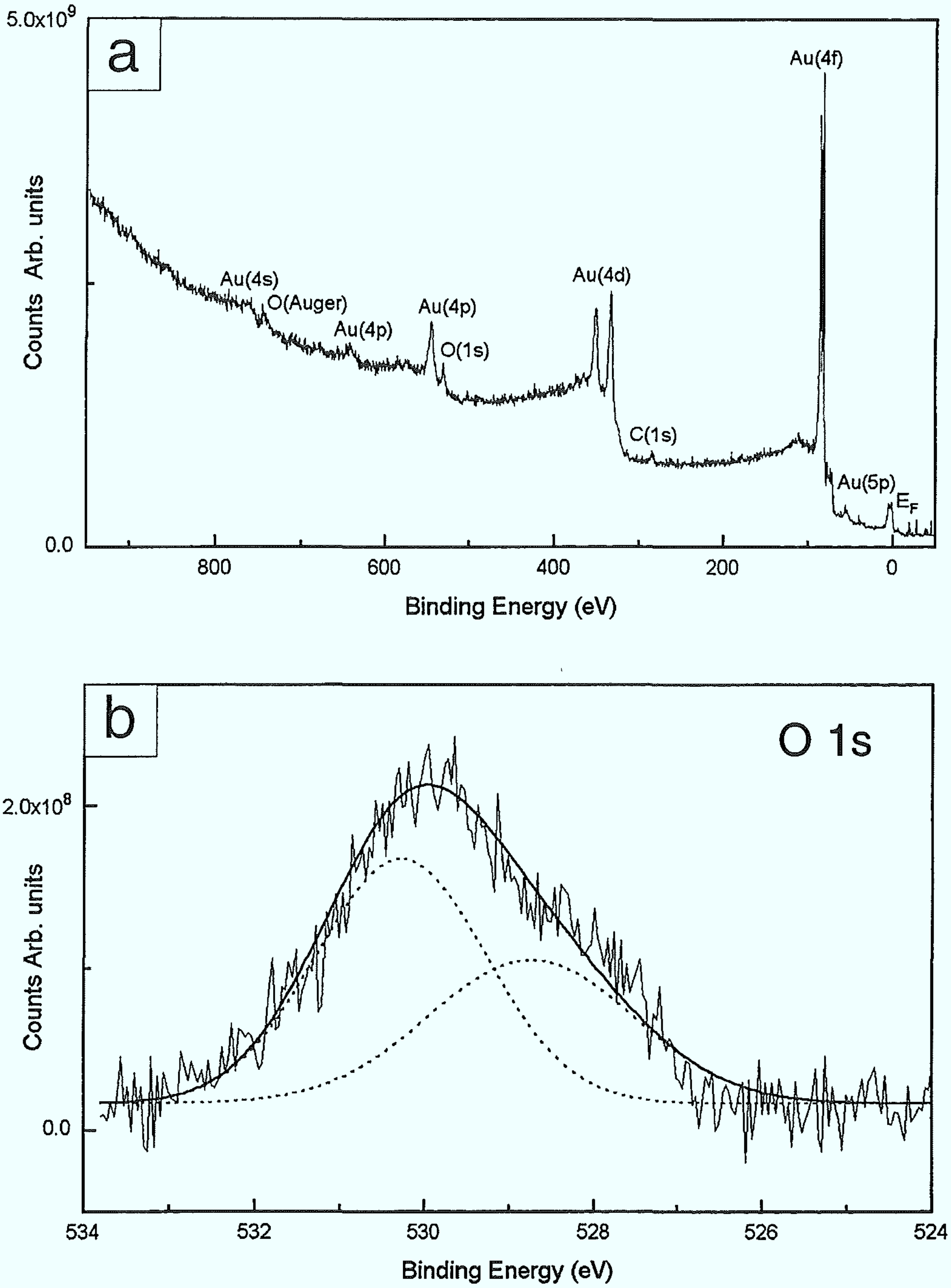

Figure 5.8: (a) XPS spectrum from the hexagonally reconstructed Au(111) single crystal surface. Except for Au, O and a small amount of C, no other elements are discernible. (b) XPS spectrum of the O 1s electronic state fitted by two Gaussian peaks (dotted lines) centered at 528.7 eV and 530.3 eV, respectively. The solid line is the sum of the two Gaussian peaks.

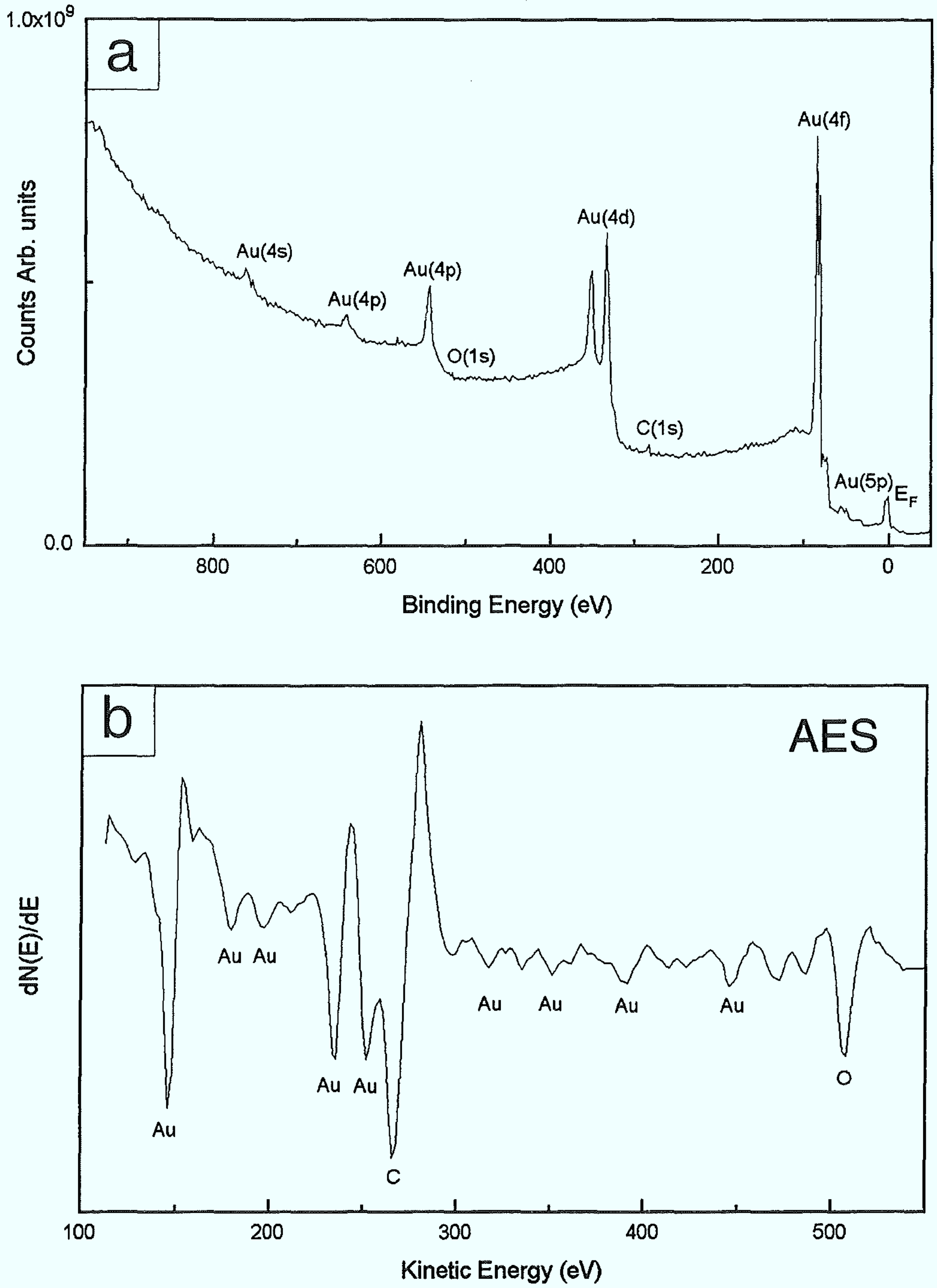

Figure 5.9: (a) XPS spectrum recorded from the Au(111) single crystal surface exhibiting the modified herringbone structure prior to transfer into the UHV-chamber. (b) AES spectrum taken from the same surface showing the presence of oxygen on the surface.

energy of 530.1 eV after annealing the gold crystal in oxygen at 900 K for 18 hours. The O 1s binding energy from reactive sputter deposited auric oxide (Au_2O_3) [98] and a typical UV/ozone oxidized gold surface [99] was found to be 530.1 and 529.61 eV, respectively.

Combining the information from these experiments, it can be concluded that the O 1s state with the binding energy of 528.7 eV is most likely related to the oxygen induced hexagonally reconstructed phase, and the state with the binding energy of 530.3 eV is contributed from the normal Au_2O_3. Note, that no significant change of the oxygen signal after several days exposure to UHV was observed.

A very crude quantitative estimate of the oxygen coverage on this surface from the XPS relative intensities gives a value for the O/Au atom ratio of the order of 0.15-0.20. There are two other factors to be considered here: (i) this surface is only partially ($\sim$ 30%) reconstructed with the hexagonal phase. (ii) the oxygen peak is resolved into two peaks, with the peak area ratio of about 0.7, the peak centered at the binding energy of 528.7 eV related with the hexagonal phase has the smaller area. Taking these factors into account, an O/Au atom ratio in the hexagonal phase is found in the order of 0.2-0.27, which is consistent with the value of 0.33 expected for a $(\sqrt{3} \times \sqrt{3})R30°$ structure.

The XPS studies were also performed on the gold surface exhibiting the modified herringbone reconstruction. The Au(111) crystal was annealed in a water saturated oxygen atmosphere (p_{O_2}=1 bar) at 800°C, for 5 h. The STM analysis on this surface showed the same morphology as the STM images presented in Fig. 5.5. The crystal was then transferred into the same UHV chamber and the XPS measurements were performed using the same parameters as mentioned above. The XPS spectrum shown in Fig. 5.9a was taken from this surface after two days exposure in UHV. Comparing this spectrum with the one in Fig. 5.8a, it is clear that the O 1s signal is almost not discernible. At the same time, there are no large differences between the gold and carbon signals in these two spectra. Since the oxygen signal is too weak, it is impossible to determine the exact binding energy of the O 1s peak. Since the modified herringbone structure is not stable after exposure in air for several hours, it is not unreasonable to think that most of the oxygen atoms may have desorbed from the surface after pumping or exposure to X-ray radiation. However, the Auger analysis (Fig. 5.9b) of this surface observed a peak at the position corresponding to oxygen (509 eV). Previous investigations on the oxidation of Pt(111) by Niehus and Comsa show that the oxygen Auger peak at 510 eV is associated with the chemisorbed oxygen, while the peak at 503 eV is due to the "oxide" or subsurface oxygen atoms [100]. This gives a clue that oxygen atoms in the modified herringbone structure are in a state similar to those chemisorbed on the Pt(111) surface. Furthermore, the Auger analysis showed no trace of other elements except carbon on this surface.

The fact that we were not able to detect Ca or Si impurities in the XPS and Auger spectra obtained from the restructured single crystal samples indicates that the concentration of these impurities must be rather low. Therefore, the appearance of extended, regular patterns of the $(\sqrt{3} \times \sqrt{3})R30°$ phase together with the long-range hexagonal superstructure cannot be attributed to the formation of a stochiometric surface compound involving a large amount of impurities. Instead, the observed structures appear to be intrinsically induced by the chemisorption of oxygen at the Au(111) surface.

5.4.2 XRD study on the oxygen-induced hexagonal reconstruction

The X-ray diffraction (XRD) measurements on the oxygen-induced hexagonal reconstruction on Au(111) were carried out using Beamline D32 (French CRG) at the European Synchrotron Radiation Facility (ESRF) [101]. Monochromatic x rays of energy $E = 10$ keV were selected by a Si(111) crystal. A flux on the order of 10^{11} photons/s in a bandwidth of $\Delta E/E = 2 \cdot 10^{-4}$ is obtained at the sample position with a beam size of 0.3×0.3 mm^2. The experiment was performed using a four-circle goniometer, which can operate in horizontal or vertical geometry for investigations in ambient environment. The accuracy of each movement is 1/1000° for rotations and 1 μm for translations. The detector used is a low background scintillation device. The sample used was a Au(111) single crystal as described in chapter 2. Before the XRD measurements, the crystal was annealed in a water saturated oxygen atmosphere at 800°C for 24 hours. The STM analysis showed that large hexagonally reconstructed domains were present on this surface. In contrast, the clean $(22 \times \sqrt{3})$ reconstruction was not observed.

The (111) facet of the gold single crystal (fcc) is hexagonally close packed. We have, therefore, used a hexagonal coordinate system to describe it. In real space, the unit cell is defined to be $a = 2.884$ Å, $b = 2.884$ Å and $c = 2.356$ Å, which corresponds to a reciprocal unit cell with dimensions $a^* = b^* = 2.516$ Å^{-1} and $c^* = 2.667$ Å^{-1}. The components h and k describe the wavevector within the surface plane and l the wavevector normal to the surface plane (in units of the reciprocal lattice vectors). The in-plane measurements (at a fixed l, usually, l=0.03) performed are h scans, k scans and hk scans indicating along which in-plane direction the scans are recorded, or the ω scans [102], which allow the determination of the total peak intensities and relative orientations of the peak with respect to the gold substrate. Out-of-plane measurements (rod scans) in which l is varied at fixed h, k positions were also recorded. The reciprocal space was investigated in the range of h, k and l close to 2 both in- and out-of-plane.

The in-plane measurements reveal satellite peaks around the Bragg peaks at integer h, k values. The hk scans around (1,1) shown in Fig. 5.10a are representative XRD profiles providing detailed information about the satellite peaks. To illustrate the situation more clearly, we have plotted several hk scans together in this figure. The additional peaks at (0.96, 0.96), (1.04, 1.04) are clearly evident. The ω scan across the (0.96, 0.96) peak is shown in Fig. 5.10b together with a fit to a Gaussian line shape. The results of the fitting reveal that the peak is centered at 0.03°, which indicates that there is no rotation of this peak (most likely from the superstructure) with respect to the close-packed $[1\bar{1}0]$ direction of the Au(111) surface corresponding to $\omega = 0°$. This indicates that the moiré structure is preferentially aligned with the gold lattice ($\Phi = 0$, $\theta = 0$). The XRD measurements on the clean $(22 \times \sqrt{3})$ reconstructed Au(111) also found satellite peaks around Bragg peaks [36]. However, STM analysis on this single crystal surface before and after XRD experiment did not observe the presence of the

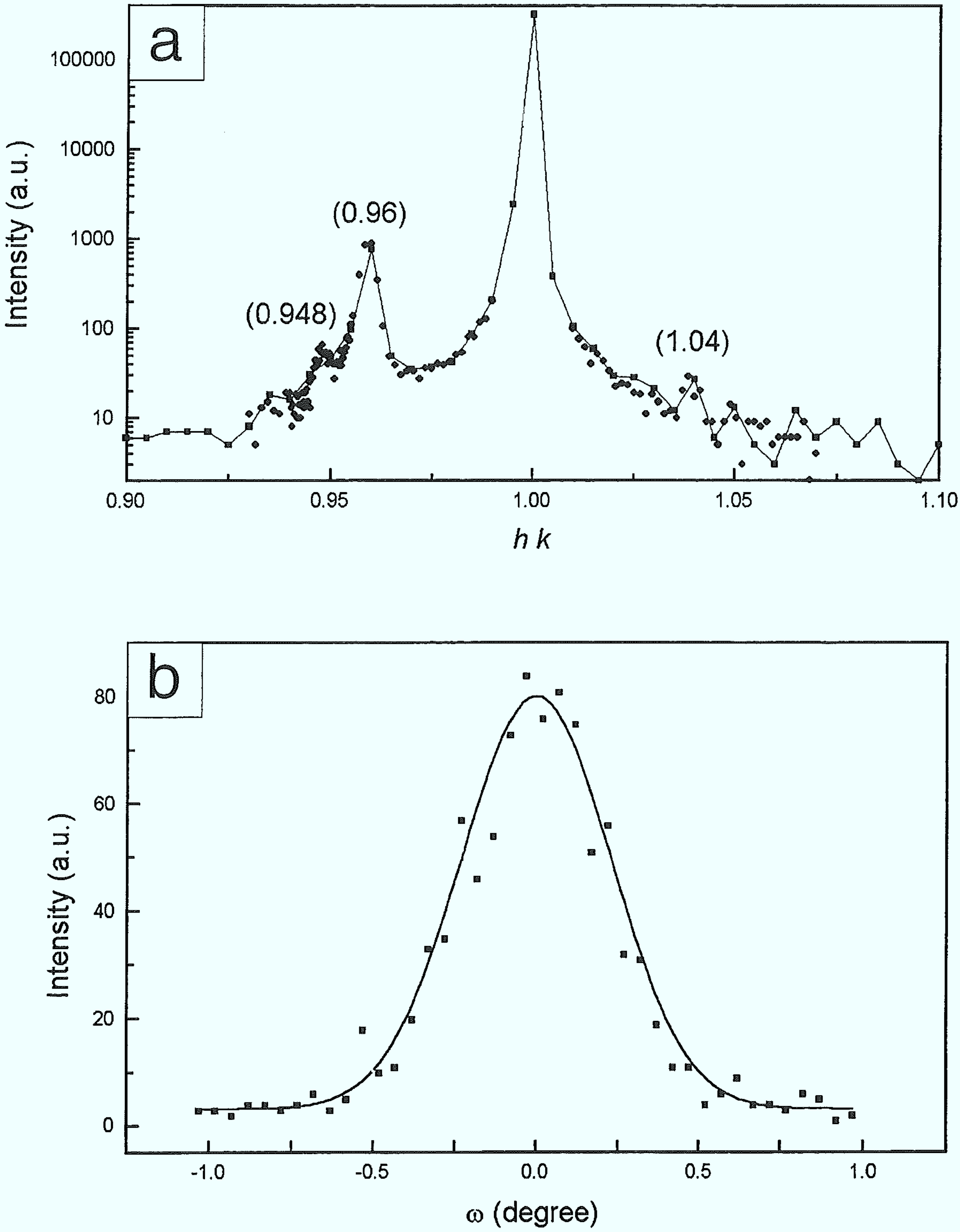

Figure 5.10: (a) Radial (*hk*) scans in the vicinity of the (1, 1) Bragg peak, showing several satellite peaks. (b) ω scan (0.96, 0.96) with a fitted Gaussian line shape peak.

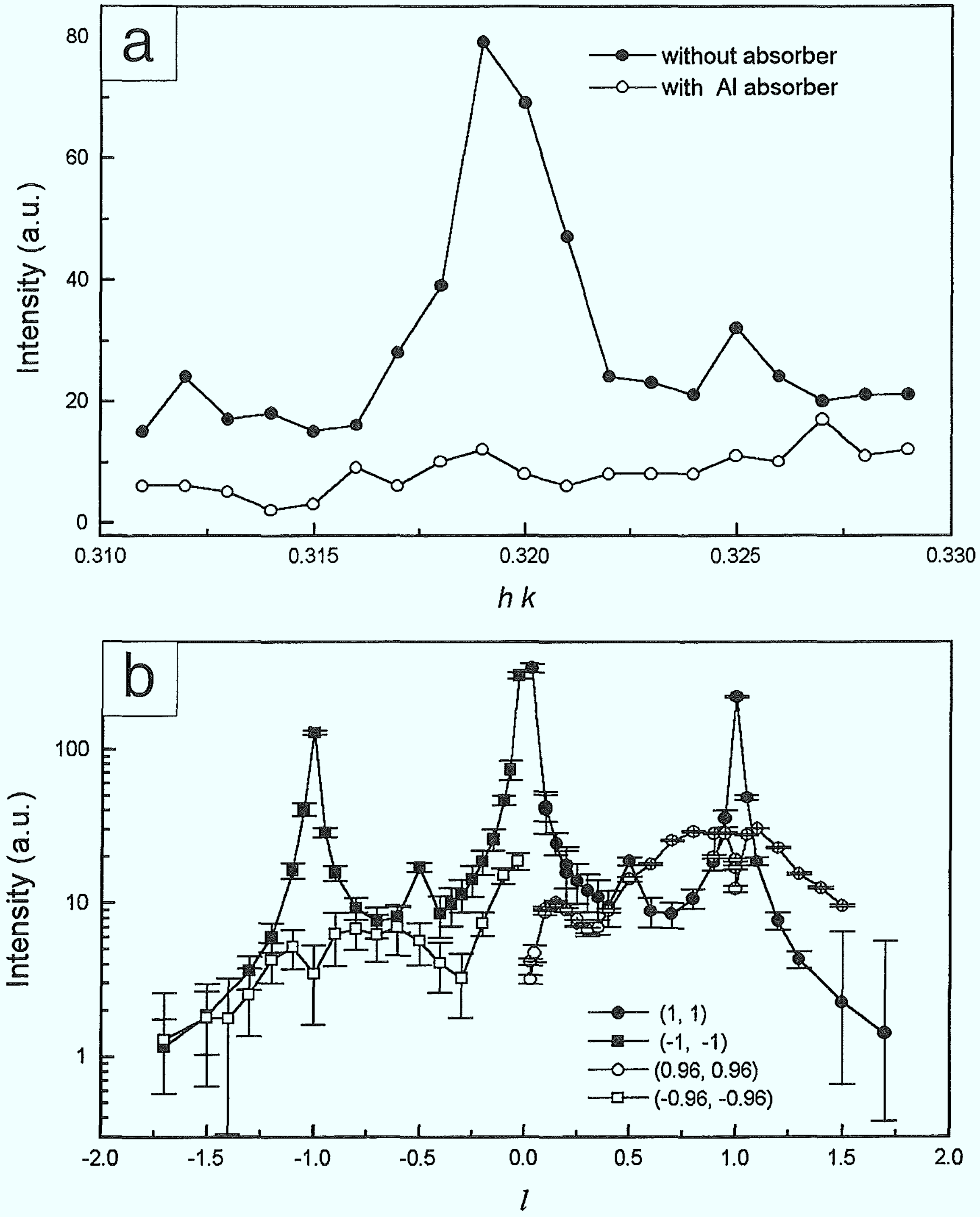

Figure 5.11: (a) Radical (hk) scans in the vicinity of (1/3, 1/3), showing a peak centered at the position of (0.32, 0.32). (b) Out of plane measurements (rod scans).

$(22 \times \sqrt{3})$ reconstruction, only the hexagonally reconstructed and the (1×1) structures were observed. This strongly suggests that the observed satellite peaks are due to the long-range hexagonal superstructure.

Note, however, that the fitting yields a peak width of about 0.455°, which is much larger than the width of 0.069° of a similar scan taken across the (1, 1) position. In diffraction measurements, both the domain size (this surface is only partially reconstructed) and the sample mosaic can affect the peak width. Also, in this case the slight distortion of the superstructure can result in a broadening of the satellite peaks.

The other important feature of the oxygen induced reconstruction is the formation of a $(\sqrt{3} \times \sqrt{3})$R30° structure as observed by STM in real space. Indeed, the *hk* scans recorded in the vicinity of the $\sqrt{3}$ position revealed a diffraction peak, which provides evidence for the presence of such a structure on this surface. The radial scans shown in Fig. 5.11a reveals a peak centered at the position of (0.32, 0.32). A simple method is often used in XRD experiments to distinguish harmonic peaks from peaks of the real structure: the use of adsorber during acquisition. While the use of adsorber will usually not affect the harmonic peaks, it, indeed, reduces the peak intensity from the real structure. We adopted this method here, and the results are presented in Fig. 5.11a. It can be seen that with the 0.5 mm Al absorber during acquisition, the peak intensity is strongly reduced and almost not discernible. This indicates that this peak reflects the real surface structure. The fact that the peak center is not at the exact $\sqrt{3}$ position (0.33) shows a distortion of the structure from a perfect $(\sqrt{3} \times \sqrt{3})$R30° structure with respect to the bulk Au(111). Actually, the peak shift corresponds to a 4% expansion to the normal $\sqrt{3}$ structure. Combined with the observation of the main satellite peak at a position of (0.96, 0.96), we infer that the topmost gold layer is *expanded* by about 4% in real space and that the oxygen atoms form a commensurate $(\sqrt{3} \times \sqrt{3})$R30° structure with the topmost gold layer. This expansion is also consistent with the long-range moiré-like superstructure with a periodicity of $\sim$ 70 Å as observed with STM. The XRD results are therefore in general agreement with the STM observations. Moreover, the XRD measurement complements the STM studies. As discussed above, the hexagonal superstructure can be explained by the formation of a moiré-like pattern. In fact, the origin of the contrast in moiré-type STM images is quite complicated [103], since STM images reflect electronic states of surfaces. In some cases, the contrast of the moiré patterns may depend strongly on the tunneling parameters used in the imaging.

The results of the out-of-plane measurements are illustrated in the plots shown in Fig. 5.11b. Only 4 rod scans are presented here, which were measured at the positions of (1, 1), (-1, -1), (0.96, 0.96) and (-0.96, -0.96) with l varying from -1.8 to 1.8. For an ideal (111) terminated Au crystal, there should be no intensities except at the positions of Bragg peaks (integer l values). The intensity variations of the rods (0.96, 0.96) and (-0.96, -0.96) provide information on the surface normal structure and will be analyzed in the future.

5.5 Conclusions

Two types of oxygen induced reconstructions on the Au(111) surface have been observed after annealing in high pressure oxygen at high temperatures: (i) a hexagonal long-range reconstruction with a periodicity of 60-80 Å and a corrugation of ~ 0.5 Å. At the atomic scale this surface exhibits a $(\sqrt{3}\times\sqrt{3})$R30° structure, which we attribute to atomic oxygen strongly chemisorbed at the Au(111) surface. The superstructure can be understood from a quantitative moiré analysis. The high sensitivity of the moiré pattern to local surface strain could explain the observed distortions of the hexagonal superstructure as well as the variation of the periodicity. (ii) a "modified" herringbone pattern related to the original herringbone reconstruction of the clean Au(111) surface, but with additional depressions in some of the fcc-regions between the reconstruction double-lines. At the atomic scale this surface exhibits a characteristic 'row structure' with $\sqrt{3}$ periodicity.

The observation of localized areas of the long-range hexagonal superstructure indicates that the restructuring of the surface upon exposure to oxygen proceeds via a nucleation and growth process. Together with the observation of only the 'modified' herringbone reconstruction after repeated cycles of annealing of the single crystals, we conclude that surface defects or impurities should play a crucial role in the nucleation of the oxygen induced hexagonal reconstruction.

The surface composition has been characterized by XPS and AES. Preliminary results show that the concentration of the impurities like Ca, Si are below the detection limit of XPS and AES. Therefore, the appearance of the hexagonal superstructure cannot be attributed to the formation of a complex surface compound involving a sizable amount of impurities. Instead, the observed structures appear to be intrinsically induced by the chemisorption of oxygen on Au(111).

The oxygen-induced hexagonal reconstruction is found very stable in air and enabled the investigation using synchrotron X-ray diffraction. In the XRD spectra both the diffraction peaks which correspond to the $(\sqrt{3}\times\sqrt{3})$R30° structure and those due to the long-range hexagonal superstructure have been observed in reciprocal space. The shift of the peaks from the expected normal $\sqrt{3}$ position can be explained by an expansion of the topmost gold layer with respect to its underlying bulk lattice. The oxygen atoms are most likely in registry with the topmost gold layer.

Chapter 6

The behavior of the reconstructed Au(111) surface under external strain

6.1 Introduction

It has been realized that even in equilibrium residual stresses are present at solid surfaces which may have an important influence on the actual surface structures. To create new surfaces of materials, excess work must be exerted to break the bonds within bulk materials. The surface free energy γ is defined as the reversible work per unit area needed to *create* the surface. There is another type of surface quantity that is associated with the reversible work per unit area needed to *stretch* a surface [104]. This work is defined as the surface stress σ_{ij}, which is a second rank tensor and is related to surface free energy γ by the Shuttleworth equation:

$$\sigma_{ij} = \gamma\delta_{ij} + \frac{\partial\gamma}{\partial\epsilon_{ij}} \tag{6.1}$$

where δ_{ij} is Kronecker delta function, and ϵ_{ij} the surface elastic strain tensor, with i, j=1, 2.

We recall that surface stress σ_{ij} and surface free energy γ are identical in the case of fluids: when a liquid film is stretched atoms or molecules move out from the bulk to form the new surface which has the same structure (density) as the existing one. In other words, the surface free energy remains constant during the deformation. In contrast to liquids, when a solid surface is deformed the distances between the atoms will change and the second term in the equation (6.1) is not zero. Therefore, σ and γ are usually not the same for solid surfaces. As discussed in chapter 3, surface stress is usually present at solid surfaces. In some cases it may be energetically favorable to relieve the surface stress through a rearrangement of the surface atoms, i.e. a surface reconstruction. This is the case for the $(22 \times \sqrt{3})$ reconstruction of the Au(111) surface. Recently, a large number of studies have been devoted to the relationship between surface stress and surface reconstruction [25, 28, 105, 108, 109]. Meanwhile, surface stresses of some metal and semiconductor crystals have been calculated theoretically [106, 107, 110] and several methods have been developed to measure the surface stress experimentally [111, 112, 113].

On the other hand, the surface strain ϵ_{ij} is directly related to the surface stress. As indicated in some studies [114, 115], the knowledge of the surface stress alone is insufficient to allow the determination of the surface structure, because the elastic properties of the near-surface region may differ considerably from that of the bulk material. The study of the surface strain can give the information about both the surface stress and the near-surface elastic response and may thus predict the energetically favorable surface structures. The correlation between strain and reconstruction has been studied in the case of Ge thin films grown on Si(111) [114] and other systems [116]. A controlled experiment to demonstrate the direct influence of *external* strain on reconstruction has been successfully performed by Men, Packard and Webb [117]. In their experiment, a thin Si(100) crystal (0.3 mm thick) was fixed at one end, and loaded at the other end. In this way a uniaxial strain was induced at the surface varying linearly along the length of the sample. The results of the experiment show that external applied strain produces a reversible asymmetric population of alternating (2×1) and (1×2) reconstructed terraces. To understand the physical origin of this observation, Alerhand, Vanderbilt, Meade and Joannopoulos (AVMJ) [118] have developed a theory, which predicts the spontaneous formation of elastic domains on surfaces with degenerate phases but anisotropic intrinsic surface stress tensors. This theory provides a correct description of the experimental results on the Si(100) (2×1) and (1×2) reconstructed surface [119].

It is obvious that the study of the surface structure as a function of external strain can provide very useful results and will have an impact on the development of the theoretical work. In this context, we have developed a special experimental set-up, which allows STM investigations of the surface structure under externally applied strain. The first experiments were performed on the reconstructed Au(111) surface, since the results presented in chapter 3 have shown that the reconstruction in air usually behaves quite similar as in UHV.

6.2 Theoretical background

6.2.1 Frenkel-Kontorova model

In theoretical studies of the reconstruction of Au(111), the Frenkel-Kontorova (FK) model [120] has been used to describe this $(22 \times \sqrt{3})$ reconstruction [38, 29, 121, 122, 123]. This model describes the physical system as illustrated in Fig. 6.1a. For simplicity, only the one-dimensional (1D) model is drawn here. Atoms in an array are connected by springs of modulus k and natural length a_0. At the same time, they interact with an underlying cosine wave potential of periodicity b and peak-to-peak amplitude $2V_0$. This model has been used to describe atoms adsorbed on a surface. It can also be used to describe the situation on the surface of a clean crystal where the preferred bond-length within the surface layer is different from that of the bulk — as in the case of the reconstructed Au(111) surface. The Hamiltonian of the system can

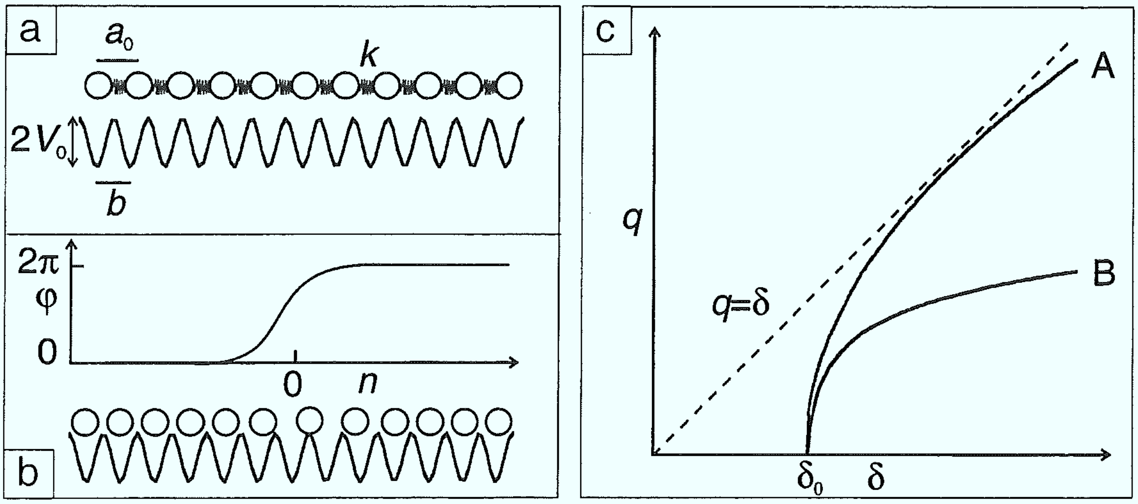

Figure 6.1: Schematic illustration of the one-dimensional (1D) Frenkel-Kontorova model. (b) The 1D Frank and van der Merwe (FVdM) solution showing the formation of soliton walls. (c) Measured misfit q as a function of natural misfit δ. A: continuum solution of the 1D FVdM model. B: Solution of the two dimensional model after Pokrovsky and Talapov [126].

be written as [69]

$$H = \sum_n \frac{k}{2}(x_{n+1} - x_n - a_0)^2 + V_0(1 - \cos\frac{2\pi}{b}x_n) \tag{6.2}$$

where x_n is the position of the nth atom in the chain. Frank and van der Merwe found the ground states of this one-dimensional model with the additional assumption that the discrete index n can be treated as a continuous variable [124]. Only in the case of a small V_0 the solutions of the discrete model show the same general features as solutions of the continuum version [125]. If the amplitude $2V_0$ of the potential is large enough, the atoms are pinned to the minima of the substrate potential and the situation cannot be modeled by a continuum theory. The first-principles calculations show that the substrate potential of Au(111) is only about 0.19 eV [38]. By introducing the phase $\phi_n \equiv 2\pi(x_n - nb)/b$ and transforming to the continuum limit $\phi_n - \phi_{n-1} = d\phi/dn$, the Hamiltonian becomes

$$H = \int [\frac{kb^2}{8\pi^2}(\frac{d\phi}{dn} - 2\pi\delta)^2 + V_0(1 - \cos\phi)]dn \tag{6.3}$$

with $\delta \equiv (b - a_0)/b$. δ is the relative 'natural misfit' between the two lattices. The ground state is found among the solutions of the 1D sine-Gordon equation

$$\frac{d^2\phi(n)}{dn^2} = A\sin\phi \text{ with } A = (\frac{2\pi}{b})^2\frac{V_0}{k}\,. \tag{6.4}$$

One of the solutions to this equation is the soliton

$$\phi(n) = 4\tan^{-1}[\exp(n\sqrt{A})]. \tag{6.5}$$

This solution describes a wall, centered at $n = 0$, which separates two commensurate regions, one with $\phi = 0$, the other with $\phi = 2\pi$, as illustrated schematically in Fig.

6.1b. The wall represents an extra atom which has been added to the chain. In general the solutions consist of a soliton lattice, i.e. a regular array of solitons separated by a distance l. The average misfit between the chain and the lattice is $q \equiv (b-a)/b = 1/l$. The difference in free energy per unit length can be written as

$$\Delta E = 8\sqrt{A}\,|q|\,[1+4\exp(-\sqrt{A}\,|q|)] - 4\pi^2\,|q|\,\delta. \tag{6.6}$$

According to this equation, for parameters such that $2\sqrt{A}/(\pi^2\delta) > 1$, ΔE is necessarily positive, and the commensurate phase (*q=0*) is thermodynamically favored. If $2\sqrt{A}/(\pi^2\delta) < 1$, an incommensurate domain wall phase with $l = 1/q$ being the distance between the walls is favored. It is found that q varies as a function of δ as follows

$$q \sim ln^{-1}(\delta - \delta_c). \tag{6.7}$$

The two-dimensional case was solved by Pokrovsky and Talapov [126] who found that

$$q \sim (\delta - \delta_c)^{1/2} \tag{6.8}$$

The 1D and 2D curves are shown in Fig. 6.1c and marked with A and B, respectively. The dashed line represents the completely incommensurate case (V_0=0) where $q = \delta$. At $\delta = \delta_c$, there will be a continuous transformation from the incommensurate to the commensurate phase. Although FK-model is quite simple, it can reproduce the basic features when applied to explain the $(22 \times \sqrt{3})$ reconstruction of Au(111) [33]. Hence, the $(22 \times \sqrt{3})$ reconstruction can be regarded as an incommensurate structure with soliton walls (reconstruction lines) separating commensurate fcc and hcp domains. Any change of the natural misfit δ, e.g. through an external strain ϵ with $b = b_0(1+\epsilon)$, $b_0 = 2.884$ Å, will induce a change in

$$\delta(\epsilon) = 1 - a_0/[b_0(1+\epsilon)]. \tag{6.9}$$

To calculate the changing of the natural misfit, we use the value of a_0=2.7744 Å as obtained by Narasimhan and Vanderbilt from a fit of the structural properties of the Au(111) reconstruction to a FK-model [29]. According to the Eqs. 6.7 and 6.8, the change of δ will further lead to a change of $q = 1/l$, where l is the periodicity of the $(22 \times \sqrt{3})$ reconstruction. Since in our case the applied strain is a compressive one (ϵ is negative), it will cause a reduction of δ. If δ becomes smaller than δ_c, the incommensurate structure (reconstructed phase) will transform to the commensurate (1×1) surface.

6.2.2 Implications of the AVMJ theory

Although the FK model discussed above can describe the $(22 \times \sqrt{3})$ reconstruction, it fails to explain the physical origin of the herringbone superstructure observed on Au(111). Narasimhan and Vanderbilt have applied the AVMJ theory to Au(111) to give a possible explanation for the presence of a herringbone pattern [29]. The results of the AVMJ theory suggest that if the surface has reconstructed domains with the same surface energy but different orientations and therefore different intrinsic stress tensors, this will lead to the spontaneous formation of elastic-stress domains due to

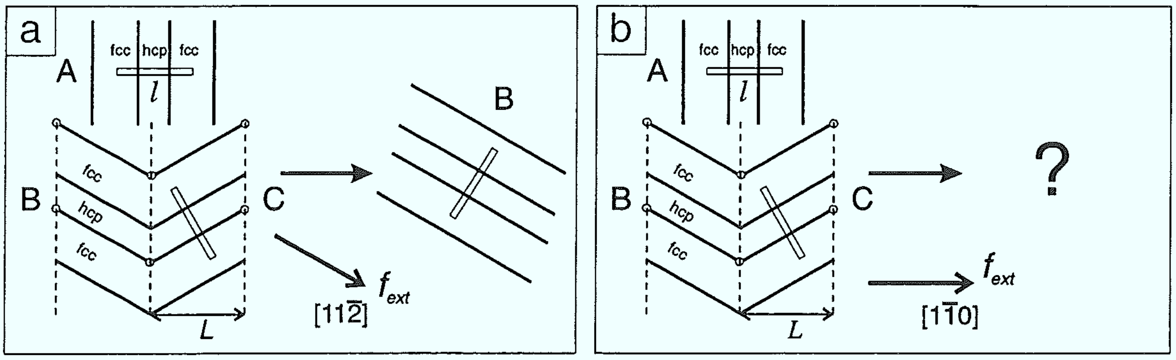

Figure 6.2: Schematic representation of the change of the $(22 \times \sqrt{3})$ domains under an externally applied compressive strain. (a) External strain along the $[11\bar{2}]$ direction: domains of type B will be favored. (b) External strain along the $[1\bar{1}0]$ direction: domains of type A will be disfavored; the influence on domains B and C should be equivalent.

long-range elastic interactions. Since the $(22 \times \sqrt{3})$ reconstruction is thought to only relieve the tensile stress along $[1\bar{1}0]$ (i.e. perpendicular to the reconstruction lines), it has an anisotropic stress tensor. Also, the reconstruction cell has three possible orientations with same energy. Therefore, the Au(111) surface satisfies the conditions for the spontaneous formation of stress domains. Based on this theory, Narasimhan and Vanderbilt indeed find that the herringbone structure is favored when the long-range elastic interactions are considered. The theoretical estimated domain wall spacing L in herringbone structure lies between 140 and 980 Å. Some of the experimental observed values are 162 Å [36] and 140 Å [35]. The terminology used is explained here [29]: *soliton walls* are those separating hcp-like and fcc-like regions within the $(22 \times \sqrt{3})$ reconstruction, whereas *domain walls* separate different orientations of the $(22 \times \sqrt{3})$ reconstruction.

Since the surface stress produces a long-range strain field extending into the bulk substrate, according to the AVMJ theory, the system may lower its energy by elastic relaxation i.e. the rearrangement of the domain walls. Consequently, in the presence of an anisotropic *external* strain, the orientational degeneracy of the surface energy will be lifted and the favored domains will grow at the expense of the others. In this context, the type of change of the reconstruction patterns on Au(111) can be also predicted by this theory. The three possible oriented domains of the $(22 \times \sqrt{3})$ are shown in Fig. 6.2. While domain A is drawn as in the uniaxial $(22 \times \sqrt{3})$ reconstruction, domains B and C are connected together as in the herringbone structure. If an external compressive force f_{ext} is applied along the $[11\bar{2}]$ direction (Fig. 6.2a), it is obvious that the domain B is unaffected, since in the ideal case, the applied strain should have no influence on this domain. However, from the results of the FK model we know that in this process the periodicity of $(22 \times \sqrt{3})$ reconstruction should also change because of the dependence of the soliton density on the strain. The situation is less clear for an external compressive force f_{ext} acting along the $[1\bar{1}0]$ direction (Fig. 6.2b). The strain will clearly not favor domain A, but now the domains B and C will be affected by symmetry in the same way; this may lead to a change of the herringbone periodicity L. However, the above discussions remains only qualitative.

6.3 Experimental set-up

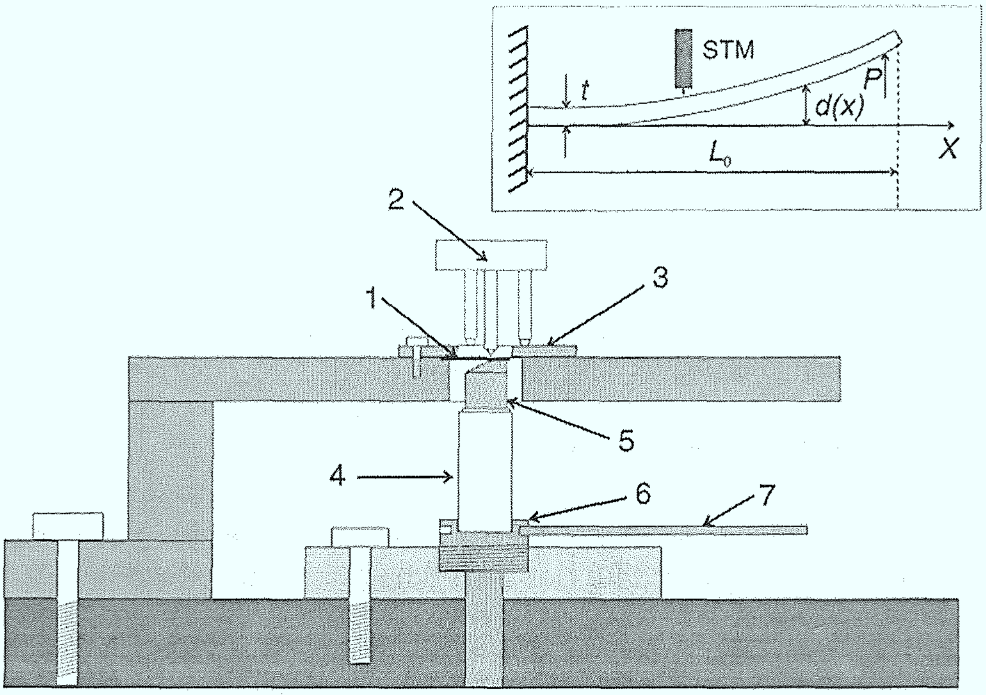

Figure 6.3: Schematic diagram of the experimental set-up, allowing STM investigations of the effect of external strain. (1) thin Au(111) single crystal (0.3 mm); (2) STM; (3) walk ring; (4) driving piezo; (5) pushing piston; (6) fine screw; (7) lever for rotating the screw. The crystal is fixed at one end by the walk ring. The free end of the crystal can be moved up by the driving piezo, thereby, bending the crystal.

The mechanism of loading a cantilevered bar is often used in bending experiments. Men et al. [117] have also used this design in their experiments on Si(100). The details of the experimental set-up used in this work are illustrated in Fig. 6.3. The sample (1) is fixed at one end by the "walk-ring" (3); under the free end the driving piezo (4) together with the fine screw (6) is used to bend the sample in a well-controlled manner. The concave surface of the sample which can be investigated by STM (2), is compressed in the direction along the bar. The pushing piston (5), which is made of stainless steel and mounted on the driving piezo, is isolated from ground. The piston is connected to an ohmmeter for the detection of an ohmic contact with the grounded sample. The gradient of the screw is 0.5 mm/turn. A lever (7) is used to turn the screw up or down. After the sample is fixed at one end, the driving piezo is approached to the back side of the sample by carefully rotating the lever (7). The contact of the piston with the sample will induce an ohmic contact which is detected by the ohmmeter. This position is regarded as the zero of the sample deflection. The further deflection of the sample is controlled by the extension of the driving piezo by applying a voltage to it. The nominal extension of the driving piezo is 15 μm for an applied voltage of 100 V. The voltage supply is a series connection of five batteries (22 V for each) with voltage output controlled by a potentiometer.

According to the elastic theory for the cantilevered bar, if the bending is within the elastic regime, the deflection of the bar *d(x)* at position x from the fixed end can be expressed as [127]

$$d(x) = \frac{Px^2(3L_0 - x)}{6B}, \tag{6.10}$$

where P is the load on the free end of the bar, B is a constant related to the geometry of the bar, L_0 is the length of the bar and t the thickness of the sample. The configuration of the cantilevered bar is illustrated in the inset of the Fig. 6.3.

The strain ϵ at the surface of the bar can be calculated as:

$$\epsilon = \pm\frac{t}{2R}; \quad \frac{1}{R} = \frac{\mathrm{d}^2 d(x)}{\mathrm{d}x^2} = \frac{P}{B}(L_0 - x) = \frac{6d(x)(L_0 - x)}{x^2(3L_0 - x)} \tag{6.11}$$

where R is the radius of the curvature; the minus sign stands for the compression of the surface lattice, the plus sign for the elongation of the bottom surface. Hence, the uniaxial strain varies linearly along the length of the bar. A 15 μm deflection of the free end corresponds to a maxim strain in the present set-up of $\epsilon = 8.3 \cdot 10^{-5}$ at the fixed end of the bar.

The samples used were two 0.3 mm thick Au(111) single crystals, 10 mm long and 5 mm wide, with the longer axis aligned to the $[1\bar{1}0]$ and $[11\bar{2}]$ direction, respectively. The crystals were cut and mechanically polished to have a (111) surface orientation. The bulk mosaicity of the crystals is $< 0.2°$. The crystals were further annealed alternatingly in an oxygen and argon atmosphere at high temperatures until the average terrace width reached about 2000 Å. Before each experiment, the crystal was annealed in an argon atmosphere at $T = 800$ °C for a time interval from 2 to 16 hours. This preparation routinely resulted in a clean surface exhibiting the $(22\times\sqrt{3})$ reconstruction.

6.4 Results

6.4.1 Elastic bending and its verification

The maximum strain applied in this bending experiments is only in the order of 10^{-5} and it is reasonable to assume that the bending is in the elastic regime. This has been verified by a direct measurement using the STM to determine the local deflection of the sample. To this end, the tip is first moved into the tunneling range, and then retracted by applying a fixed voltage on the z-piezo. The driving piezo under the free end of the sample is moved up by applying a voltage and the movement of the piezo pushes the sample up. Therefore, a smaller voltage is needed to drive the STM tip back into the tunneling range again. If we know the characteristics of the STM piezo and the difference between the two voltages needed to approach the tip before and after loading of the sample, the sample deflection can be inferred. The extension of the STM piezo is calibrated to be 32 Å/V by measuring the height of a monatomic step at the Au(111) surface. To avoid a possible hysteresis effect, we waited for 3 minutes at each measuring point after applying the voltage on the STM piezo. Since the voltage applied to the z-piezo reaches its maximum at 200 V, the tip can be retracted with the

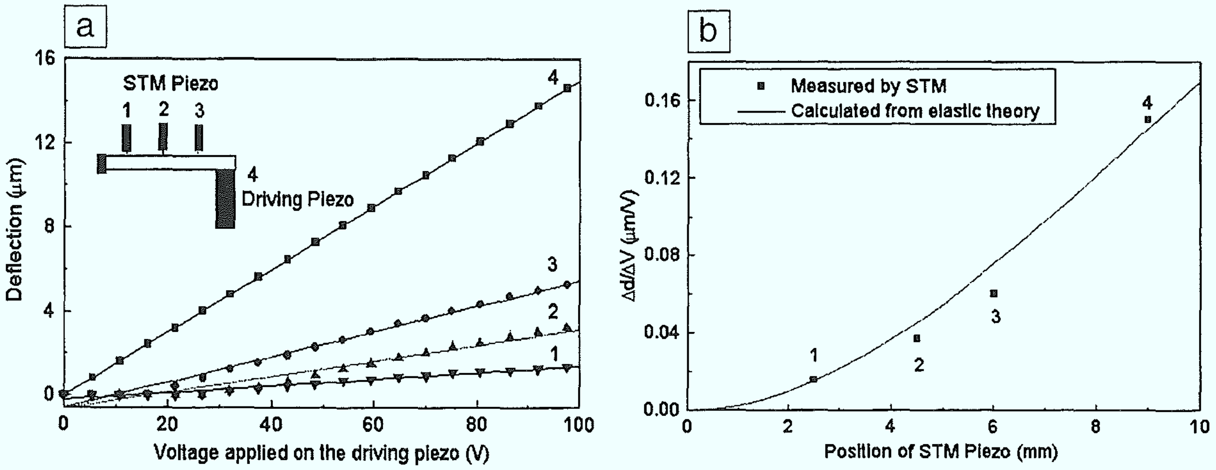

Figure 6.4: (a) Deflections at different positions along the Au crystal measured by STM as the function of the voltage applied to the driving piezo. (b) Comparison of the measured data with those calculated from the elastic theory.

piezo no more than 0.64 μm. Instead, we have to retract the tip by moving the STM using the coarse approach. In the ideal case the coarse approach should only cause a vertical movement of the tip, but usually it introduces a slight lateral movement of the STM, too. However, in the present context this lateral movement is negligible because it is of the order of a few micrometer. Only if the lateral movement were of the order of a millimeter, the change of the local deflection would become significant. In this way, the vertical deflection of the sample is measured as the function of the voltage applied to the driving piezo. The measurement was repeated at three different positions (1, 2 and 3 in the inset of Fig. 6.4a) along the sample and the results are plotted in Fig. 6.4a. The reference curve 4 is the nominal extension of the driving piezo. It can be seen that all three data-sets agree well with a linear deflection function, which is expected from the elastic theory. To analyze the data quantitatively, the slopes of the lines fitted to the data are plotted as a function of the position of the STM tip, which are shown in Fig. 6.4b. The expected curve calculated from the theory using the geometric and elastic constants for the case of the Au(111) samples is also plotted. It can be seen that calculated curve fits the data quite well, indicating that the bending experiments are indeed within the elastic regime. During the bending experiments the local deflection $d(x)$ of the sample was measured and with the knowledge of the STM position x, the strain can be calculated using Eq. 6.11.

6.4.2 Influence of external strain on the $(22 \times \sqrt{3})$ reconstruction

Fig. 6.5a shows an image obtained from the thin Au(111) single crystal surface after annealing first in oxygen at 600°C for 16 hours and then in argon at 700°C for 1 hour. The longer axis of the crystal is aligned along the $[11\bar{2}]$ direction, which implies that the external strain is also along this direction. As explained in chapter 3, the corrugation due to the reconstruction double-lines are the characteristic signature of the surface exhibiting the $(22 \times \sqrt{3})$ reconstruction. Before the acquisition of this image, 16 scans

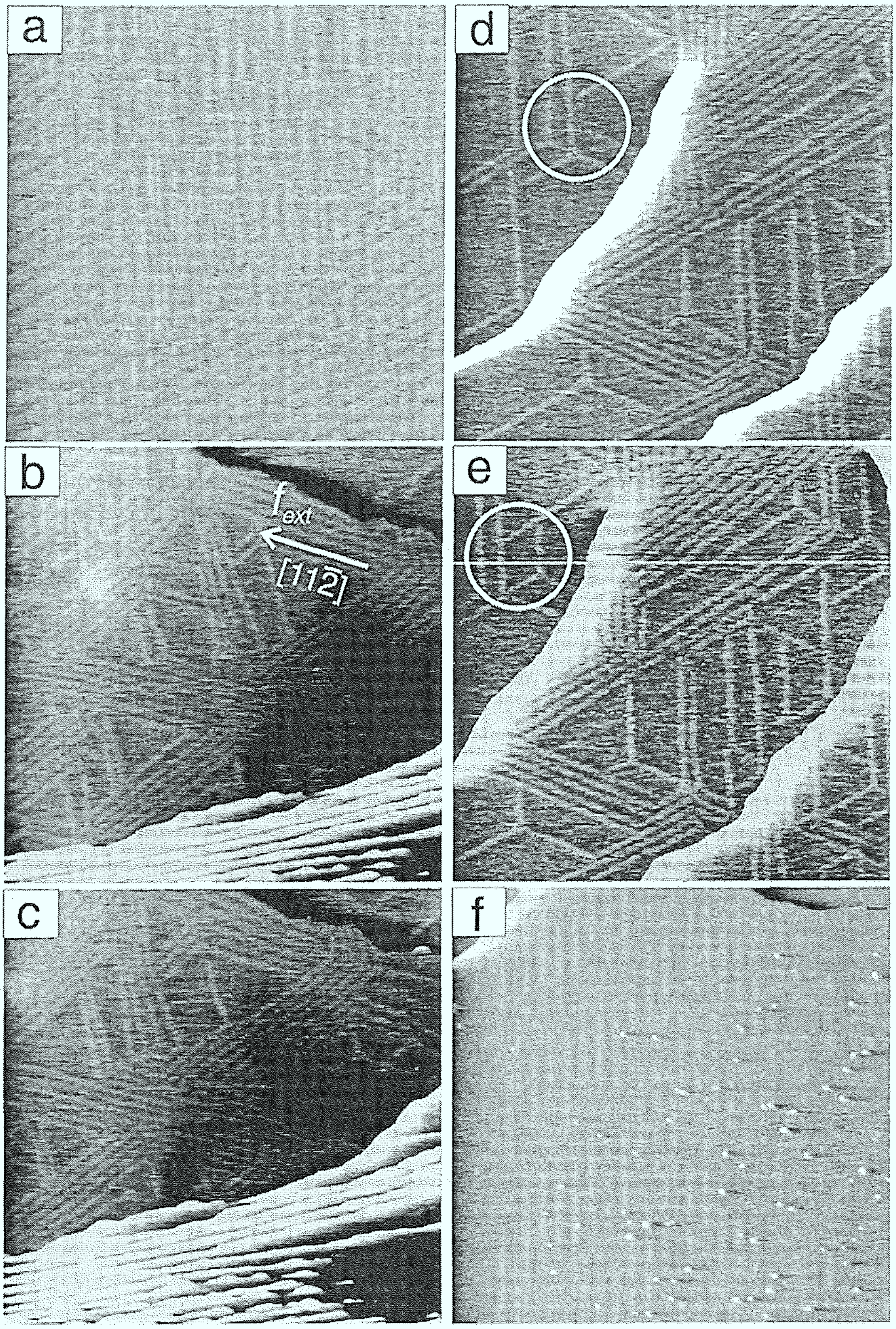

Figure 6.5: (a) STM topograph (1550 × 1550 Å) obtained from the Au(111) thin crystal surface, showing the $(22 \times \sqrt{3})$ reconstruction without external strain ($\epsilon = 0$). Tunneling parameters: V_t=75 mV, I_t=17 nA. (b)-(f): STM images (3100 × 3100 Å, V_t=75 mV, I_t=12 nA) taken from the Au(111) thin crystal surface under external strain, revealing the changes of the reconstruction pattern with increasing strain (b-e, $\epsilon = 0.4 \cdot 10^{-5}$, $0.6 \cdot 10^{-5}$, $1.0 \cdot 10^{-5}$ and $1.1 \cdot 10^{-5}$) acting along the direction indicated be the arrow in (b). Finally (f), the strain induced structural transformation (deconstruction) leads to the formation of gold islands on the surface ($\epsilon = 1.3 \cdot 10^{-5}$).

were made in this area. No significant change of the reconstruction pattern due to the scanning or contamination was observed. Then an external strain was applied by increasing the voltage on the driving piezo in steps of 2.3 V, corresponding to a deflection of $\sim 0.35\ \mu$m at the free end per step.

The STM images were recorded 1 minute after the deflection. Only 5 images from this series are presented in Figs. 6.5b-f. Due to the low magnification used for the acquisition the reconstruction double-lines appear as 'single' lines in the images. The direction of the bending is shown by the white arrow drawn in Fig. 6.5b. The change of the reconstruction pattern is evident. In Figs. 6.5b and c, there are some triangular-shaped regions surrounded by the reconstruction double-lines. In these regions the surface is no longer reconstructed but instead, is likely to exhibit a smooth (1×1) structure. As discussed above, the results of theoretical studies predict an increase of the distance l between soliton walls with a decrease of the natural misfit (or the increasing compressive strain in this case). A homogeneous change of l would be expected for a corresponding continuos movement of each soliton wall as a response to the applied strain. Since soliton walls are partial dislocations, they might be pinned by the substrate. It is, therefore, conceivable that some of the soliton walls disappear, while the distance between some others are not changed. This is, in fact, what is observed in the STM images. This results in an increase of the average distance l, but producing large, localized patches of 'deconstructed' surface.

Upon further increasing of the strain, the (1×1) regions become larger. Comparing the patterns in the area marked by the white circles in Fig. 6.5d and Fig. 6.5e, the movement of a single soliton wall is evident. The reappearance of the reconstruction lines in previously deconstructed region indicates that long-range elastic interactions are involved in this process. Also, star-like patterns are appearing, they are similar to the essential elements of the partially reconstructed Pt(111) surface [128], but are rarely observed on the unloaded clean Au(111) surface. Since the reconstructed phase is more densely packed, the excess atoms should be expelled from the topmost layer during the phase transformation. This situation is indeed observed in the image shown in Fig. 6.5f. The reconstruction lines are no longer present in this area, instead, many small islands are present on the surface. The islands were found to be not stable on the surface. After two further scans, they have completely disappeared leaving a flat deconstructed surface behind. Since the diffusion rate is rather high, it is most likely that they have diffused to the step edge and been trapped there. After recording Fig. 6.5f, we moved the STM to another area with the similar strain and found that locally the reconstruction could still exist. This reveals the fact that the transformation is inhomogeneous and that the critical strain needed for the local transformation may be different from place to place and that the final step occurs in a very sharp transition. This is consistent with a 'critical' behavior as predicted by the theory. However, once the strain had reached a value of $1.9\cdot10^{-5}$, the reconstruction was rarely observed in that region. Therefore, this value was used to calculate the critical misfit δ_c (Eq. 6.9).

Using the STM images in this series, we have tried to make a quantitative analysis to find the relationship between the measured misfit q and the natural misfit δ. The natural misfit is calculated using Eq. 6.9, and the measured misfit q can be inferred

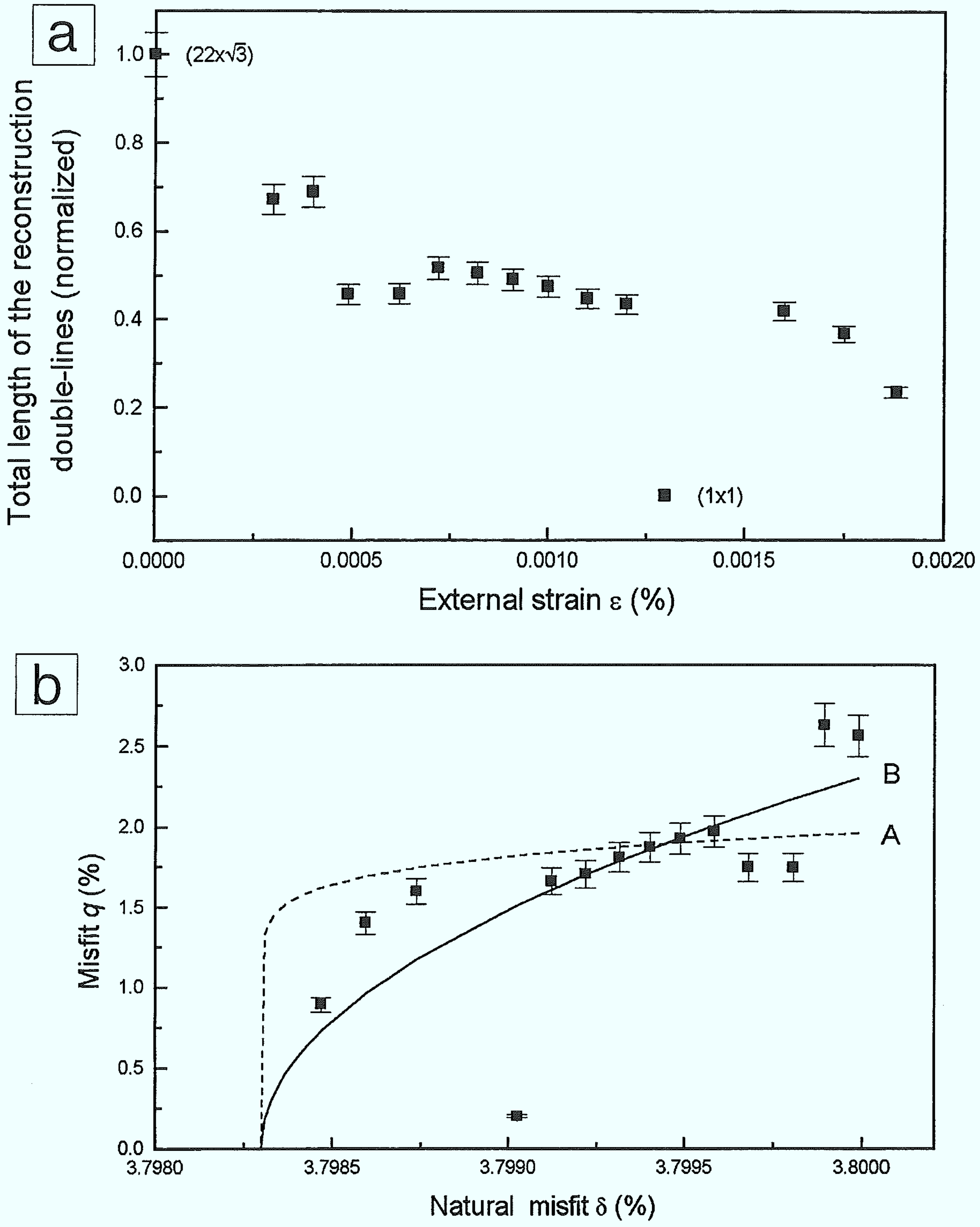

Figure 6.6: (a) Total length of the reconstruction double lines as a function of the external strain. (b) Relationship between the measured misfit q and the calculated natural misfit δ. Dashed line (A): data fitted by the continuum solution of the 1D FVdM model (Eq. 6.7). Solid line (B): data fitted by the solution of the two dimensional model (Eq. 6.8).

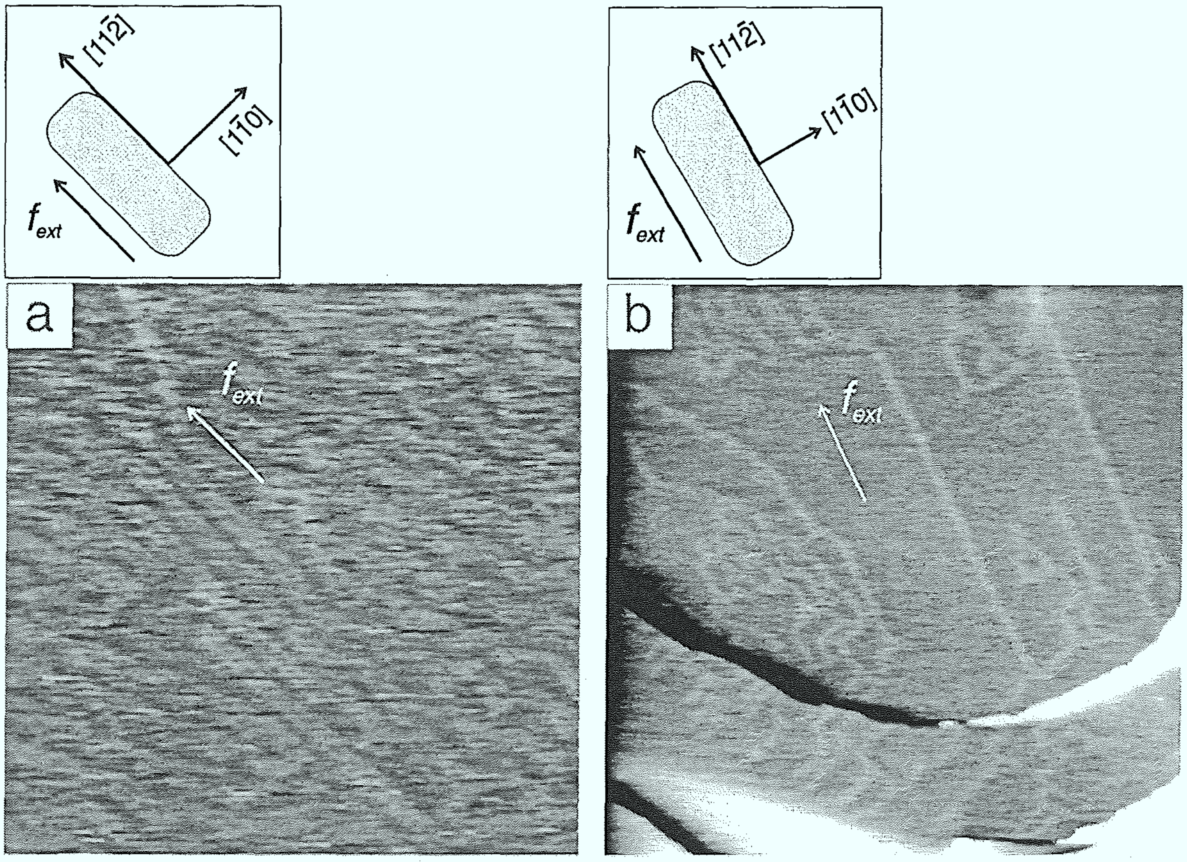

Figure 6.7: STM topographs taken from the Au(111) thin crystal surface under strain. The longer axis of the crystal is aligned along the [11$\bar{2}$] direction and the uniaxial strain is also along this direction. (a) Due to the presence of the strain field, the herringbone pattern rearranges and the domain with soliton walls parallel to the strain direction is favored (1200 × 1200 Å, $\epsilon = 7.9 \cdot 10^{-6}$, V_t=46 mV, I_t=16 nA). (b) Two reconstruction double-lines are preferentially aligned with the direction of the externally applied strain (2400 × 2400 Å, $\epsilon = 1 \cdot 10^{-5}$, V_t=27 mV, I_t=13.6 nA).

from the STM images. From the atomic structure of the reconstruction, we know that one extra Au atom is incorporated in each close-packed [1$\bar{1}$0] oriented atomic row when across a reconstruction double-line. The total length of all the reconstruction double-lines in an fixed area divided by the interrow spacing of the [1$\bar{1}$0] rows gives the number of total excess atoms in this area. The misfit q can be obtained by dividing the number of the excess atoms by the total number of Au surface atoms in this area. In this way, the misfit of the reconstructed area shown in Fig. 6.5a is calculated to be 3.8%, slightly lower than the value of 4.5% expected for a fully ($22 \times \sqrt{3}$) reconstructed Au(111) surface. Fig. 6.6a shows the total length of the reconstruction double lines obtained from each image in this series plotted against the external strain. The length is normalized to the length of double-lines in a quasi-fully reconstructed phase (3.8%). We can see that the length decreases with increasing external strain. The misfit q is plotted against the natural misfit δ in Fig. 6.6b. The dashed and solid lines marked A and B are fits of the experimental data to the 1D and 2D FK-model, respectively. We find that the experimental data can be relatively well fitted using the 2D FK-model.

After unloading the free end, the 'deconstructed' surface remains in its (1×1) structure and the spontaneous transformation of the (1×1) patches into reconstructed areas was not observed. We have no satisfying explanation for this phenomenon. However, after annealing the crystal at high temperatures, the reconstruction is again observed. The reconstruction process involves the removal of atoms from the steps and the incorporation into the terraces. The study on the nucleation process of the reconstruction of Pt(111) showed that the incorporation of a single atom into the terrace (nucleation of the reconstruction) is very difficult [128]. Therefore, this process may prevent the transformation to be reversible under our experimental conditions.

The influence of the external strain on the herringbone structure was also observed on the same Au(111) crystal. Figure 6.7 shows images from different series of measurements at different bending stage. The longer axis of this crystal is along the $[11\bar{2}]$ direction as indicated by the small schematics above the STM images. In the central area of Fig. 6.7a, four straight double-lines running along the $[11\bar{2}]$ direction are evident. Further examination reveals that the straight lines are connected with the zigzag patterns at their lower ends. This may give a clue that these straight lines are derived from the original herringbone structure. Comparing with the situation illustrated in Fig. 6.2a, it is obvious that the straight lines represent the favored B-type domains. Some small areas exhibiting the (1×1) structure are also found in this image, which indicates the decrease of the soliton-wall density. The trend of the reconstructed double-lines to align themselves parallel to the $[11\bar{2}]$ (external strain) direction is more clear in Fig. 6.7b. At this stage, the strain induced phase transformation to the (1×1) structure almost completed. The observed reconstruction patterns in the left and lower part of the image have already lost their long-range order. Surprisingly, two single reconstruction double-lines whose lengths exceed 1200 Å are observed to run along the $[11\bar{2}]$ direction. We may speculate that the isolated reconstruction double-lines are stabilized due to the external strain.

A strain induced phase transformation was also observed with the other thin Au(111) crystal, whose longer axis is oriented along the $[1\bar{1}0]$ direction. In other words, the uniaxial strain was applied along this direction in the bending experiments. According to the AVMJ theory discussed above, the rearrangement of the reconstruction domains in response to the external strain on these two crystals should have a different effect. This was indeed observed in our bending experiments, as seen in Fig. 6.8. At this stage, the herringbone-like structure is still discernible in the central area of Fig. 6.8a, without significant derivation from the usual herringbone pattern. However, in the lower part of this image, another type of reconstruction pattern is evident, which is surprisingly similar to the structure observed after Na adsorption on the reconstructed Au(111) [63]. As discussed above, in this case, the A-type domains in the herringbone structure are disfavored, but within the BC herringbone structure, both B- and C-type domains should be affected exactly the same way. Also, the periodicity of herringbone structure L can change in this case, since L is found to be related to the anisotropic stress tensor of the reconstruction unit cell, which will be affected by the external strain. Therefore, the observed change of the herringbone periodicity as seen in Fig. 6.8a can be qualitatively understood. Even in the presence of a relative large strain, we

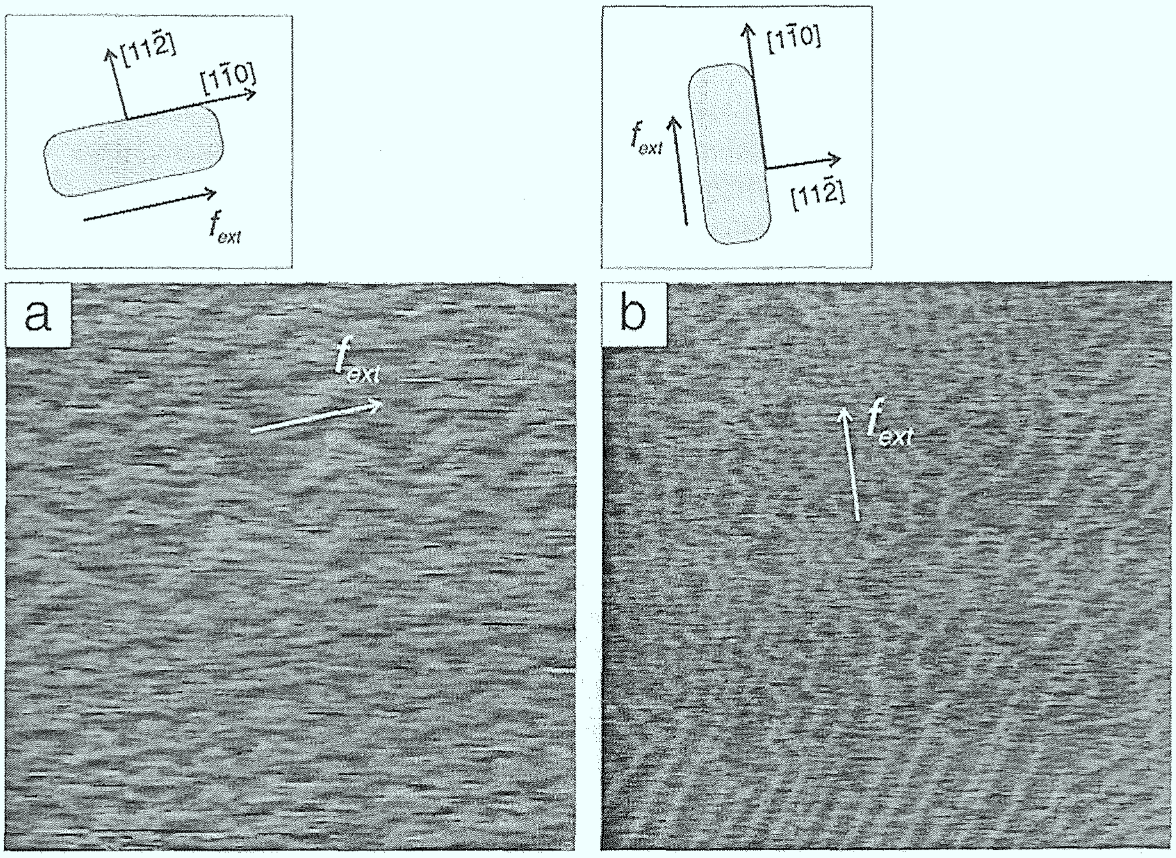

Figure 6.8: STM topographs taken from Au(111) thin crystal surface under strain. The longer axis of the crystal is aligned along the $[1\bar{1}0]$ direction. (a) A new type of reconstruction derived from the herringbone structure with a strongly reduced zigzag periodicity (1200 × 1200 Å, $\epsilon = 7.9 \cdot 10^{-6}$, V_t=31 mV, I_t=11 nA). (b) Two of the three domains are favored. (2600 × 2600 Å, $\epsilon = 4.7 \cdot 10^{-5}$, V_t=56 mV, I_t=10 nA).

can still observe B- and C-type domains (see Fig. 6.8b). Comparing with the schematic illustration in Fig. 6.2b, we infer that in the upper part of the image are BC-herringbone domains, and the straight double-lines in the lower part of the image are individual B-type domains. No large A-type domains or even AB-, AC-herringbone domains are observed in this image.

6.5 Conclusions

The possibility of using STM for the investigation of the surface restructuring under variable external strain has been demonstrated. The preliminary results on the reconstructed Au(111) surface show that external strain induces a change of the periodicity of the original $(22 \times \sqrt{3})$ reconstruction as well as a rearrangement of the three intrinsic orientation degenerate domains. When the strain exceeds a critical value, the reconstructed surface transforms into the (1×1) structure. After unloading of the crystal, a spontaneous back transformation into the reconstructed phase does not occur, even though the STM measurements demonstrate that the macroscopic bending is still within the elastic regime. The observed phase transition can be understood in terms of the Frenkel-Kontorova model. The rearrangement of the reconstructed domains is found to follow the predictions of the AVMJ theory.

Chapter 7

Zusammenfassung

Mittels Rastertunnelmikroskopie (RTM) wurde die reine und adsorbatbedeckte Au(111)-Oberfläche untersucht.

Zunächst wurden die Präparationsmethoden für die Verwendung von Au(111)/Quarz als Substrat für Adsorptionsexperimente weiter entwickelt und verbessert. Die "Fischgräten"-Rekonstruktion der Au(111)-Oberfläche wurde als Modellsystem zur Beurteilung der Funktionsfähigkeit des RTMs an Luft untersucht. Die Ergebnisse zeigen, daß in den meisten Fällen die "Fischgräten"-Rekonstruktion an Luft stabil ist und mit dem RTM abgebildet werden kann. Die Strukturen der Rekonstruktion an Luft sind ähnlich denen im Ultrahochvakuum (UHV). Wegen der Anwesenheit von Verunreinigungen nimmt die Mobilität der Rekonstruktion an Luft im Vergleich zum UHV stark zu. In einigen Fällen konnte auch die Auflösung der Rekonstruktion beobachtet werden.

Die Adsorption von Iod auf der Au(111)-Oberfläche wurde untersucht und die Entstehung verschiedener zweidimensionaler Strukturen und die entsprechenden Phasenübergänge in Abhängigkeit der Bedeckung verfolgt. Bei niedriger Iod-Bedeckung ($\theta \sim 0.33$) konnte eine $(\sqrt{3} \times \sqrt{3})$R30°-Struktur beobachtet werden. Mit zunehmender Iod-Bedeckung bildet sich eine uniaxial komprimierte Streifenphase mit $(p \times \sqrt{3})$-Struktur aus. Bei weiterer Zunahme der Bedeckung beobachtet man einen Phasenübergang erster Ordnung, bei dem die Streifenphase in eine hexagonal komprimierte, inkommensurable Phase übergeht. Diese Struktur weist im RTM ein hexagonales Moirémuster mit einer Periodizität von ~ 20 Å auf. Durch Änderung der Tunnelparameter (V_t bzw. I_t) können entweder die Iod- oder die Au-Atome abgebildet werden, wodurch sich die Iod-Struktur sehr genau bestimmen läßt.

Im Rahmen dieser Arbeit wurde eine neue, durch Sauerstoff verursachte langreichweitige hexagonale Rekonstruktion auf der Au(111)-Oberfläche entdeckt. Die Entstehung der neuen Rekonstruktion sowie die Struktur, Stabilität und Komposition wurden durch Experimente mit dem RTM, Photoelektronenspektroskopie (XPS), Augerspektroskopie sowie Röntgenbeugung (XRD) charakterisiert. Die Rekonstruktion wird durch langes Heizen bei hoher Temperatur (800°C) in einer Sauerstoff-Atmosphäre erzeugt. Auf atomarer Skala wird eine $(\sqrt{3} \times \sqrt{3})$R30°-Struktur beobachtet, die wahrscheinlich dem chemisorbierten Sauerstoff zuzuschreiben ist. Die hexagonale

Überstruktur besitzt eine Periodizität von 60-80 Å und eine Korrugation von ca. 0.5 Å. Diese Überstruktur läßt sich als Moirémuster aufgrund einer Gitterfehlanpassung zwischen den beiden obersten Atomlagen der Au(111)-Oberfläche interpretieren. Die Entstehung der sauerstoffinduzierten hexagonalen Rekonstruktion erfolgt über die präferentielle Keimung durch Oberflächendefekte und anschließendes laterales Wachstum der Rekonstruktion. Die Ergebnisse der XPS- und AES-Untersuchungen zeigen, daß die Anwesenheit von Verunreinigungen auf der Oberfläche außer Sauerstoff sehr gering ist: Somit ist die Rekonstruktion unmittelbar der Chemisorption von Sauerstoff an der Oberfläche zuzuschreiben. Die Ergebnisse der XRD-Experimente sind in Übereinstimmung mit den RTM-Beobachtungen.

Der letzte Teil der Arbeit befaßt sich mit dem Einfluß externer Spannungen auf die Rekonstruktion der Au(111)-Oberfläche. Zur Untersuchung des Zusammenhangs zwischen externer Kompressionsspannung und Rekonstruktion haben wir einen speziellen Versuchsaufbau entwickelt, der durch die Verbiegung eines 0.3 mm dicken Au(111)-Einkristalls eine variable externe Kompressionsspannung auf die Oberfläche ausübt. Mittels RTM kann dann die Änderung der Rekonstruktion in Abhängigkeit der Verbiegung untersucht werden. Die Ergebnisse zeigen, daß eine externe Kompressionsspannung eine Änderung der Periodizität und des Musters der Rekonstruktion induziert. Die Änderung der Rekonstruktion hängt ab von der Größe und Orientierung der externen Kompressionsspannung relativ zur lokalen Ausrichtung des Rekonstruktionsmusters. Theoretische Untersuchungen legen nahe, daß die Änderung der Periodizität durch die spannungsbedingte Änderung der natürlichen Fehlanpassung verursacht wird, während die Änderung des Rekonstruktionsmusters eine Folge der Änderung der Anisotropie der Oberflächenspannung ist. Beim Übergang der rekonstruierten Oberfläche in die unrekonstruierte (1x1)-Struktur entstehen viele kleine Au-Inseln auf der Oberfläche durch die freiwerdenden Goldatome. Obwohl die Biegeversuche makroskopisch elastisch und reversibel erfolgen, wurde auf atomarer Skala eine Umkehrung des Übergangs von der unrekonstruierten Oberfläche zurück in die rekonstruierte Au(111)-Oberfläche nach Aufhebung der Verbiegung nicht beobachtet.

Bibliography

[1] H.H. Rotermund, G. Haas, R.U. Franz, R.M. Tromp and G. Ertl, Science 270 (1995) 608.

[2] P. Stoltze and J.K. Nørskov, Phys. Rev. Lett. 55 (1985) 2502.

[3] G. Binnig and H. Rohrer, Helv. Phys. Acta 55 (1982) 726; G. Binnig, H. Rohrer, Ch. Gerber and E. Weibel, Appl. Phys. Lett. 40 (1982) 178; G. Binnig, H. Rohrer, Ch. Gerber and E. Weibel, Phys. Rev. Lett. 49 (1982) 57.

[4] R. Miranda, N. Garcia, A.M. Bar, R. Garca, J.L. Pea and H. Rohrer, Appl. Phys. Lett. 47 (1985) 367.

[5] Sang-II Park and C.F. Quate, Appl. Phys. Lett. 48 (1986) 112.

[6] V.M. Hallmark, S. Chiang, J.F. Rabolt, J.D. Swalen and R.J. Wilson, Phys. Rev. Lett. 59 (1987) 2879.

[7] K.H. Besocke, M. Teske and J. Frohn, J. Vac. Sci. Technol. A 6 (1988) 408.

[8] B. Drake, R. Sonnenfeld, J. Schneir, P.K. Hansma, G. Slough and R.V. Coleman, Rev. Sci. Instrum. 57 (1986) 411.

[9] B.J. Mclntyre, M. Salmeron and G.A. Somorjai, Rev. Sci. Instrum. 64 (1993) 687.

[10] J. Tersoff and D.R. Hamann, Phys. Rev. Lett. 50 (1983) 1998; J. Tersoff and D.R. Hamann, Phys. Rev. B 31 (1985) 805.

[11] K. Besocke, Surf. Sci. 181 (1987) 145.

[12] T. Michely, Ph.D. thesis, Bonn, 1991 (Jül-Bericht 2569).

[13] H. Röder, Diplom, thesis, Bonn, 1991.

[14] A.J. Melmed, J. Vac. Sci. Technol. B 9 (1991) 601.

[15] C.J. Chen, Phys. Rev. B 42 (1990) 8841.

[16] C.J. Chen, Phys. Rev. Lett. 65 (1990) 448.

[17] D.M. Kolb, Prog. in Surf. Sci. 51 (1996) 109.

[18] C.E.D. Chidsey, D.N. Loiacono, T. Sleator and S. Nakahara, Surf. Sci. 200 (1988) 45.

[19] A. Putnam, B.L. Blackford, M.H. Jericho and M.O. Watanabe, Surf. Sci. 217 (1989) 276.

[20] J.A. DeRose, T. Thundat, L.A. Nagahara and S.M. Lindsay, Surf. Sci. 256 (1991) 102.

[21] W. Haiss, D. Lacky, J.K. Sass and K.H. Besocke, J. Chem. Phys. 95 (1991) 2193.

[22] A. Hammiche, R.P. Webb and I.H. Wilson, Vacuum 45 (1994) 569.

[23] C.R. Clemmer and T.P. Beebe, Jr. Scanning Microscopy, 6 (1992) 319.

[24] M. Hegner, P. Wagner and G. Semenza, Surf. Sci. 291 (1993) 39.

[25] V. Heine and L.D. Marks, Surf. Sci. 165 (1986) 65.

[26] M.A. Van Hove, R.J. Koestner, P.C. Stair, J.P. Bibérian, L.L. Kesmodel, I. Bartos and G.A. Somorjai, Surf. Sci. 103 (1981) 189.

[27] Y. Tanishiro, H. Kanamori, K. Takayanagi, K. Yagi and G. Honjo, Surf. Sci. 111 (1983) 395.

[28] R.J. Needs, M.J. Godfrey and M. Mansfield, Surf. Sci. 242 (1991) 215.

[29] S. Narasimhan and D. Vanderbilt, Phys. Rev. Lett. 69 (1992) 1564.

[30] D.D. Chambliss, R.J. Wilson and S. Chiang, Phys. Rev. Lett. 13 (1991) 1721.

[31] B. Voigtländer, G. Meyer and N.M. Amer, Phys. Rev. B 44, (1991) 10354.

[32] J.A. Stroscio, D. T. Pierce, R.A. Dragoset and P.N. First, J. Vac. Sci. Technol. A 10 (1992) 1981.

[33] U. Harten, A.M. Lahee, J. Peter Toennies and Ch. Wöll, Phys. Rev. Lett. 54 (1985) 2619.

[34] Ch. Wöll, S. Chiang, R.J. Wilson and P.H. Lippel, Phys. Rev. B 39, (1989) 7988.

[35] J.V. Barth, H. Brune, G.Ertl and R.J. Behm, Phys. Rev. B 42 (1990) 9307.

[36] A.R. Sandy, S.G.J. Mochire, D.M. Zehner, K.G. Huang and D. Gibbs, Phys. Rev. B 43 (1991) 4667.

[37] N.J. Tao and S.M. Lindsay, J. Appl. Phys. 70 (1991) 5141.

[38] N. Takeuchi, C.T. Chan and K.M. Ho, Phys. Rev. B 43 (1991) 13899.

[39] J. Schneir, R. Sonnenfeld, O. Marti, P.K. Hansma, J.E. Demuth and R.J. Hamers, J. Appl. Phys. 63 (1988) 717.

[40] R. Emch, J. Nogami, M.M Dovek, C.A. Lang and C.F. Quate, J. Appl. Phys. 65 (1989) 79.

[41] Z. Wang and M. Moskovits, J. Appl. Phys. 71 (1992) 5401.

[42] D.G. Walmsley, P.A. Campbell, K.W. Smith and R.E. Somekh, Nanostructured Materials 3 (1993) 245.

[43] D. Porath, Y. Goldstein, A. Grayevsky and O. Millo, Surf. Sci. 321 (1994) 81.

[44] N. Eibel, H. Behner and H. von Seggern, J. Vac. Sci. Technol. B 13 (1995) 2119.

[45] D.D. Chambliss, R.J. Wilson and S. Chiang, J. Vac. Sci. Technol. B 9 (1991) 933.

[46] Y. Hasegawa and Ph. Avouris, Science 258 (1992) 1763.

[47] N.A. Surplice and W. Brearley, Surf. Sci. 52 (1975) 62.

[48] N.J. Tao and S.M. Lindsay, Surf. Sci. 274 (1992) L546.

[49] D.R. Peale and B.H. Cooper, J. Vac. Sci. Technol. A 10 (1992) 2210.

[50] M.A. Dubson, M. Kalke and J. Hwang, Phys. Rev. B 47 (1993) 10044.

[51] T. Michely, K.H. Besocke and G. Comsa, Surf. Sci. 230 (1990) L135.

[52] K. Morgenstern, G. Rosenfeld and G. Comsa, Phys. Rev. Lett. 76 (1996) 2113.

[53] S. Esch, M. Hohage, T. Michely and G. Comsa, Phys. Rev. Lett. 72 (1994) 518.

[54] M. Fournel, E. Lacaze and M. Schott, Europhys. Lett. 34 (1996) 489.

[55] S.A. Cochran and H.H. Farrell, Surf. Sci. 95 (1980) 359.

[56] B.G. Bravo, S.L. Michelhaugh, M.P. Soriaga, I. Villegas, D.W. Suggas and J.L. Stickney, J. Phys. Chem. 95 (1991) 5245.

[57] X. Gao and M.J. Weaver, J. Am. Chem. Soc. 114 (1992) 8544.

[58] N.J. Tao and S.M. Lindsay, J. Phys. Chem. 96 (1992) 5213.

[59] W. Haiss, J.K. Sass, X. Gao and M.J. Weaver, Surf. Sci. 274 (1992) L593.

[60] R.L. McCarley and A.J. Bard, J. Phys. Chem. 95 (1991) 9618.

[61] J. Wang, G.M. Watson and B.M. Ocko, Physica A 200 (1993) 679.

[62] B.M. Ocko, G.M. Watson and J. Wang, J. Phys. Chem. 98 (1994) 897.

[63] J.V. Barth, R.J. Behm and G. Ertl, Surf. Sci. 302 (1994) L319. J.V. Barth, R.J. Behm and G. Ertl, Surf. Sci. 341 (1995) 62.

[64] M.D. Chinn and S.C. Fain, Jr., Phys. Rev. Lett. 39 (1977) 146.

[65] K. Kern, R. David, P. Zeppenfeld, R.L. Palmer and G. Comsa, Solid State Commun. 62 (1987) 391.

[66] R. Vogel and H. Baltruschat, Ultramicroscopy, 42-44 (1992) 562.

[67] P. Bak, D. Mukamel, J. Villain and K. Wentowska, Phys. Rev. B 19 (1979) 1610.

[68] S.L. Yau, C.M. Vitus and B.C. Schardt, J. Am. Chem. Soc. 112 (1990) 3677.

[69] P. Bak, Rep. Prog. Phys. 45 (1982) 587.

[70] R. Dennert, M. Sokolowski and H. Pfnür, Surf. Sci. 271 (1992) 1.

[71] P. Zeppenfeld, K. Kern, R. David and G. Comsa, Phy. Rev. B 38 (1988) 3918.

[72] A.D. Novaco and J.P. McTague, Phys. Rev. Lett. 38 (1977) 1286.

[73] J. Chevrier, L. Huang, P. Zeppenfeld and G. Comsa, Surf. Sci. in press.

[74] F. Flores, P.M. Echenique and R.H. Ritchie, Phys. Rev. B 34 (1986) 2899.

[75] G.M. Shedd and P.E. Russell, Nanotechnology 1 (1990) 67.

[76] P. Zeppenfeld, C.P. Lutz and D.M. Eigler, Ultramicroscopy 42-44 (1992) 128.

[77] B. Hammer and J.K. Nørskov, Nature, 376 (1995) 238.

[78] M.A. Chesters and G.A. Somorjai, Surf. Sci. 52 (1975) 21.

[79] P. Légaré, L. Hilaire, M. Sotto and G. Maire, Surf. Sci. 91 (1980) 175.

[80] J. Cao, N. Wu, S. Qi, K. Feng and M.S. Zei, Chinese Phys. Lett. 6 (1989) 92.

[81] L. Huang, J. Chevrier, P. Zeppenfeld and G. Comsa, Appl. Phys. Lett. 66 (1995) 935.

[82] M.E. Schrader, Surf. Sci. 78 (1978) L227.

[83] N.D.S. Canning, D. Outka and R.J. Madix, Surf. Sci. 141 (1984) 240.

[84] J.J. Pireaux, M. Chtab, J.P. Delrue, P.A. Thiry, M. Liehr and R. Caudano, Surf. Sci. 141 (1984) 211.

[85] J. Oudar, Physics and Chemistry of surfaces, Blackie and Son Ltd. (1975) 48.

[86] Metal Surfaces, Ed. W.D. Roberts and N.A. Gjostein, American Society for Metals, Metals Park, OH, 1962.

[87] X. Bao, J.V. Barth, G. Lempfuhl, R. Schuster, Y. Uchida, R. Schlögl and G. Ertl, Surf. Sci. 284 (1993) 14; X. Bao, M. Muhler, B. Pettinger, R. Schlögl and G. Ertl, Catalysis Letters 22 (1993) 215.

[88] M.J. Wilkins, M.C. Davies, D.E. Jackson, C.J. Roberts, S.J.B. Tendler and P.M. Williams, Appl. Phys. Lett. 60 (1992) 1436.

[89] G.A. Somorjai and M.A. Van Hove, Prog. in Surf. Sci. 30 (1989) 201.

[90] K. Takayanagi, Ultramicroscopy 8 (1982) 145.

[91] T.A. Land, Th. Michely, R.J. Behm, J.C. Hemminger and G. Comsa, Surf. Sci. 264 (1992) 261.

[92] T. Wiederholt, H. Brune, J. Wintterlin, R.J. Behm and G. Ertl, Surf. Sci. 324 (1995) 91.

[93] F. Besenbacher and J.K. Nørskov, Prog. in Surf. Sci. 44 (1993) 5.

[94] H.P. Bonzel, A.M. Franken and G. Pirug, Surf. Sci. 104 (1981) 625.

[95] J.K. Gimzewski, S. Modesti, Ch. Gerber and R.R. Schlittler, Chem. Phys. Lett. 213 (1993) 401.

[96] J.V. Barth, R.J. Behm and G. Ertl, Surf. Sci. 302 (1994) L319.

[97] M. Peuckert, F.P. Coenen and H.P. Bonzel, Surf. Sci. 141 (1984) 515.

[98] C. R. Aita and N.C. Tran, J. Vac. Sci. Technol. A9 (1991) 1498.

[99] D.E. King, J. Vac. Sci. Technol. A13 (1995) 1247.

[100] H. Niehus and G. Comsa, Surf. Sci. 93 (1980) L147; H. Niehus and G. Comsa, Surf. Sci. 102 (1981) L14.

[101] This experiment was performed in collaboration with other scientists: J. Chevrier, L. Ortega, J.M. Gay, P. Zeppenfeld.

[102] R. Feidenhans'l, Surf. Sci. Rep. 10 (1989) 105.

[103] K. Kobayashi, Phys. Rev. B 50 (1994) 4749.

[104] J.W. Gibbs, The Scientific Papers of J.W. Gibbs, Vol. 1 (Longmans-Green, London) (1906).

[105] J.C. Phillips, Phys. Rev. Lett. 45 (1980) 905.

[106] R.J. Needs, Phys. Rev. Lett. 58 (1987) 53.

[107] D. Vanderbilt, Phys. Rev. Lett. 59 (1987) 1456.

[108] R. C. Cammarata, Surf. Sci. 279 (1992) 341.

[109] R.C. Cammarata, Prog. in Surf. Sci., 46 (1994) 1.

[110] M.C. Payne, N. Roberts, R.J. Needs, M. Needels and J.D. Joannopoulos, Surf. Sci. 211/212 (1989) 1.

[111] D. Sander and H. Ibach, Phys. Rev. B 43 (1991) 4263.

[112] R. Martinez, W.M. Augustyniak and J.A. Golovchenko, Phys. Rev. Lett. 64 (1990) 1035.

[113] A.J. Schell-Sorokin and R.M. Tromp, Phys. Rev. Lett. 64 (1990) 1039.

[114] H.J. Gossmann, J.C. Bean, L.C. Feldman, E.G. McRae and I.K. Robinson, Phys. Rev. Lett. 55 (1985) 1106.

[115] B.W. Dodson, Phys. Rev. Lett. 60 (1988) 2288.

[116] C. Günther, J. Vrijmoeth, R.Q. Hwang and R.J. Behm, Phys. Rev. Lett. 74 (1995) 754.

[117] F.K. Men, W.E. Packard and M.B. Webb, Phys. Rev. Lett. 61 (1988) 2469.

[118] O.L. Alerhand, D. Vanderbilt, R. D. Meade and J.D. Joannopoulos, Phys. Rev. Lett. 61 (1988) 1973.

[119] M.B. Webb, F.K. Men, B.S. Swartzentruber, R. Kariotis and M.G. Lagally, Surf. Sci. 242 (1991) 23.

[120] J. Frenkel and T. Kontorova, Phys. Z. Sowjetunion 13 (1938) 1.

[121] M. El-Batanouny, S. Burdick, K. M. Martini and P. Stancioff, Phys. Rev. Lett. 58 (1987) 2762.

[122] R. Ravelo and M. El-Batanouny, Phys. Rev. B 40 (1989) 9574.

[123] M. Mansfield and R.J. Needs, J. Phys. Condens. Matter 2 (1990) 2361.

[124] F.C. Frank and J.H. Van der Merwe, Proc. R. Soc. 198 (1949) 205, 216.

[125] P. Bak and V.J. Emery, Phys. Rev. Lett. 36 (1976) 978.

[126] V.L. Pokrovsky and A.L. Talapov, Zh. Eksp. Teor. Fiz. 75 (1978) 1151.

[127] Handbook of Physics, Ed. E.U. Condon and H. Odishaw (McGraw-Hill Book Company), (1950) P3-72.

[128] M. Hohage, T. Michely and G. Comsa, Surf. Sci. 337 (1995) 249.

Danksagung

Beim Deutscher Akademischer Austauschdienst (DAAD) danke ich für die finanzielle Unterstützung meiner Promotion in Deutschland.

Herrn Prof. Dr. George Comsa bedanke ich mich verbindlich für die Betreuung sowie für die Möglichkeit, die vorliegende Arbeit im Institut für Grenzflächenforschung und Vakuumphysik des Forschungszentrum Jülich durchführen zu können.

Mein besonderer Dank gilt Herrn Dr. Peter Zeppenfeld für die Betreuung und die Einführung in die faszinierende "Tunnel-Welt". Ohne seine stete Unterstützung, zahlreiche Anregungen und unermüdliche Hilfs- und Diskussionsbereitschaft wäre die Anfertigung dieser Arbeit nicht möglich.

Herrn Dr. Rudolf David bedanke ich mich für viele wichtigen Ratschläge bei der Durchführung der Arbeit.

Herrn Dr. Joël Chevrier und Herrn Dr. Sebastian Horch gilt mein Dank für die freundschaftliche Zusammenarbeit und viele nützliche Hinweise.

Herrn Josef Ziemons danke ich für seine ständige Hilfsbereitschaft bei der Lösung von technischen Problemen.

Herrn Martin Teske und Herrn Werner Hürttlen danke ich für die tatkräftige Hilfe im Elektronik- und Softwarebereich.

Herrn Udo Linke danke ich für seine hervorragend präparierten Kristalle und viele wichtige Ratschläge. Frau Birgit Schumacher danke ich für die Hilfe und ihre Geduld bei den zahlreichen Probenpräparationen.

Herrn F.P. Coenen danke ich für die Hilfe bei der XPS- und AES Untersuchung des O/Au(111)-System.

Herrn Strobl, Herrn Rausch und allen anderen Mitarbeitern der beiden Institutswerkstätten danke ich für die Anfertigung von Bauteilen und Geräten und ihre Hilfe bei Reparaturen.

Den Diplomanden und Doktoranden des IGV danke ich für die Hilfsbereitschaft und Diskussionen.

Schließlich danke ich meinen Eltern für ihre stete Unterstützung und Ermunterung. Meiner Frau Yufang und Tochter Bowen danke ich für ihre Unterstützung und Geduld sowie für die angenehme Familienatmosphäre während des Aufenthalts in Jülich.

FORSCHUNGSZENTRUM JÜLICH GmbH

Jül-3251
July 1996
ISSN 0944-2952